Exploration Into the Feasibility of Underwater Synthetic Jet Propulsion

Thesis by

AnnMarie Polsenberg Thomas

In Partial Fulfillment of the Requirements

for the Degree of

Doctor of Philosophy

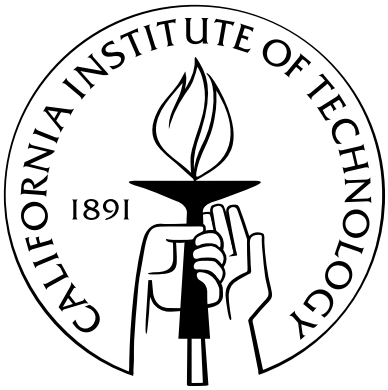

California Institute of Technology

Pasadena, California

2007

(Defended August 25, 2006)

Acknowledgements

I sometimes tell people that I was "raised by a village," which quite accurately describes my upbringing in Avalon, NJ. Over the last five years I have realized that this is truly a thesis "created by a village."

I am fortunate to have had an amazing advisor for my years at Caltech. Joel Burdick has been an incredible source of support and knowledge, as well as a wonderful mentor. There is no way I would have completed this thesis without his support and assistance. Often Joel had much more faith in me than I had in myself, and I am eternally grateful for that vote of confidence.

In my first few years at Caltech, John Dabiri was a wonderful classmate and friend. Thus, I am very lucky that Professor Dabiri agreed to become my co-advisor for this thesis. His deep knowledge of fluid mechanics has made this a much stronger work than it would have been without his guidance. In particular, he was integral to the development of the inflow model.

I am grateful to my committee members, Professors Chris Brennen and Erik Atonsson for their insightful comments during my candidacy exam and dissertation defense. They are responsible for making this a much stronger work. Dr. Michele Milano saw a talk on my work and approached me about a possible collaboration. I am

indebted to Michele for the countless hours he spent teaching me, assisting me with experiments, and helping me gain a greater perspective on science and life. Meetings with Professor Jerrold Marsden were helpful throughout this process. Professor Gharib kindly lent us his equipment, lab space, and wisdom. Professor Tim Colonius, Professor Niles Pierce, Jon Othmer, and Eric Johnsen were all kind enough to bring me up to speed on conformal mapping and potential flow.

I was fortunate to receive a lot of wonderful advice and help on the creation of the jet prototypes. John VanDeusen, of the Caltech ME Machine shop, spent countless hours assisting me on the design and construction of the synthetic jet prototypes. This work would not have been possible without the amazing undergrads who assisted me, particularly Vicente Fernandez, Maxwell Grazier G'Sell, Joanna Cohen, Kathleen Fischer, Jesse Escobedo, Zach Dydek, Amish Patel, Melissa Tanner and Aimee Eddins.

My friends kept me sane for the last five years, and I realize that that wasn't always an easy task. Kjerstin Williams and Maria Kriechbaum were always there for me when things were bleak. A panic stricken grad-student couldn't wish for a better pair of friends to keep her sane! The Burdick group was a wonderful "family" for five years, and I am particularly thankful for the friendship of Sam Pfister, Tim Chung, Patricio Vela, Kristo Kriechbaum, and Rachel Berquist. I have had the good fortune to have Mary Dunlop as an office-mate for the last two years. Maria Koeper is truly the "mother hen" of the Robotics group. Maria made Caltech a home away from home in a way that no one else possibly could. Thank you to Susan Buchman, Sarah Taylor-

Deak, and Emily Furia for being such an amazing long-disance support network. I'm so grateful for their friendship. The Caltech Robotics Outreach Group, particularly Angela, Dirk and Kerstin, provided a wonderful opportunity to procrastinate, yet still feel productive. Thank you to my students, teachers and colleagues at the Art Center College of Design for letting me indulge my artistic side and giving me a respite from Caltech.

I have had a large group of mentors during my 24 years of schooling. Thank you to Mrs DeSantis, Mr. Gil Godwin, Pam Nix, Mr Buckingham, and Mr Bradley for supporting me long before I thought I'd ever want to be an engineer. At MIT I was fortunate enough to learn from Professor Michael Triantafyllou, Professor Jake Kerwin, Professor John Leonard, Dr Tom Consi, Professor Woodie Flowers, Professor David Mindell, John Kumph, Dr Todd Taylor, Dr Rich Kimball. At MBARI, I am grateful to Drew Gashler, Paul McGill, Dr George Matsumoto and Bill Kirkwood.

My family has always supported me in my endeavors. I am so incredibly thankful to my mother and father for their unwavering support and near-daily phone calls. My sister, Joyce, definitely helped me keep things in perspective and reminded me to have fun once in a while! Aunt Lorraine and Luckey were always there to cheer me on.

Finally (and firstly, and always) I thank my husband, Chris. I can not imagine anyone more perfect for me. As I hand in this thesis I am looking forward to starting on the next chapter of my life with him, knowing full well that this chapter could never have been closed without his help. I truly am "the luckiest!"

Abstract

This thesis explores the feasibility of using synthetic jet actuators for the propulsion of small underwater vehicles. This work was inspired by the widespread use of pusatile jet propulsion by sea creatures such as squid, salp, and jellyfish. The jets created by these animals utilize vortex rings for thrust production. A method for creating similar vortex ring-based jets is the use of synthetic, or zero net mass flux, jets. These jets, which form a jet structure through the alternating sucking and blowing of fluid through a single orifice, have previously been investigated for the utility in air flow control.

This thesis presents the design, construction, and testing of aquatic synthetic jet prototypes. Force measurement and flow visualization experiments are performed on these jets to gain an understanding of the forces and flow structures produced. The flow visualizations confirm the outflow vortex ring observations reported previously in the literature and present the first images of vortex ring formation inside the synthetic jet chamber. A new phenomenon, that of self-induced coflow upstream of the jet orifice, is discussed. The force measurements present confirmation that a net thrust is produced by the jets and give insight to the relationship between jet forcing parameters (such as frequency) and the resulting thrust. An automated

genetic algorithmic approach to optimizing the thrust for a given jet geometry is also presented and tested.

Using the results of these experiments I propose a model for synthetic jet thrust. This model asserts that there are three force producing components to the flow: orifice inflow, orifice outflow, and a self-induced coflow. The contribution of each of these components is derived and compared with experimental results.

Included at the end of this thesis is a preliminary study into possible vehicle architecture for the utilization of synthetic jet thrusters.

Contents

List of Tables

List of Figures

List of Notation

A_o : Orifice area (m^2)

A_v : Characteristic area of vehicle (m^2)

C_D : Drag Coefficient (nondimensional)

δ : Membrane displacement (m)

d_c : Fluid chamber inner diameter (m)

d_d : Diameter of rigid disk attached to membrane (m)

d_o : Orifice diameter (m)

d_{oc} : Fluid chamber outer diameter (m)

f : Frequency of membrane actuation (Hz)

F : Complex velocity potential

$F_{cf}(t)$: Force generated due to coflow (N)

F_D : Drag force (N)

$F_{in}(t)$: Force generated due to inflow, neglecting coflow forces (N)

$F_{out}(t)$: Force generated due to outflow, neglecting coflow forces (N)

g : Gravitational constant ($\approx 9.8\ \frac{m}{s^2}$)

$G(\lambda)$: Genetic algorithm cost function

Γ : Circulation

Γ_{opc} : Circulation with over-pressure correction [1]

h_c : Chamber height (m)

h_o : Orifice thickness (m)

I : Hydrodynamic impulse (Ns)

I_{SM} : Hydrodynamic impulse using the slug model equations (Ns)

λ : Design parameter for genetic algorithmic optimization

m_a : Added mass (kg)

μ : Kinematic viscosity ($\frac{m^2}{s}$)

$\hat{n}$: Normal vector

ϕ : Velocity potential

ψ : Stream function

q : Source strength ($\frac{m^2}{s}$)

ρ : Fluid density ($\frac{kg}{m^3}$)

r_c : Fluid chamber inner radius (m)

r_d : Radius of rigid disk attached to membrane (m)

r_o : Orifice radius (m)

r_{oc} : Fluid chamber outer radius (m)

Re : Reynolds number (non-dimensional)

τ : Shear stress tensor ($\frac{N}{m^2}$)

t : time (s)

t_{in} : Duration of in-stroke (s)

t_{out} : Duration of out-stroke (s)

T : Period of oscillation (s)

u_m : Membrane velocity ($\frac{m}{s}$)

u_{or} : Spatially averaged velocity of fluid in orifice ($\frac{m}{s}$)

vp : Velocity profile ratio defined for sawtooth forcing signals (non-dimensional)

v_r : Radial velocity ($\frac{m}{s}$)

v_θ : Angular velocity ($\frac{m}{s}$)

v_v : Vehicle velocity ($\frac{m}{s}$)

W : Complex velocity

List of Abbreviations

AUV	:	Autonomous Underwater Vehicle
CCD	:	Charge Coupled Device
CFD	:	Computational Fluid Mechanics
CRS	:	Constant Random Search
CV	:	Control Volume
DPIV	:	Digital Particle Image Velocimetry
GA	:	Genetic Algorithm
MEMS	:	Micro-Electrical-Mechanical Systems
PWM	:	Pulse Width Modulation
ROV	:	Remotely Operated Vehicle

Chapter 1

Introduction

This thesis explores the potential use of synthetic, or zero net mass flux, jet propulsion for underwater robots. The design and construction of these jets is presented, along with force measurement and flow visualization experiments. A model for synthetic jet thrust is developed, and the feasibility of using synthetic jets as propulsors on underwater robots is discussed.

1.1 Motivation

There are two categories of underwater robots: Autonomous Underwater Vehicles (AUVs) and Remotely Operated Vehicles (ROVs). AUVs, as the name implies, operate autonomously. Mission plans and software are loaded into the vehicle, which is then launched. There is no real-time human control of the vehicle, and it operates freely, untethered to a surface ship. This lack of a tether allows AUVs to maneuver without fear of getting tangled or caught on something, but also means that all problem solving capabilities must be programmed in advance. Thus, AUVs at present are primarily used for large scale surveying.

ROVs are controlled in real-time by a human operator communicating with the vehicle through a tether. Real-time operator control gives the vehicle more capabilities than an AUV, as the pilot can make decisions when the robot faces difficulties, allowing ROVs to operate in more challenging situations than AUVs. ROVs are often outfitted with a wide assortment of cameras, grippers, and scientific equipment (e.g. coring drills, specimen containers, special sensors). Applications include ocean bottom coring, sample collection, underwater repairs, and photography. To date, essentially all ROVs and AUVs used in practice are propelled by groups of propellers. While ROVs are much more adept than AUVs at hovering in one place, precision maneuvers may result in less than optimal use of the propellers. Precise maneuvering may require a propeller to turn only a fraction of a revolution, as opposed to the continuous revolutions that propellers are designed for.

Despite the hydrodynamic advantages of propellers, there are a few downsides to their use in AUVs and ROVs. Two sub-sea robotic applications that have motivated this thesis are *exploration of dangerous, unpredictable environments such as shipwrecks or caves* and *tracking of slow-moving creatures such as larvaceans and jellyfish*. In the first scenario, given an unknown layout of an obstruction-filled area that is being explored, there is a high likelihood that the vehicle will bump into something risking damage to the robot. As such, it is not uncommon for propellers to be broken or damaged. In such a situation, any protruding component of the vehicle is a liability. One solution to these problems is using a ducted propeller. Examples of this can be seen on vehicles built by Bluefin Robotics, the Monterey Bay Aqurium

Research Institute, and others. It should be noted that the duct is primarily added for hydrodynamic reasons, yet the duct also provides a level of protection for the propeller. However, while more robust to breakage than an un-ducted propeller, the ducted propeller typically still protrudes from the vehicle's body and is thus still more susceptible to damage than a propulsor that is flush with the vehicle hull. Another alternative to exposed, unducted propellers is to embed the propellers in the hull such that water is pulled through a hole in the hull and the propeller does not protrude from the vehicle. From the standpoint of minimizing hull protuberances this is a great solution; however, this method involves piercing through the center of the hull, which complicates internal architecture. Additionally, when maneuvering in closed spaces, small changes in speed and maneuvering are crucial. Propellers are optimized for continuos revolution. Thus, small direction changes require the propellers to perform "twitchy" maneuvers.

The second motivational application, *tracking of slow-moving creatures such as larvaceans and jellyfish*, poses a different set of challenges. In discussions with biologists about this project, we were repeatedly told of their desire to have slow moving autonomous vehicles which could maintain a high degree of maneuverability. While the speed and maneuverability requirements are similar to those discussed above for navigating in tight spaces, there are other unique practical concerns. Propellers pose a threat to sea creatures, particularly fragile animals such as jellyfish. It is not uncommon for animals to be cut or killed by an ROV's propellers. More speculatively, it has also been suggested that given the lack of natural propellers, at least on a

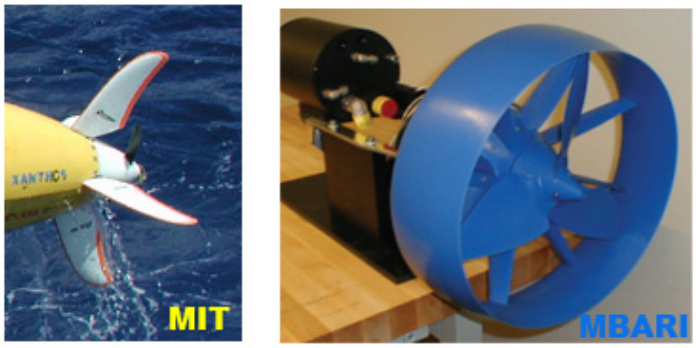

Figure 1.1: (A) shows a typical AUV tail configuration in which the small black propeller and white/orange maneuvering fins can be seen, and (B) shows a ducted AUV propeller. Figure (A) is courtesy of Brian Bingham, and Figure (B) is courtesy of Bill Kirkwood.

scale larger than the flagellum of micro-organisms, the wake structure produced by propellers may alert and scare off the very animals that the robots are trying to investigate.

After considering the thruster configurations of nearly forty commercial and experimental AUVs and ROVs, it becomes apparent that propellers are the only significant method used to propel underwater vehicles. One alternative that has been explored is flapping foils, an area in which a substantial amount of work has been done. However, flapping foil propulsion is still used primarily in laboratories and not in real-world applications [2, 3, 4, 5, 6, 7]. While flapping foils may potentially have an efficiency advantage over propellers, their mechanical design tends to be more complex and require a substantial amount of a vehicle's internal space to be dedicated to actuators and linkages.

As such, propellers and their role in propelling underwater vehicles have been intensely studied [8, 9, 10]. It is clear that in most regimes, propellers are the most efficient propulsion method, and much work has been done in the area of matching propulsion requirements to the optimal propeller [11]. However, as new regimes (such as low speed propulsion for small vehicles) are explored, the possibility arises that there may be more desirable propulsion methods for these applications.

1.2 Natural Inspiration

***"Ages before man discovered jet propulsion, cephalopods were jetting through primeval seas."*[12]**

Alternative methods of underwater propulsion can be found by looking at what occurs in the natural world. It should be noted that propellers do not exist in nature (with the arguable exception of the flagellum of bacteria), yet sea creatures have evolved numerous methods of propelling themselves through fluid [13, 14]. Our inspiration is the pulsed jet propulsion of many underwater sea creatures: squid, salp, and jellyfish are common examples [15, 16, 17, 18, 19, 20]. These creatures propel themselves by pulsing water out of a cavity in their body. The fluid rolls up into vortex rings as it exits the body. Weihs showed that this method of pulsed jets results in an increase in average thrust for a given mass flux relative to what can be accomplished with a steady jet [18]. It is, however, important to note that 70 of the roughly 176 known species of cephalopods have mantle lengths of less than 15 cm [21]. This seems to imply that there may be some limit to the size of the animal (or

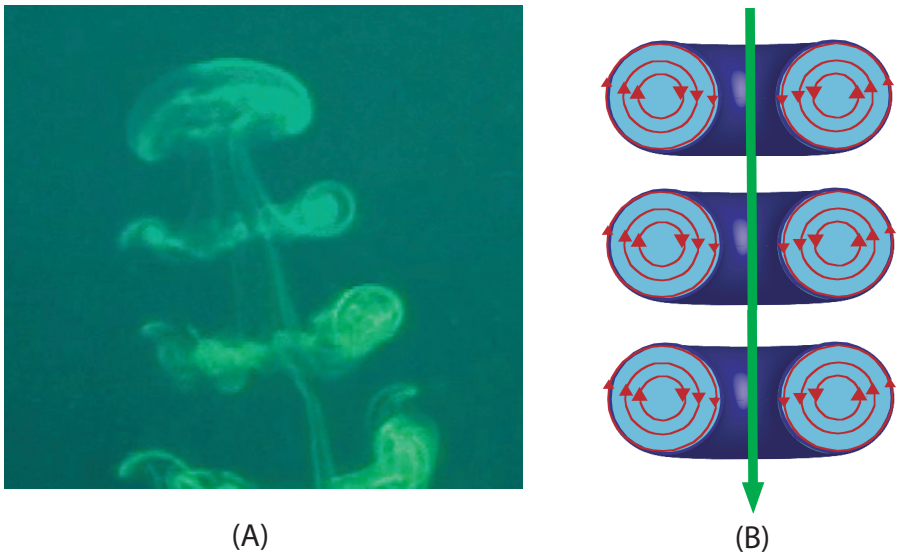

Figure 1.2: (A) Dye visualization of the wake of a swimming jellyfish (image courtesy of John Dabiri [23]); (B) Subsequent vortex rings pull fluid through their centers.

vehicle) for which this propulsion method is best suited. There are at least 22 species that have a mantle length of over 30 cm, with some reaching in excess of 100 cm [21]. O'Dor points out possible geometric and energetic constraints which may play a role in explaining the prevalence of smaller squid [22]. Whether or not these sizing constraints will apply to a synthetic jet propelled vehicle remains to be seen, but this size distribution shown in squids should not be ignored.

While the swimming of cephalopods and jellyfish inspire this thesis, it was decided early in the design process to develop a propulsor that does not exactly reflect what has evolved in Nature. Some creatures, such as jellyfish, suck water in and then expel it from the same orifice. Squid and salp, however, have separate orifices for these two functions. The choice of a synthetic jet as a candidate propulsor is motivated by that fact that it has only one orifice which can be implemented with mechanical

simplicity. Our reasons for this approach focus primarily on simplifying the design requirements for a vehicle using these thrusters. A more dramatic departure from Nature's design is the chamber section of our thruster, which has rigid walls. Most of Nature's jet propelled creatures have flexible chambers. For example, a jellyfish's bell expands as it fills with water and then contracts as it moves forward. It is likely that the flexible chamber is a desirable feature that aids in the efficiency of these creatures. Recent work by Dabiri [24] demonstrates that the ability to change the orifice diameter during the vortex ring ejection phase results in higher energy vortex ring structures. In the interest of mechanical simplicity, however, this thesis will look only at the case of a rigid chamber with a fixed orifice diameter.

1.3 Vortex Rings

It has been demonstrated experimentally (e.g. Smith and Glezer [25], Crook and Wood [26], and Krieg et al. [27, 28]) and numerically (e.g. Rizzetta et al. [29], Lee and Goldstein [30], and Mallinson et al. [31]) that synthetic jets produce a series of vortex pairs (or rings in the case of a circular orifice). Thus, a brief review of vortex rings is presented in this section. A thorough vortex ring review has been written by Shariff and Leonard [32].

Vortex ring formation is typically studied using a piston-cylinder apparatus consisting of a piston pushing outwards within a cylinder, as illustrated in Figure 1.3. The piston has a diameter of D and moves a distance of L. As fluid is pushed out of the orifice, a boundary layer forms on the inside surface of the cylinder. A vortex

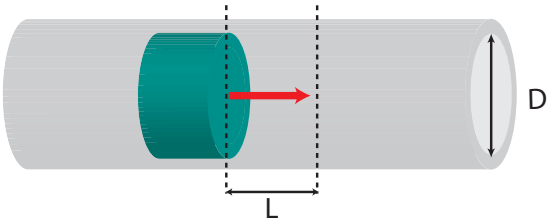

Figure 1.3: Schematic of a typical piston-cylinder vortex ring formation experiment. L is the distance travelled by the piston, and D is the piston's diameter.

ring is formed by the roll-up of this boundary layer. For more information on this process, the works of Maxworthy [33] and Didden [34] are excellent starting points.

The ratio between L/D, known as the characteristic stroke ratio, was investigated by Gharib, Rambod, and Shariff [35]. They discovered that the value of L/D had a strong correlation on the amount of circulation imparted into the ejected vortex ring. At a certain point, roughly L/D equal to 4, it was found that no more circulation could be added to the ring, and thus a trailing jet was formed behind the ring.

The primary method for modeling the circulation for a vortex ring is the slug model, in which the ejected fluid is treated as a cylindrical slug of fluid which has a uniform velocity [34, 32]. The slug model predicts circulation, Γ, as

$$\frac{d\Gamma}{dt} \approx \frac{1}{2} U_P^2(t), \tag{1.1}$$

where U_P is the velocity of the piston [32]. This approximation of Γ can then be used to approximate the impulse generated by the ring. More recently, Shusser et al. [36], Dabiri and Gharib [37], and Krueger [38] have all made modifications to the slug model in order to more accurately reflect experimental results on vortex formation.

1.4 Pulsatile Jets

Synthetic jets are a particular type of pulsatile jet. A pulsatile jet is, as the name implies, is one in which the jet is formed by bursts of fluid which are typically ejected from an orifice. The mean jet velocity can either return to zero between pulses (fully pulsed jet) or merely be reduced (forced jet).

As mentioned in the introduction to this thesis, the earliest pulsatile jets were those of aquatic creatures such as jellyfish and cephalopods [21]. Thus, there has been an effort to understand the thrust produced from such a jet in hopes of explaining Nature's use of them. Weihs [18] looked at periodic (pulsatile) jet propulsion in aquatic creatures. He found that for high pulse rates, pulsatile jets can produce more thrust than continuous jets of the same fluid mass. This analysis was based on the conjecture that the successive vortex rings are close enough to have an effect on each other, thus increasing the net thrust.

1.5 Synthetic Jets

A wonderful starting point for the investigation of synthetic jet flows is the summary written by Glezer and Amitay [39]. Synthetic jets are so-named because of their ability to create a momentum flux while maintaining no net mass flux. Rather than having separate inflow and outflow orifices, a synthetic jet typically has a single orifice which is used for both inflow and outflow. Every pulse of fluid ejection, during which a vortex ring leaves the orifice, is followed by a pulse of fluid inhalation. Thus, there

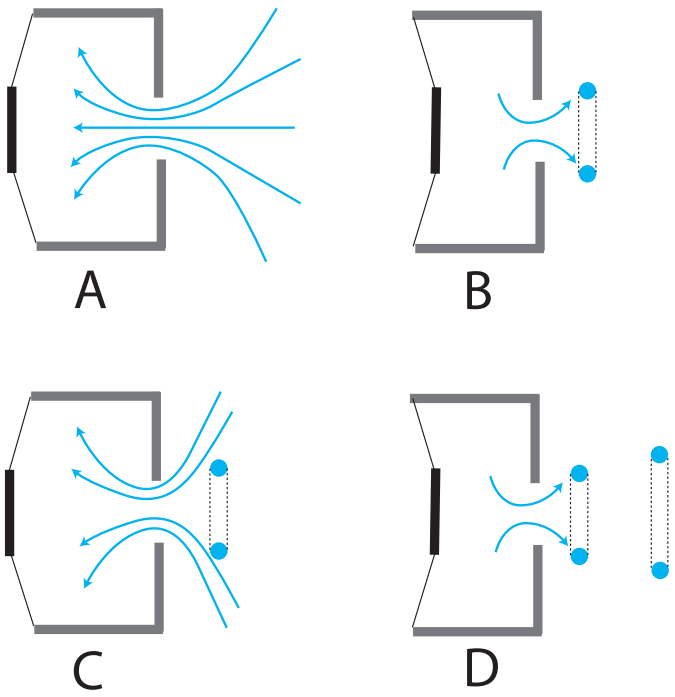

Figure 1.4: Stages of a synthetic jet: (A) The initial in-stroke sucks water into the chamber. (B) The out-stroke causes fluid to roll up into a ring. (C) The vortex ring pinches off. (D) During subsequent in-strokes, water is sucked in from around the departing vortex ring.

is an alternating pressure rise/drop across the orifice. In order for a jet to form, the impulse from a departing vortex ring must be sufficiently large as to overcome the forces that arise during the in-stroke phase. This process is illustrated in Figure 1.4.

Acoustic streaming [40], or streaming induced by acoustic waves, has been shown to create jet flow. However, as pointed out in Crook et al.[41], acoustic streaming requires the compression of the working fluid, yet synthetic jets occur in both compressible and incompressible fluids, and thus acoustic streaming can not offer a full explanation for the formation of synthetic jets in incompressible fluids. Therefore, while this may be relevant for air based synthetic jets, it is unlikely to be of relevance

to this aquatic synthetic jet study.

James and Jacobs [42] demonstrated the formation of a zero net mass flux jet in water that was formed entirely from the vibration of a circular diaphragm flush mounted on a plate. Their setup revealed that this chamberless configuration can produce a selfsimilar jet (where the jet radius and the inverse of the centerline velocity are both linearly dependent on the distance from the jet). They found this jet to be the result of the formation and collapse of cavitation bubbles on the membrane's surface.

Smith and Glezer characterized formation and evolution of synthetic jets [25] with a rectangular orifice geometry (using air as the working fluid). They determined the near field (close to the orifice) evolution of synthetic jet flow to be dominated by the formation, expulsion, and advection of discrete vortices. These vortex rings eventually transition to turbulence, slow down, and lose their coherence. During the outstroke of the membrane, fluid rolls up into a vortex pair (or ring in the case of a circular orifice) which travels away from the orifice at a self-induced velocity. They found that the in-stroke of the membrane seemed to trigger the transition of the vortex pairs to turbulence, possibly due to the core instabilities associated with the reversal of the streamline velocity near the orifice plane [25, 39]. They also noted the formation of secondary vortical structures wrapped around the cores of the primary vortices. They suggested that these lead to the breakdown of the primary vortices [25].

Additionally, Smith and Glezer concluded that the mean trajectories of the ejected vortex pairs consist of three domains characterized by the speed at which the vortex

pairs are travelling [25]. Initially, the vortex pairs travel at an approximately constant speed which scales with $I_0^{\frac{1}{3}}$, where $I_0 = \rho h \int_0^\tau u_0^2(t)\, dt$, τ is the outstroke time, and h is the width of the slit. The next domain is after the vortex pair has transitioned to turbulance. They found this to occur at approximately $0.5 < t/T < 0.8$; here T is the period of oscillation. In this domain the propogation velocity of the vortex pair decreases as $(t/T)^{-2}$. The vortex pair's velocity was found to be minimal at t/T=0.8. The final domain, beginning at about t/T=0.8, is characterized by the pair's velocity increasing like $(t/T)^2$ until the pair has become incorporated into the jet. They point out that the mean centerline velocity of the jet behaves slightly differently, increasing monotonically until the distance from the jet is about seven times the width of the orifice slit, and then monotonically decreasing.

One intriguing result found by Smith and Glezer [43] is that the reversal in flow direction along the jet centerline leads to the appearance of a stagnation point on the centerline. This point moves during the in-stroke. Additionally, they found that the stagnation streamlines divide the flow into two categories: flow that is driven by the in-stroke and flow that is driven by the out-stroke. It should be noted that these experiments were done for a synthetic jet with a non-axisymmetric geometry, designed for the purpose of vectoring an adjacent steady air jet. While their geometry is dramatically different than the one used for this thesis, this result will be referred to in Section 3.2 when discussing the forces produced during the jet's inflow phase.

1.5.1 Jet Design

Most prior work seems to be in agreement that the parameters of importance for a synthetic jet are its membrane deflection, cavity diameter, cavity height, orifice diameter (assuming a circular orifice), orifice thickness, and actuation frequency. Mallinson et al. [44, 45] present investigations into the effect of jet parameters (chamber depth, chamber diameter, orifice diameter, orifice depth, and orifice thickness) on the exit velocity of synthetic jets.

Crook and Wood [26] address the "lack of reliable information on the behaviour of synthetic jets operating at different conditions." With their goal being to obtain the maximum possible jet velocity, Crook et al.[41] investigated the effect of cavity height, orifice/slit depth, orifice/slit width/length, membrane thickness, and type of piezoceramic actuator, and compared the measured mean jet velocity. They utilized Rathnasingham's model of coupled fluid-structure interaction for a synthetic jet in a compressible medium [46]. The steady Poiseuille flow equation is used to model the flow inside the orifice. Their models were found to be more successful at predicting the maximum jet velocity measured an orifice diameter away from the jet than predicting the maximum velocity at the orifice. Additionally, they concluded that their model did not well predict the optimal orifice diameter or cavity height. In a later paper by Crook et al. [26], the effect of cavity height, orifice diameter, and orifice depth for a fixed actuation frequency is explored; however the work focused more on qualitative discussion of their results.

1.5.1.1 Orifice Geometry

This thesis is concerned solely with a synthetic jet having a circular orifice. This geometry is used by Crook et al.[41, 26], Rathnasingham and Breuer[46], and Mohseni et al. [47, 48, 27]. It should be noted that the synthetic jet used by Crook et al. has an orifice which is on the wall adjacent to the membrane, rather than opposite the membrane as is seen in most of the other jets. Alternatively, Smith and Glezer [25] , performed their experiments on jets with a rectangular orifice slit. Both geometries have proven effective at producing synthetic jet flow. (A third synthetic geometry, the so-called "springboard actuator." is used by Rathnasingham and Breuer [46], but will not be dealt with in this thesis.)

The advantage of the high aspect rectangular orifice is that it lends itself to $2-D$ modelling (away from the ends of the rectangle). As pointed out by Lee and Goldstein [30], three dimensional simulations were prone to external flow breakdown due to three-dimensional instabilities. Circular orifice geometries, on the other hand, necessitate three dimensional modelling to adequately predict jet velocities and properties.

1.5.1.2 Scale

Glezer and Amitay [39] point out that it should be possible to create synthetic jets over a wide range of scales given the characteristic dimensions of the jet scale with the orifice diameter. However, synthetic jet investigations have primarily focused on jets smaller than the ones presented in this thesis.

Micro-synthetic jets have been constructed and tested by Coe et al. [49], Müller et

al. [50, 51], Mallinson et al. [31]. Amitay et al. [52] used a synthetic jet rectangular orifice width of 0.5 mm. Crook et al. [41] experimented on jets with a circular orifice diameter of 0.5 mm, while that used by Holman et al. [53] had a diameter of 2 mm.

In water, Crook and Wood [26] used synthetic jets with orifices of 5 and 7 diameters. More extensive testing of synthetic jets was done by Mohseni and colleagues [48, 27, 28]. They used an array of orifice diameters ranging from approximately 0.3 to 1.0 mm.

1.5.1.3 Jet Actuation Techniques

A variety of actuation techniques have been used to drive the membrane of a synthetic jet. Piezoelectric actuation of a membrane seems to be the most common method and is used in Crook et al. [41], Mallinson et al.[44], Chen et al. [54], Lee et al. [30], and Smith and Glezer [55, 25]. Alternatively, pistons were used in theoretical models by Rathnasingham and Breuer [46]. Mohseni et. al [47, 48, 56, 27] have successfully generated thrust using solenoid-driven aquatic synthetic jets. Finally, acoustically driven cavities were used by Müller et al. [50, 51].

1.5.2 Induced Velocity Field

Experimentally, the focus of synthetic jet research has primarily been to achieve an understanding of the velocity field. To achieve this, a variety of flow visualization techniques have been used. Hot wire anemometry readings were used by Mallinson et al., Rathnasingham et al., and Smith and Glezer [44, 46, 25]; laser doppler velocimetry was used by Gallas et al. [57]; Schlieren visualization techniques were used by Smith

and Glezer [25].

Smith and Glezer [55, 25] showed the evolution of a synthetic jet near the orifice to be dominated by the time-periodic formation and advection of vortex pairs. These pairs transition to turbulence and then lose their coherence as they move away from the orifice.

1.5.3 Modelling Synthetic Jet Flow

One goal of this thesis is to develop a simple model relating the geometry of a synthetic jet to its average thrust. While the modelling of synthetic jet flow is an active field, the dominant vein of this research is on computational fluid dynamic methods of modelling the flow. Rumsey et al.[58] wrote in their summary of the findings of the 2004 Computational Fluid Dynamics (CFD) Validation Workshop on Synthetic Jets that CFD can only qualitatively predict the flow physics. This is due in part to the wide variation in results among different CFD techniques.

Rizetta et al. [29] numerically solved the flow field inside and outside of the fluid chamber using the *compressible* unsteady Navier-Stokes equations. They used a rectangular orifice geometry with a large aspect ratio. Their work found the height of the fluid chamber to have a strong effect on the jet exit outflow profile. Lee and Goldstein [30] present a two-dimensional direct numerical simulation of synthetic jet flow. An intriguing aspect of their work is the investigation of the effect of orifice geometry on jet velocity. They evaluated flow properties for three different orifice (or "lip") geometries: a cylindrical orifice hole, an orifice with rounded edges, and an

orifice with a cusp-shaped lip. The rounded lip was found to allow more fluid to be entrained from the sides during the inflow, which increased the spanwise velocity.

Mallinson et al. [45] present a numerical simulation using the commercial Navier Stokes solver CFX4.3. They model a jet with air (temperature 300K) as the working fluid and a sinusoidally vibrating membrane. They ran their numerical simulation for frequencies of 0.725 kHz and 1.45 kHz and for membrane deflections of 0.2-1 μm. Interestingly, they find, for all combinations of frequency and deflection, that the average velocity along the orifice centerline was greater than zero. In other words, the actuator spends more time ejecting fluid at the center of the orifice than it does ingesting fluid. Given that their model's membrane spends equal time pushing out and pulling in, this is an intriguing result. They also add that there is evidence that most of the ingestion of fluid occurs along the edge of the orifice. However, this positive velocity offset result is not in agreement with the experimental results of Smith and Glezer [25]. Smith and Glezer's experiment, performed in air for a frequency of 1.140 kH, found that at the center of the orifice the time averaged velocity is zero. Mallinson concludes that "no simple complete functional relationship is apparent" between jet velocity and membrane-velocity/forcing-frequency, despite the presence of a nearly linear relationship.

Tang and Zhong [59] present an incompressible flow model, pointing out that prior to this there was no analytical model to quantitatively predict the performance of synthetic jets. Their model assumes a circular orifice and uses the Buckingham-Pi theorem to nondimensionalize the performance parameters of the jet. Their model

found good correlation for circulation and mass/moment flux particularly for L/D < 3.5. For stroke ratios greater than 3.5, they found it necessary to add an empirical correction factor.

1.5.4 Applications of Synthetic Jets

1.5.4.1 Flow Control

The primary application of synthetic jets, as discussed in the literature, is active flow control. Smith and Glezer demonstrated the effectiveness of using synthetic jets to vector the flow of adjacent jets. Crook et al. [41] and Amitay et al. [52] used synthetic jets to affect flow separation on an airfoil. Mallinson et al. [45] show synthetic jets to be effective at mixing in both flames and hypersonic cross-flow.

1.5.4.2 Thrust Production

The idea of using synthetic jets as propulsors is a relatively new concept. Müller et al. [50, 51] propose synthetic jets as a method of propulsion for micro-airborne platforms. Their design utilizes MEMS technology to embed electrostatic actuators into a wafer. They present a proposed model for thrust as well as experimental results. Their experimental results for thrust, however, are not the result of force measurements, but rather predictions based on fluid velocity measurements. It should be noted that the geometry of their synthetic jet actuator, as shown in Figure 1.5, is quite different than the other geometries discussed in this section. Their model for thrust was constructed using conservation of momentum. For the outflow, the thrust contribution was found

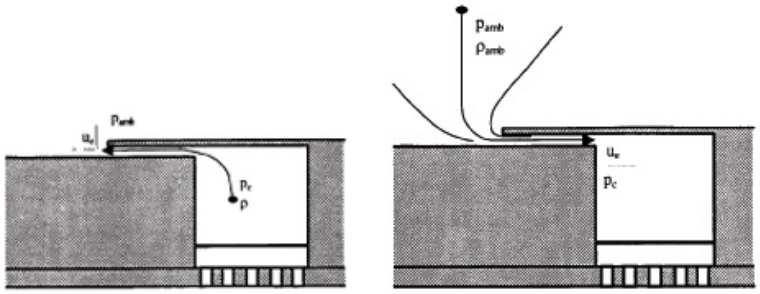

Figure 3. Streamline during outflow part of cycle.

Figure 4. Flow streamlines during inflow to the cavity.

Figure 1.5: Schematic of the resonator used by Müller et al.[50, 51]. Image used with permission of Professor Luis Bernal.

to be

$$J = \frac{1}{T}\int_{u_e>0} \rho u_e^2 A_{JE} dt, \tag{1.2}$$

where T is the period of membrane oscillation, $u_e(t)$ is the maximum velocity at the orifice plane, and A_{JE} is the effective area of the throat (orifice). During the inflow, drag must be taken into account, and thus

$$D = -\frac{\rho_{amb} U}{T}\int_{u_e<0} u_e A_E dt, \tag{1.3}$$

with ρ_{amb} representing the ambient fluid's density, A_E the effective area of the throat, and U the flow speed of the fluid outside of the jet chamber. This model will be referred to in Chapter 4, when a model for thrust from circular orifice aquatic synthetic jets is presented.

Mohseni, Krieg, and collaborators [48, 56, 27, 28] have shown the potential for synthetic jets to create a net thrust underwater. Their work included using solenoid-

driven synthetic jets to turn a submerged cylinder. They found that thrust produced by their aquatic synthetic jets is dependent on the square of the actuation frequency. They also found that an L/D formation ratio of between 4 and 5.5 produced the most thrust when all other parameters were kept the same. This is in agreement with the findings of Gharib et al. [35] in their work concerning the optimal L/D for imparting the maximum circulation into a vortex ring. To the best of our knowledge, Mohseni's work and our work is the first to directly experimentally measure the thrust produced by a synthetic jet (in any fluid). One particularly intriguing result found by Krieg, Mohseni et al. [28] was that for certain forcing conditions ,the thrust measured was *always* positive; thus the in-stroke and out-stroke stages produced thrust in the same direction. This brings to mind Mallinson et al.'s [31] observation that their numerical simulation showed that the centerline average velocity was nonzero, despite a symmetric membrane forcing profile. Krieg and Mohseni propose using the slug model to calculate the impulse generated by the jet. Chapters 5 and 4 will show that the slug model, while providing a qualitative prediction of thrust, does not completely describe the thrust producing phenomena of synthetic jets, and thus must be amended.

1.6 Advantages of Using Synthetic Jets for AUV and ROV Propulsion

For the applications proposed above, synthetic jets have many potential advantages. First, these jets are compact mechanical structures, requiring only a small volume of space. When used in small AUVs, they could potentially provide a propulsion scheme which consumes very little of the vehicle's precious internal volume, thereby leaving more room for vehicle payloads. Second, the synthetic jet has only one moving part, which lowers the probability of mechanical failure. As an additional benefit of having only a single moving part, only one simple seal is necessary to protect the actuator from the surrounding fluid. From a vehicle hydrodynamics perspective, synthetic jets can be mounted in such a way that they do not protrude from a vehicle's hull. This can allow for a reduction in vehicle drag and a possible increase in vehicle efficiency. Finally, the wake structure and noise generated by synthetic jets are likely to be less obtrusive for underwater surveillance of biological organisms. Discussions with biologists have revealed that animals are often scared away by propellers. While this is undoubtedly due in part to the sound produced by propellers, it is also possible that the unnatural wake they produce also causes animals to depart. We hypothesize that the more natural wake structure of synthetic jets may be less intrusive to animals. On a related note, propellers are often responsible for injuring or killing marine creatures. Lacking a propeller's sharp blade, synthetic jets are less likely to injure animals and objects.

1.7 Thesis Outline and Contributions

This chapter presented the background and motivation for this thesis. The following chapters will present the investigations we have performed to characterize the thrust produced by a synthetic jet, as well as the viability of using these jets for vehicle applications.

Chapter 2 presents the variety of physical synthetic jet prototypes constructed to perform the experiments presented in this thesis. While there is a wide array of designs for synthetic jets in air, the incompressibility and density of water poses a different design consideration. Three different membrane actuation methods (solenoid, speaker coil, and motor) are presented and analyzed. While solenoid and motor driven aquatic synthetic jet work has been presented by Mohseni and colleagues, [27, 28], this thesis (and related conference articles [60, 61, 62]) is the first to explore the use of voice coil actuation for underwater synthetic jets. This chapter will also discuss potential improvements for the design of the next generation of synthetic jet actuators.

In Chapter 3, flow visualization experiments, both qualitative and quantitative of the jet prototypes are presented. Dye flow visualization and DPIV (digital particle image velocimetry) experimental results are shown and discussed. One particularly intriguing result is the observation of an upstream coflow induced by the synthetic jet. To the best of our knowledge, this phenomenon has not previously been investigated. Additionally, this chapter will present visualizations of the vortex rings formed during the instroke (inside the fluid chamber) and outstroke (in the ambient fluid outside of the jet chamber).

Chapter 4 presents a model for thrust produced by a cylindrical synthetic jet. The model reflects geometry and membrane forcing profile. An analysis of the inflow is presented which explains why a net thrust is produced even in the presence of a symmetric forcing profile. The coflow phenomenon discussed in Chapter 3 is analyzed, and its potential to augment the jet's net thrust is shown. Finally, charts showing the impact of various jet parameters on the produced force are included. These charts are useful for the design of synthetic jets.

Chapter 5 will present the setup and results of the experiments run to measure the amount of force produced by the jets. Despite the presence in the literature of synthetic jet velocity measurements, there is not a similar body of experimental measurement of force. Force measurement of synthetic jet thrust is a fairly new result, as force measurements have only been presented by Mohseni and colleagues [27, 28] (in water) and Kim et al. [63] (in air). Our studies look at the effect of both frequency and forcing profile on thrust generation. Additionally, this chapter presents the method and results of an automated thrust optimization technique designed to use a genetic algorithm to find the jet forcing parameters resulting in the greatest produced thrust.

As the intent of this project is to assess the feasibility of using synthetic jets as propulsors on underwater vehicles, Chapter 6 analyzes the feasibility and practicality of this application. The final chapter presents other possible applications of aquatic synthetic jets and suggestions for future work.

Chapter 2

Synthetic Jet Construction

While synthetic jets in air have been widely studied [54, 41, 57, 39, 42, 44, 55], the literature on aquatic synthetic jets is sparse. For this reason, we chose to start this project by designing and constructing a wide number of working prototypes.

The essential elements of a synthetic jet, regardless of the working fluid, are the same. Only four elements are needed (as shown in Figure 2.1.) They are:

- **Fluid Chamber**: This is the body of the jet, into which fluid is pulled in and expelled.
- **Flexible Membrane**: The bottom of the *fluid chamber* consists of a flexible material which can be moved up and down.
- **Membrane Actuation Mechanism**: The jet requires some method for moving the *flexible membrane*. This thesis will discuss solenoid, speaker coil, and motor-driven methods.
- **Orifice Plate**: By using an orifice plate to cover the end of the *fluid chamber* opposite the moving membrane, the L/D ratio for the synthetic jet can be changed without modifying the *membrane actuation mechanism*.

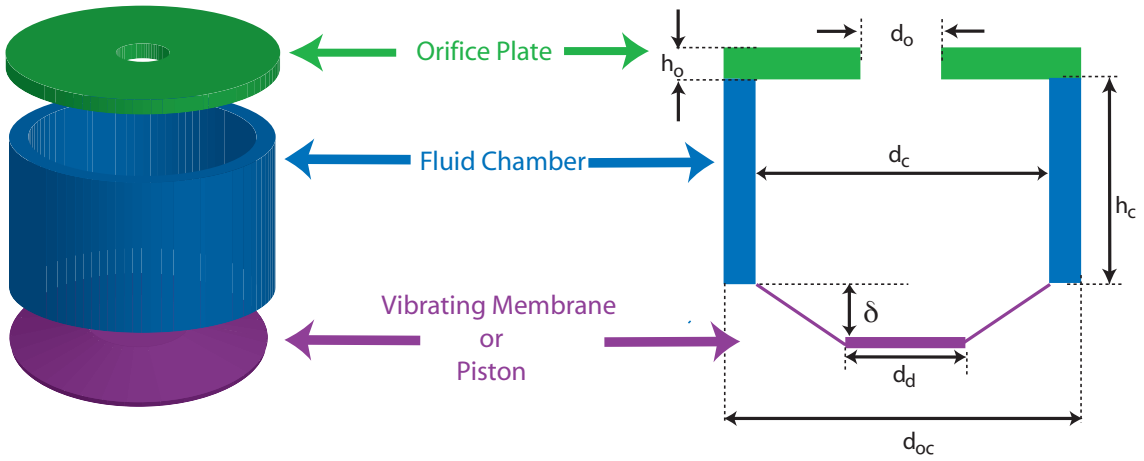

Figure 2.1: Schematic of a synthetic jet actuator: exploded and cross-sectional views.

These four components describe the simplest synthetic jet. As will be discussed later, the design of these components can have a substantial effect on the force produced by the jet.

As mentioned in Chapter 1, most synthetic jets in the literature use piezo-electric (or piezo-ceramic) actuation to vibrate the membrane [49, 55, 46, 41]. While piezo-electric systems have shown to be well-suited for the construction of synthetic jets with a compressible working fluid, the incompressibility and higher density of water imposes different conditions on the jet. Therefore, alternative membrane actuation methods were explored.

2.1 Speaker-Driven Jet Prototypes

Given that one of our secondary goals was to develop a low-cost thruster, we were particularly interested in "off the shelf" methods of vibrating the membrane. A

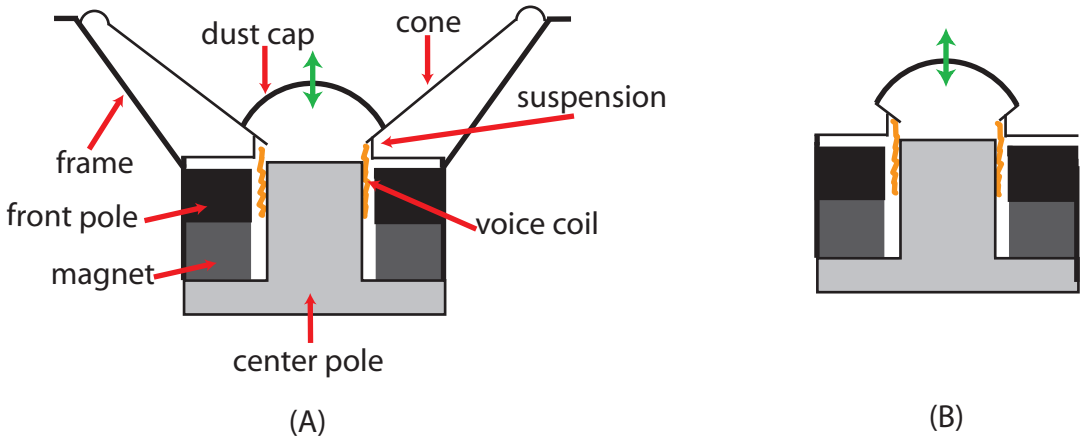

Figure 2.2: (A) Typical speaker configuration; (B) Speaker with cone and frame detached.

starting point was an exploration of voice coils (speakers).

Speakers consist of three main components: a magnet, a voice coil, and a suspension. The voice coil consists of wire coiled into a cylinder and placed over the center pole of the speaker. The voice coil is surrounded on the outside by a cylindrical magnet. Current passing through the voice coil induces a magnetic field which interacts with the field of the outer magnet. This interaction causes the wire coil to move. As the wire coil is attached to the speaker's cone, the cone moves as well. By alternating the current in the coil, the speaker cone can be made to travel up and down. The pressure waves created by the speaker cone moving through the air is what we hear as sound [64]. Figure 2.2 shows schematics of an unmodified speaker as well as a speaker that has been modified for use in our synthetic jet design. Various methods for waterproofing speaker cones were explored before deciding to build a water tight housing to enclose the speaker, as shown in Figure 2.3. It became clear that attempts to use the speaker's cone as the oscillating membrane would be too

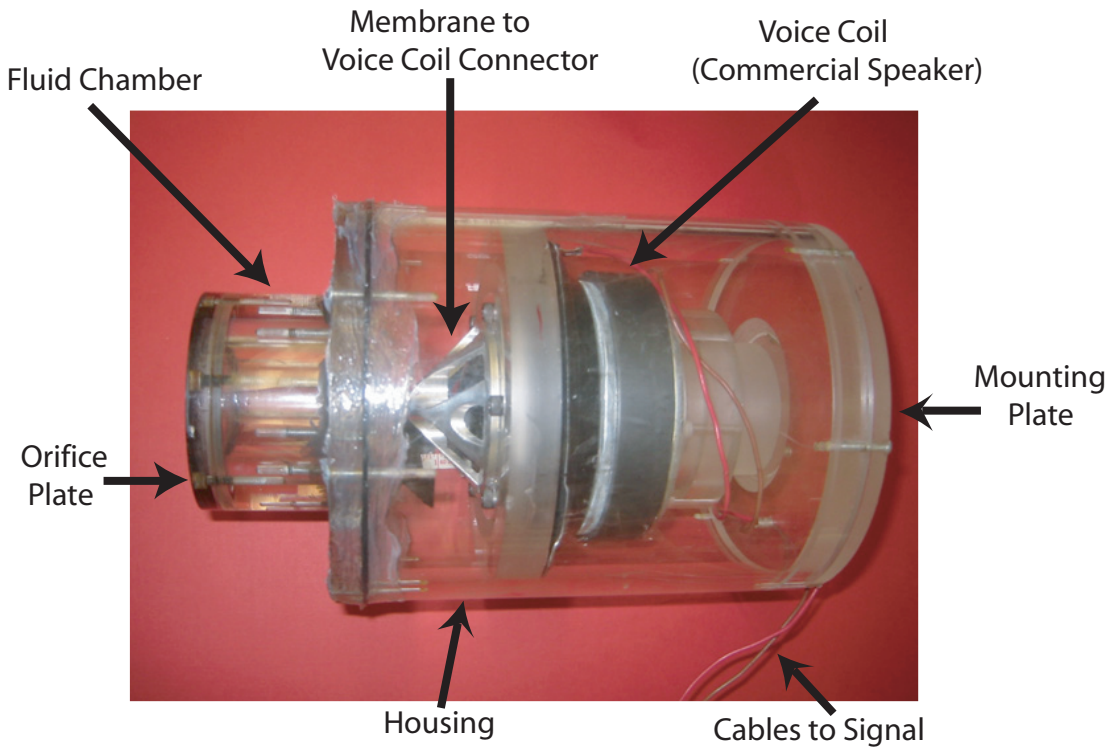

Figure 2.3: Speaker-driven synthetic jet prototype.

challenging. Thus, a metal attachment was designed and constructed which could clamp onto the speaker's dustcap, as shown in Figure 2.4. A threaded hole at the top of this piece allows for attachment to the metal disk, which is affixed to the back of the flexible membrame, which in this case is made out of 0.45 mm thick rubber. The membrane is mounted between the fluid chamber and the cap of the jet housing. The use of o-rings and gaskets between all connections prevented leakage. The orifice plate is a two-part design, as shown in Figure 2.5, which allows the orifice diameter to be changed easily. Dimensions for this jet are given in Table 2.1. The speaker coil rests in a cylindrical housing. The housing, as shown in Figure 2.3, is substantially longer than the size of the speaker would necessitate. This allows for greater stability

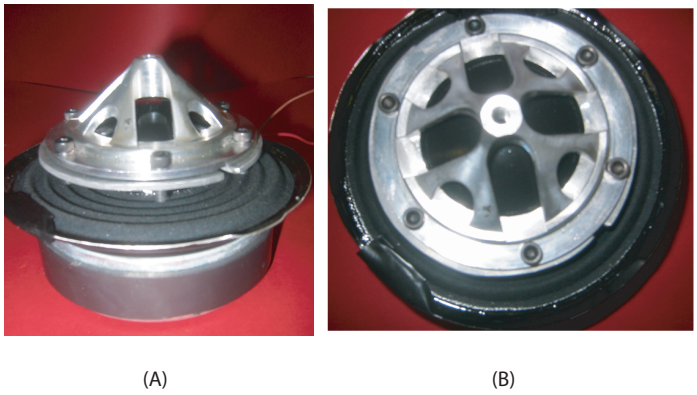

Figure 2.4: Speaker with mechanical adapter that allows a membrane to be attached. (A) side view; (B) top view.

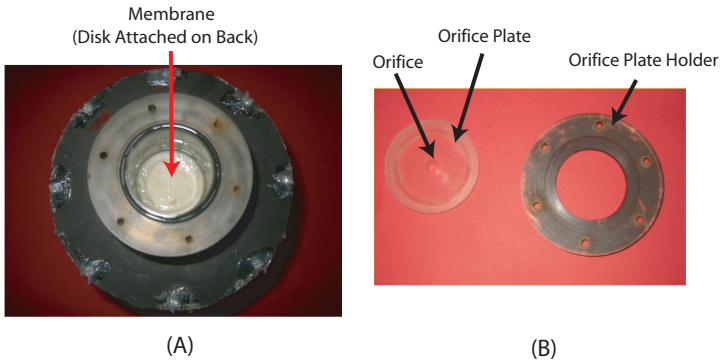

Figure 2.5: (A) Top view of fluid chamber with orifice plate removed. (B) Orifice plate and holder.

in the force measurement experiments presented in Chapter 5.

The speaker used for these experiments was a Goldwood GW-8024 190 Watt 8" woofer, and was chosen because of its low cost (< $20 per voice coil). Additionally, its plastic cone makes it less susceptible to damage should water leak into the housing. Signals were sent to the speaker using a Measurement Computing PCMCIA digital-analog card (Model DAS16/12-AO) and a car stereo amplifier (Alpine brand, MRP-T220) as illustrated in Figure 2.6. The use of an audio grade amplifier allows for both a

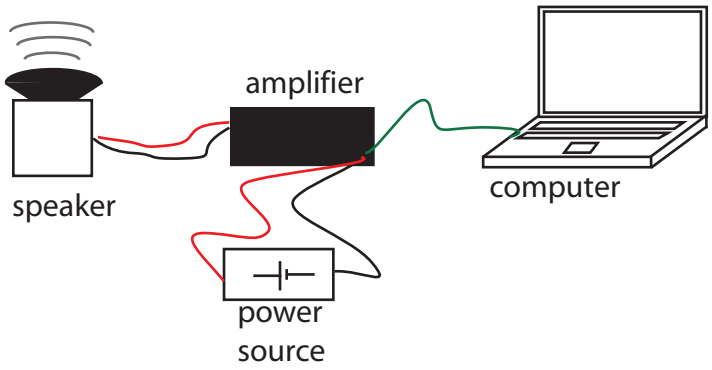

Figure 2.6: Schematic of speaker-driven prototype configuration.

d_c	3.81 cm
d_{oc}	7.62 cm
d_o	variable (up to d_c)
d_d	2.85 cm
δ	$\approx$ 3 mm

Table 2.1: Dimensions for speaker-driven prototype.

proper impedence match between speaker and amplifier and a necessary amplification of the signal sent from the computer.

An additional voice coil prototype thruster was built using a Bruel and Kjael 4810 minishaker, a device designed to vibrate small objects. This voice coil provides more force and thus could allows for greater membrane throws. The minishaker's cost, however, was $\approx$ 100 times greater than that of the commercial audio-grade voice coil and not easily configurable for possible future jet designs. Thus, this prototype was used only for the automated thrust optimization experiment presented in Section 5.5.

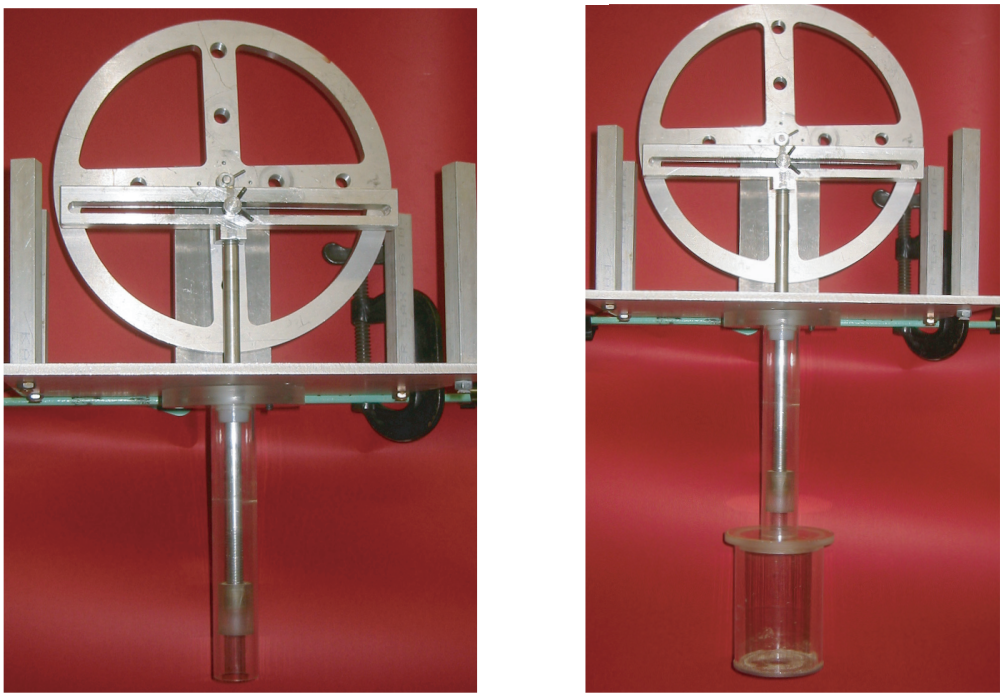

(A) (B)

Figure 2.7: Scotch yoke prototype in (A) piston cylinder configuration and (B) with larger fluid chamber attached.

2.2 Motor-Driven Prototype

While there are many benefits to using the voice coil prototypes, the exact throw of the membrane can vary from trial to trial. Additionally, the relatively small throw of the voice coils makes it harder to be sure of the membrane's velocity at any given time. Finally, the throw of the membrane constrains the scale of the rest of the jet design. This makes flow visualization difficult, as the scale of the fluid structures are smaller than can be reliably visualized. Thus, for more precise studies, particularly those involving flow visualization, it is important to have a prototype with a repeatable, and larger, throw distance. This was accomplished using a "Scotch Yoke" design, as

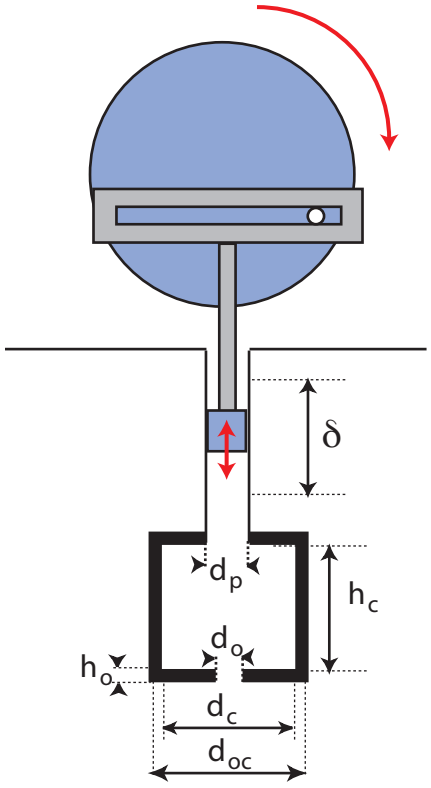

Figure 2.8: Scotch Yoke prototype parameters.

illustrated in Figures 2.7 and 2.9. Tapped holes at various distances from the wheel's axis allow for easy adjustment of the L/D ratio for the jet. The dimension values for this prototype are listed in Table 2.2. As shown in Figure 2.7, the larger fluid chamber can be removed, allowing for a "piston-cylinder" setup. This configuration, which sets $d_o = d_c$, allows the demonstration (as shown in Chapter 3) that a synthetic jet can be formed without an orifice plate.[1] Signals are sent to the Pittman GM8724

[1]This is an unsurprising result, as James and Jacobs [42] demonstrated the formation of a zero net mass flux jet in water that was formed entirely from the vibration of a circular diaphragm flush mounted on a plate. Their experiment is discussed further in Chapter 1. It should be noted that they did not detect the presence of distinct vortex rings.

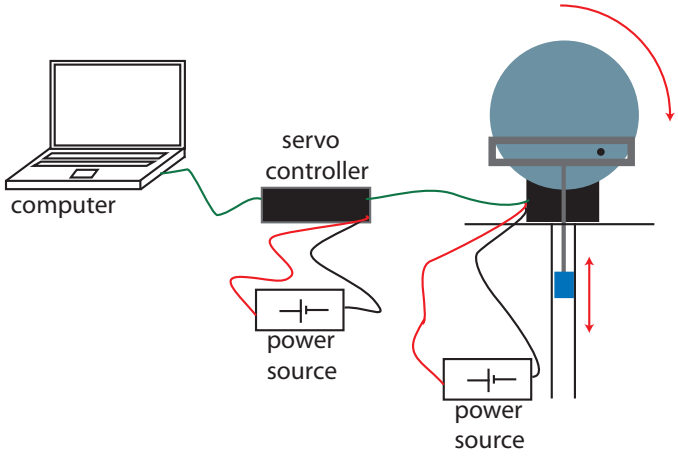

Figure 2.9: Schematic of Scotch Yoke prototype configuration.

d_c	2.75 in
d_{oc}	3.0 in
d_o	0.75 in
d_p	1.0 in
h_o	0.125 in
h_c	3.9 in
δ	variable (from 2-8 inches)

Table 2.2: Dimensions for Scotch Yoke-driven prototype.

S021 motor driving the scotch yoke using a J.R. Kerr Inc. PIC-SERVO 3ph v.1 servo controller board and Z232-485 v.2 converter, as is illustrated in Figure2.9.

2.3 Solenoid-Driven Jet Prototypes

In the early stages of this investigation, two solenoid-driven synthetic jet prototypes were constructed to investigate the effect that an increased membrane throw would have on the force produced by a synthetic jet. As in the speaker coil actuation method, a rigid chamber with an orifice plate was used. Due to the potential risk of the long throw tearing the membrane, the rubber membrane was replaced with

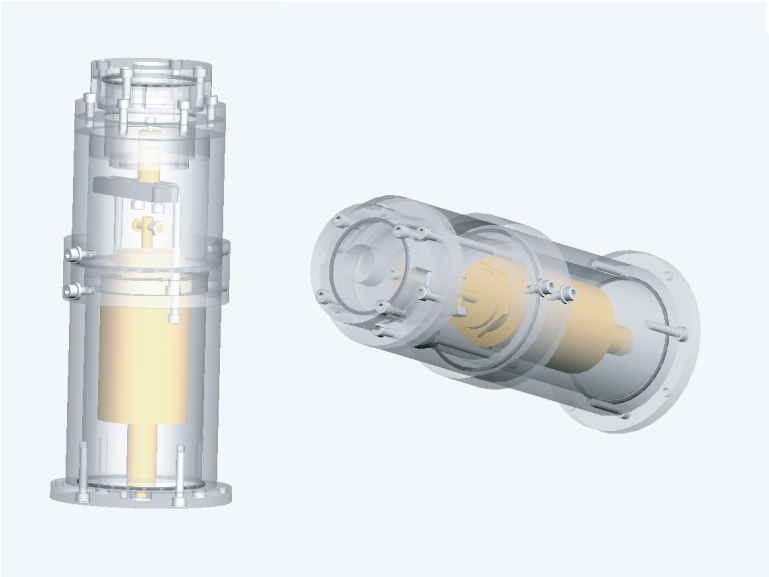

Figure 2.10: Solidworks CAD model of solenoid-driven prototype, courtesy of Joanna Cohen.

a solid disk. Two solenoid driven jets were built, one using a pull solenoid and one using a push solenoid. Springs were used to return the membrane/disk to its resting position. Unlike the speaker coil actuated synthetic jet, the solenoid jet only has one variable parameter: actuation frequency.

As will be shown in Chapter 5's discussion of thrust measurement experiments the throw, and thus force, produced by these prototypes fell dramatically with frequency. The work of Krieg et al. [27, 28] shows the same throw vs. frequency trend, yet their design allows for the exploration of a much greater range of frequencies. For these reasons, work with the solenoid jet prototypes was stopped in favor of focusing on the speaker coil prototype.

Chapter 3

Visualizing Synthetic Jet Flow

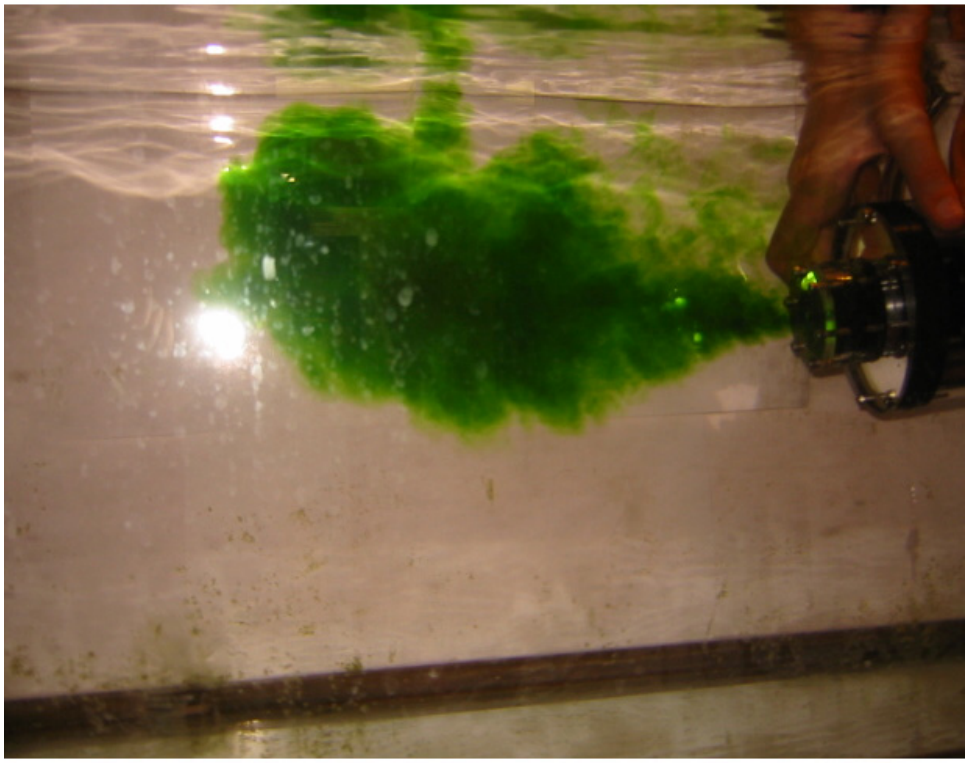

Figure 3.1: Dye flow visualization of synthetic jet thruster operation.

As only a small amount of flow visualization work has been published on synthetic jets in water [26], much remains to be learned about them. Prior to this study, no

flow visualization has been done inside the fluid chamber. Current understanding of the flow inside the fluid chamber is based on the results of simulations, such as those done by Rizzetta et al. [29]. This chapter presents qualitative visualizations of the inflow and outflow stages of a synthetic jet, confirming both the formation of vortex rings during the outflow and the formation of a stopping vortex inside the fluid chamber during the instroke. In this study, qualitative flow visualization techniques using colored dyes illustrate the dynamics of synthetic jet flow, that the overall flow structure is a jet (illustrated in Figure 3.1) , and that well defined vortex rings are created (shown in Figure 3.2). Additionally, the concept (and visualization) of a self-induced coflow is presented. Finally, these pieces are integrated into a more complete description of synthetic jet flow in water.

3.1 Outflow

The outflow phase of a synthetic jet, during which the jet's membrane or piston is pushing fluid out of the chamber, is the most studied aspect of the synthetic jet. As shown in many papers (including those by Smith and Glezer [25] and Crook and Woods [26]), vortex rings/pairs[1] are formed in this stage (a single ring/pair per outstroke).

Vortex ring formation during the outflow was present for all of our prototype jets. Figure 3.2 shows the rings formed using the scotch yoke prototype. In this

[1] As explained in Chapter 1, there are two main categories of synthetic jet orifices: circular and slit. The circular orifice produces a vortex ring during the out-stroke. The slit orifice, typically used to study 2D flow, produces a vortex pair, assuming the slit has a sufficiently large aspect ratio.

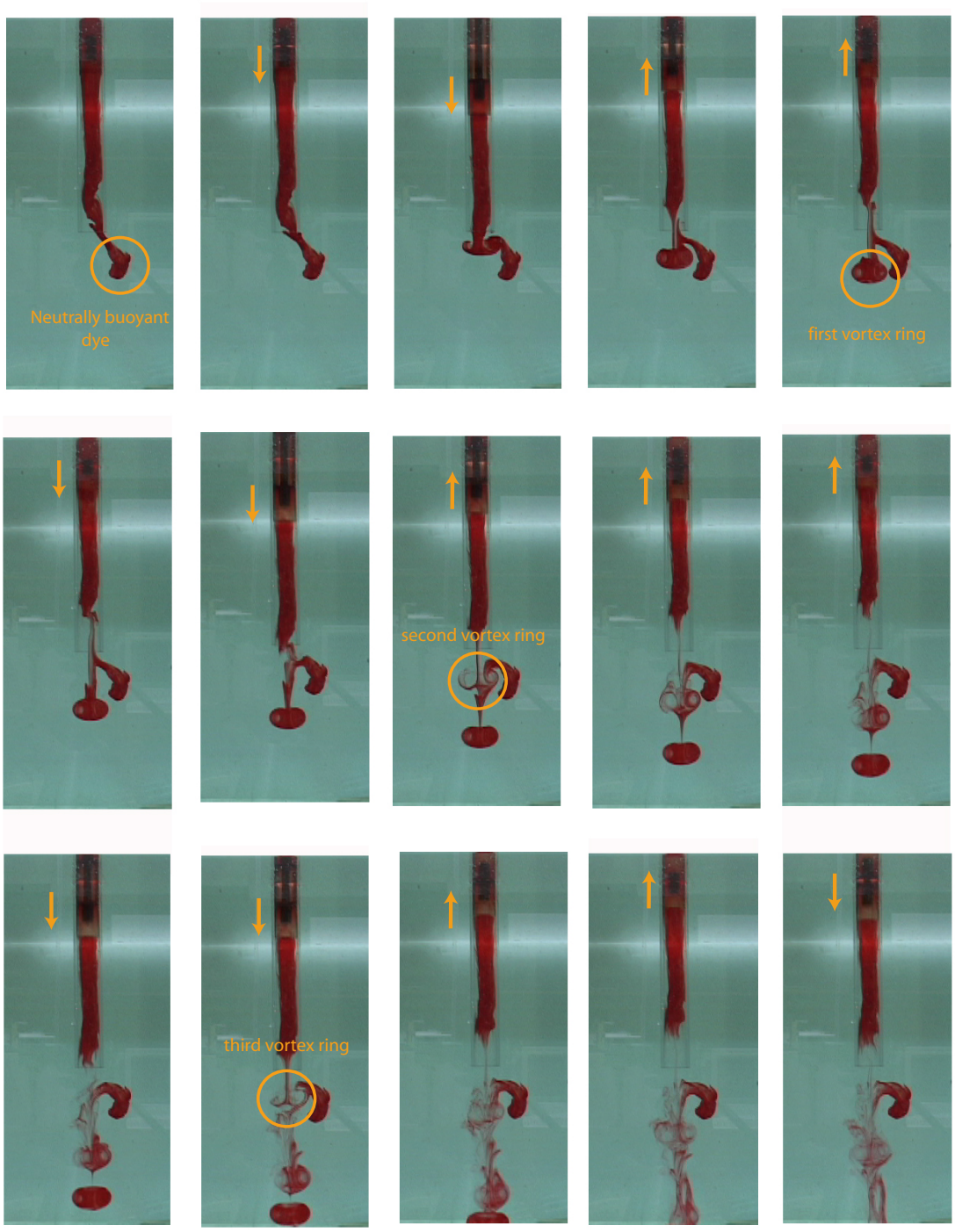

Figure 3.2: Dye flow visualization of a synthetic jet with an L/D stroke ratio of 2.

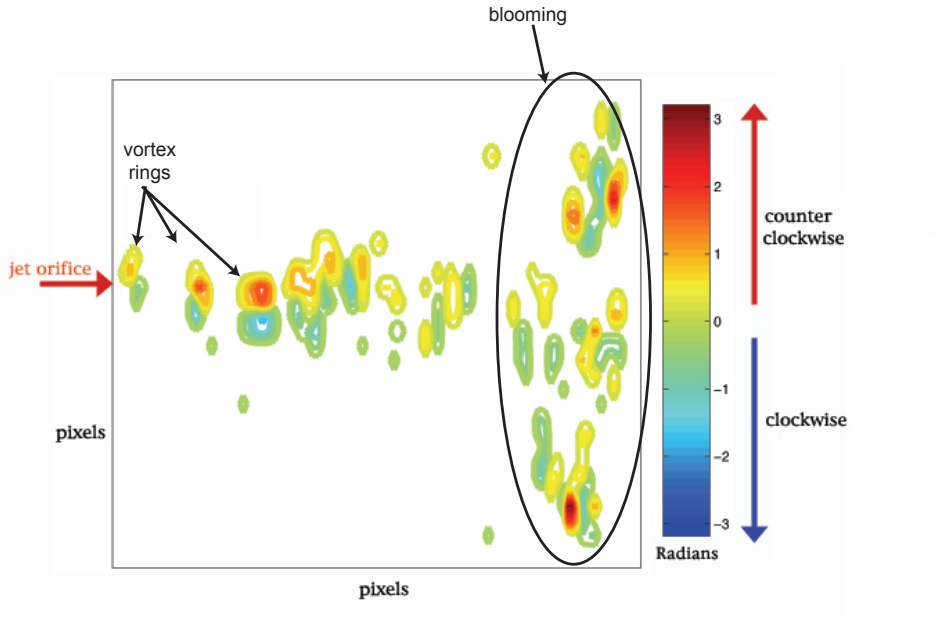

Figure 3.3: DPIV vorticity plot of voice coil-driven synthetic jet flow, color coded according to vorticity strength (positive vorticity means a clockwise rotating vortex and vice versa). The jet is flowing from left to right in this image.

case the cylinder was filled with an approximately neutrally buoyant dye, and a blob of this dye was also allowed to settle outside the orifice prior to starting the jet. Distinct rings were also seen in both digital particle image velocimetry (DPIV) and dye visualizations of the voice coil driven prototypes. Figure 3.3 shows a vorticity plot from a horizontal plane visualization of the voice coil jet actuated at 10 Hz.[2] Pairs of counter-rotating vortices are clearly visible in the field. In the near and intermediate field of the orifice, the flow has a clear vortex ring jet structure. In the far field, notice that the axial flow breaks up (the "blooming phenomena" described by Reynolds [65]).

[2]This DPIV image is from data taken in collaboration with Kayte Fischer, an undergraduate student at Caltech.

3.2 Inflow

Given that the primary use of synthetic jets has historically been in the area of flow control, the literature focuses predominantly on the flow outside the jet cavity. To gain a further understanding of the forces acting on the jet, a better understanding of the flow inside the chamber was needed. This was accomplished by performing DPIV on the Scotch Yoke-driven prototype.

Rizetta, Visbal, and Stanek [29] present a numeric simulation of the flow field inside a synthetic jet chamber. Being only the second numerical simulation of a synthetic jet (the first being that of Kral et al. [66]), theirs was the first to include the flow inside the chamber. It should be noted that their simulations were for a synthetic jet with a slit orifice and compressible fluid. Their model shows the formation of a stopping vortex within the chamber. During the instroke, their model predicts a counter-rotating vortex pair (as their simulations are for a slit orifice, this is truly a pair of vortices as opposed to a slice through the same vortex ring) forming at the inner edge of the jet orifice.

3.3 Inflow/Outflow Interaction

Figures 3.4 and 3.5 show a single in-out cycle of the scotch yoke jet. The flow is imaged using a laser sheet oriented along the jet axis and with the camera oriented perpendicular to this axis. The water is seeded using 14 micron glass particles. This experiment uses two 150 mW New Wave Gemini lasers and photographed 30 frames a

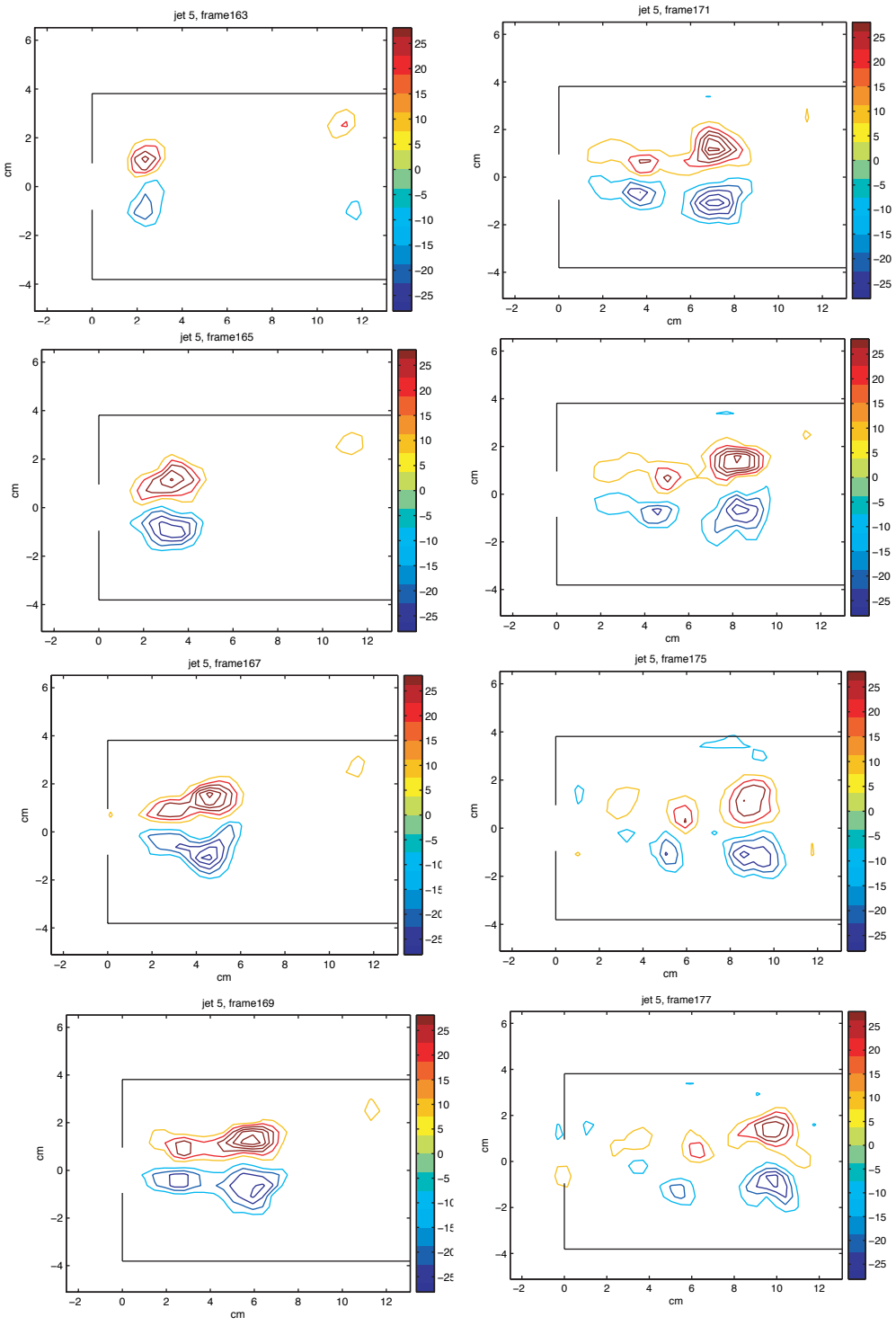

Figure 3.4: DPIV data taken inside of the scotch yoke synthetic jet chamber. The frames progress from top to bottom and left to right.

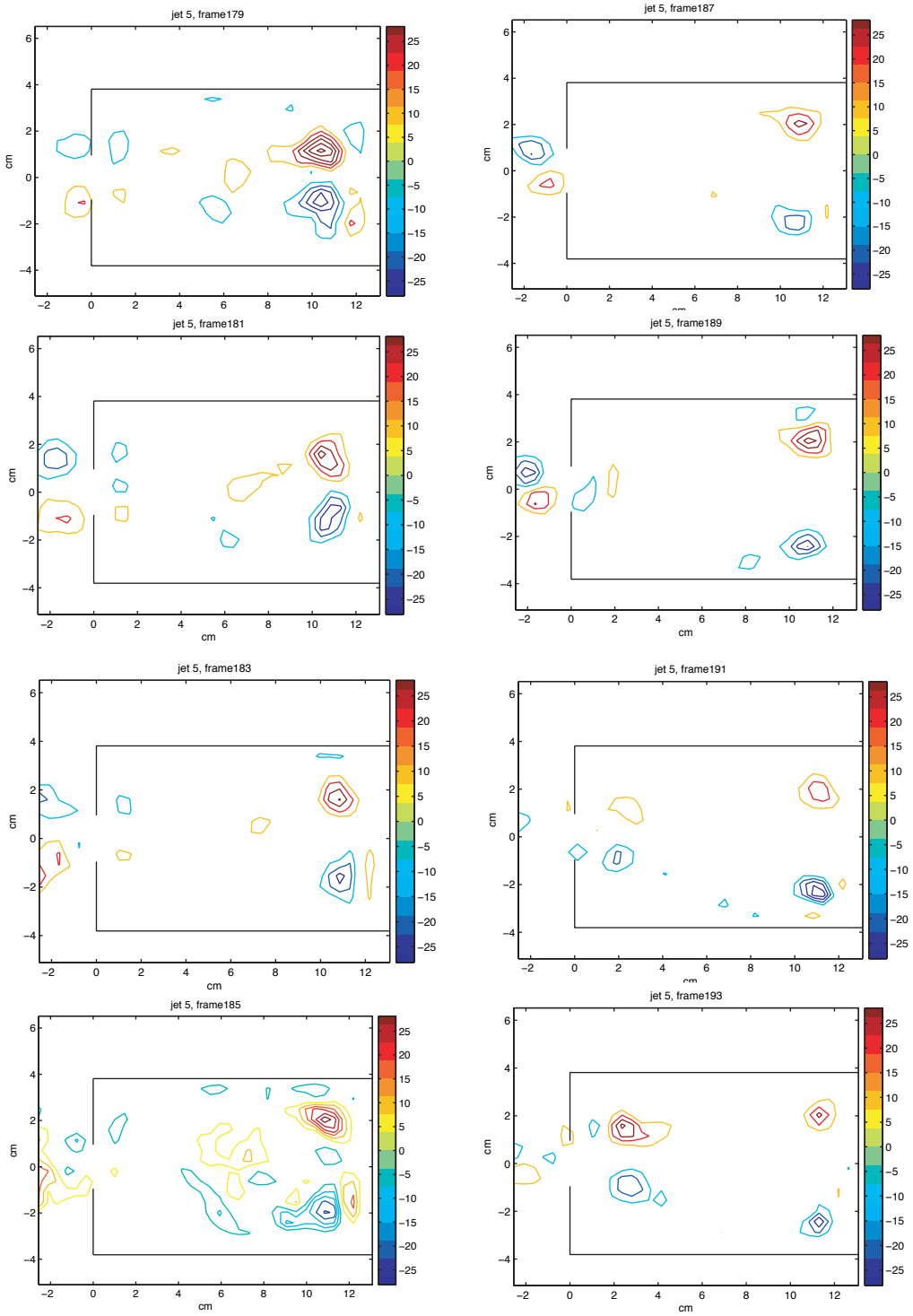

Figure 3.5: Page 2 of DPIV data taken inside of the scotch yoke synthetic jet chamber. The frames progress from top to bottom and left to right.

second using a CCD camera. From the photographs, cross-correlation of the particle locations in consecutive frames can be used to determine the local flow velocity. These values are then used to estimate an overall velocity field. Subsequently, the vorticity field can be calculated from the velocity field [67]. The motor of the scotch yoke was driven at a constant PWM (pulse width modulation).

In a sample run, several stages of jet evolution are evident. For example, the formation (and subsequent pinchoff) of a vortex ring inside the chamber is quite clear in frames 163-175. During frames 177-189, the formation and subsequent departure of a counter-rotating vortex ring outside the orifice can be seen. Finally, frames 189-193 show the formation of the next stopping vortex inside of the chamber. It is interesting to note that the previous chamber-internal vortex ring is still present, and visibly weakening, at the piston end of the chamber. Similarly, in frame 163 we can see a weakening vortex ring towards the right of the frame.

3.4 Self-Induced Coflow

As previously stated, the outflow vortex ring formation presented in Section 3.1 has been well documented both experimentally and theoretically in the literature. The inflow stopping vortex discussed in Section 3.2 has been predicted numerically. To the

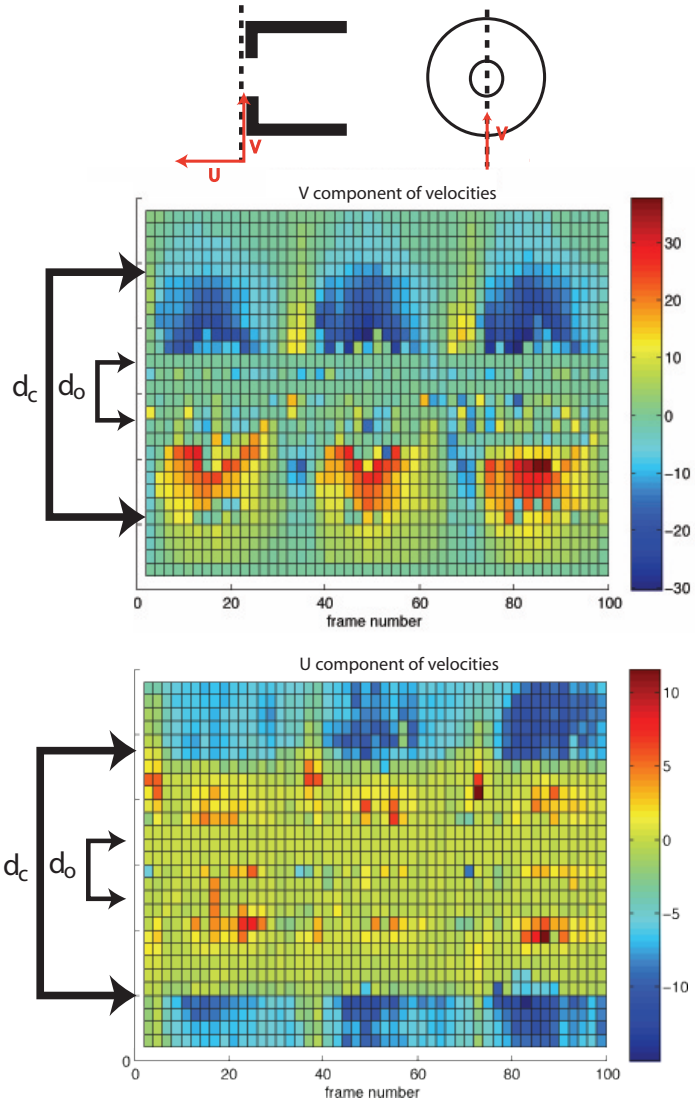

Figure 3.6: Velocities calculated along the line a ≈ 0 (just downstream of the orifice) over the course of three inflow/outflow cycles. The middle image (reproduced larger in Figure 3.7) shows velocities perpendicular to the jet axis, while the bottom image (reproduced larger in Figure 3.8) shows velocities parallel to the jet axis. The x axis of the plots represents these cross sections are from the same DPIV data presented in Appendix A.

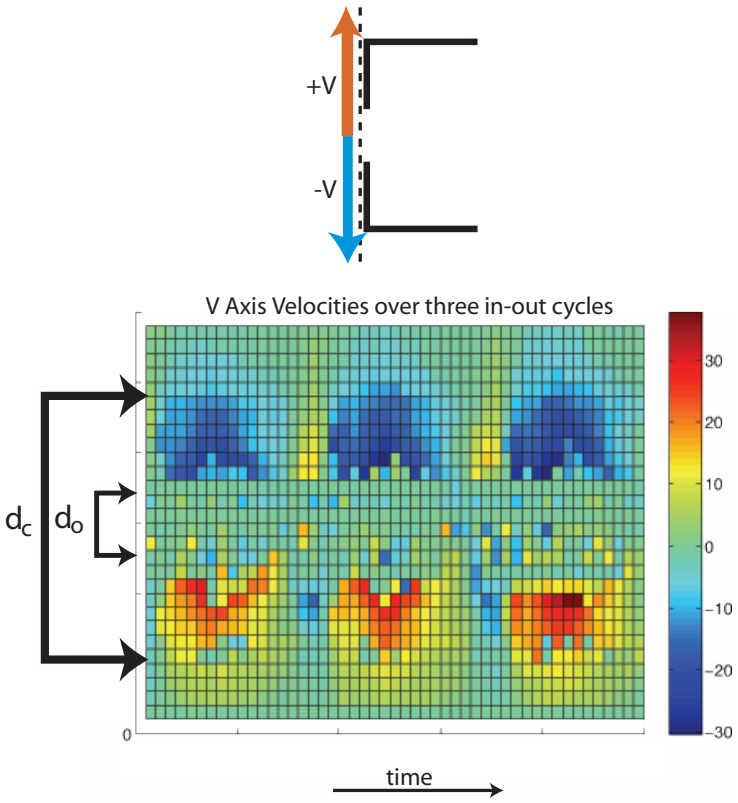

Figure 3.7: Plotting the v axis velocities over time. During the inflow, the flow along the orifice plate towards the orifice is very clear (the dark blue and red). During the outflow, the sign of these velocities switches, yet the duration and region of influence for the outflow is much smaller than during the inflow (the small yellow and blue regions) occurring, in time, between the large inflow velocities.

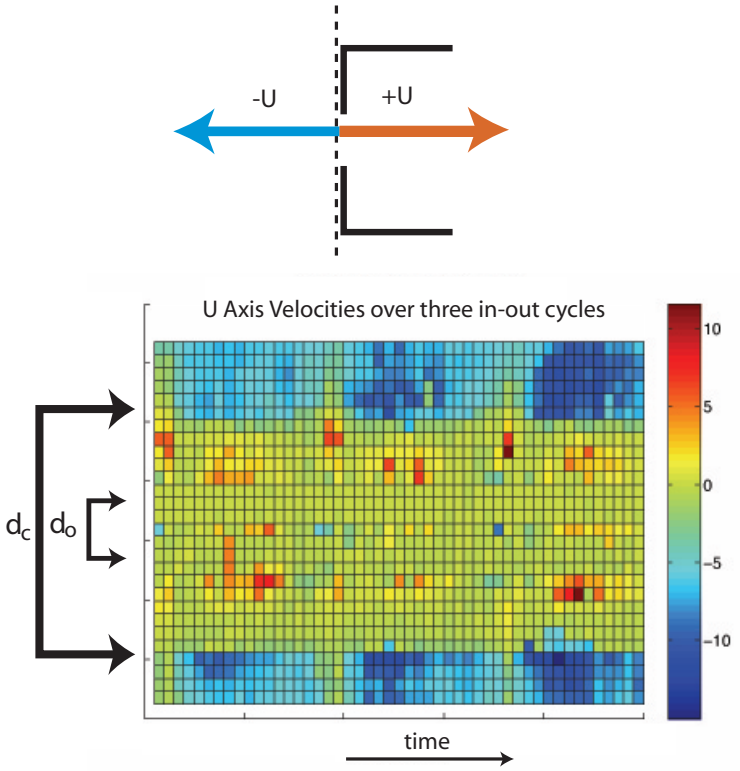

Figure 3.8: Plotting the u axis velocities over time. These velocities never change sign, thus indicating that the self-induced coflow's direction never changes. The magnitude of this flow is clearly larger during the inflow and approaches 0 during the outflow.

best of my knowledge, however, no one has previously modelled or visualized the flow external to the jet and upstream of the orifice. Most models have assumed an infinite plate with an orifice and chamber in it, and experimental setups have been designed to focus on the downstream flow. While visualizing the vortex ring formation inside the jet's fluid chamber, it became apparent that, in addition to forming the above-mentioned outflow and inflow vortices, the synthetic jet also induces flow upstream of the orifice plane.

After performing DPIV on the scotch yoke prototype at a frequency of ≈ 1.2 Hz, Figure 3.6 (A) was generated to illustrate how the radial velocities along the orifice plate during inflow and outflow. The schematics at the top of the figure show the line along which the velocities were calculated. Data for three inflow/outflow cycles is shown. The x-axis on both plots is the frame number (where there are 34 frames per cycle), while the y axis is the location along the v axis of the jet. The color represents the velocity at that point. The top image shows the radial velocities. It is quite clear that fluid is pulled into the orifice during the instroke. More surprising is the result that the flow spends most of the duration of the in/out cycle being pulled toward the orifice, even during the inflow. There is a brief period (frames 32-36, for example) where the flow is reversed, but the region over which this reversal acts is relatively small. Figure 3.6 (B) was produced to show the velocities in the u direction (parallel to the chamber walls). As is expected, the magnitude of the flow along the orifice plate is relatively small, and higher velocities are observed near the edges of the orifice during the inflow. We note that flow measurement on this line near, in,

and around the orifice are, at best, qualitative, as there is a high level of laser light reflection off of the orifice plate.

An interesting and unexpected result is the flow observed outside the chamber walls. At both the top and bottom of the plot, the v axis flow is negative throughout the entire flow cycle, which implies that the synthetic jet is inducing its own coflow. As can be seen in Figure 3.9, which shows a DPIV velocity frame during the inflow phase, the flow along the sides of the chamber is fairly evident. This presents an additional mechanism by which the synthetic jet can create a net thrust. This coflow is present at all points in the cycle, with the lowest magnitude velocities occurring during the outflow. The coflow may contribute to thrust in the $+u$ direction at all times. This will be discussed in greater detail in Chapter 4. The figures in Appendix A show the DPIV velocity fields for the entire plane over the course of a single inflow/outflow cycle.

3.5 Notes on the DPIV Data Presented in this Chapter

The DPIV experiments presented in this chapter were performed to corroborate our qualitative understanding of synthetic jet flow. However, the quantitative values of the results suggests that the trigger that synchronized the firing of the laser pairs may have been allowing the time between pairs to change over the course of individual experiments. This hypothesis is based on the following information. First, the

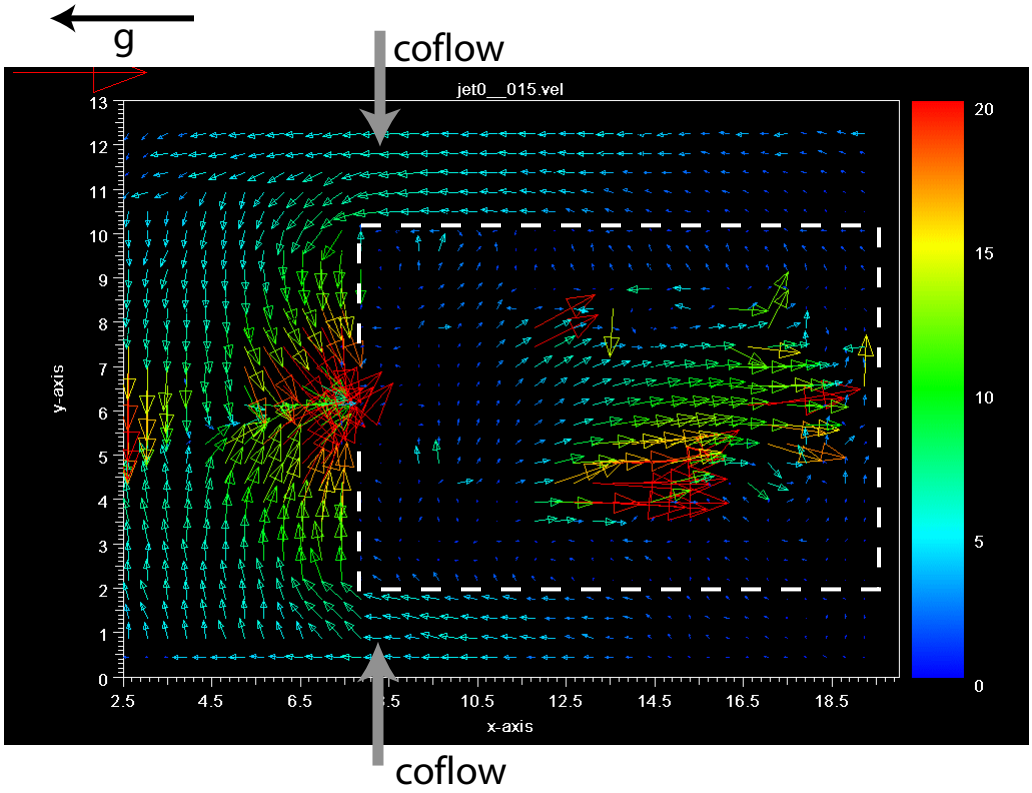

Figure 3.9: DPIV taken during inflow of the scotch yoke prototype shows evidence of a selfinduced coflow upstream of the orifice.

brightness of the individual photographic frames varies dramatically. When the timing is consistent, the brightness level of the frames is relatively constant. Secondly, there appears to be a drift in measured velocities that is consistent with the timing between lasers firing. Figure 3.10 shows the u component of velocity calculated at the same point in the flow field over the span of 120 frames, approximately 3 in-out cycles of the scotch yoke jet.[3] The blue line is the actual data. Notice that the velocities are increasing in magnitude. At first glance this could be attributed to the possible speeding up of the scotch yoke rotation rate. However, over the course of the three cycles pictured, the period remains constant, while the velocities increase. If the scotch yoke was speeding up, we would expect to see a decrease in the cycle period. The red line shows the data after being corrected for a linear drift, as we suspect was the case in this system. After this correction, the cycles look fairly similar to one another. The possibility that the increased velocities are a real phenomenon cannot conclusively be ruled out, in light of the above considerations. Thus, these DPIV studies are presented as a qualitative investigation of self-induced coflow and internal chamber vortex ring formation.

3.6 Summary of Flow Visualization Results

Combining the flow visualization observations from this chapter with the visualization information available in the literature, a general picture of the flow induced by a synthetic jet can be synthesized. This is pictured in Figure 3.11.

[3]Note that this plot is created from the same data set used to produce the figures in Appendix A.

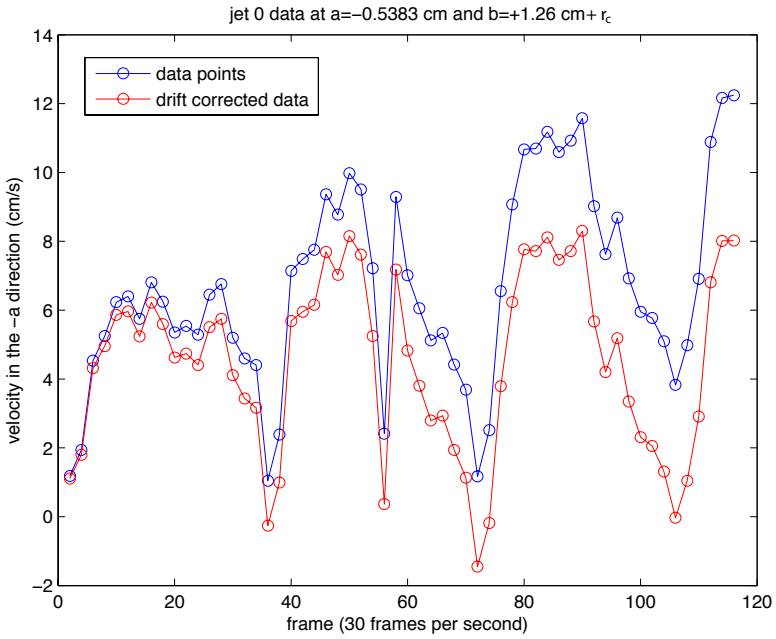

Figure 3.10: DPIV inferred velocity at a set point in the flow field over three inflow/outflow cycles.

(A): During the initial in-stroke of the membrane (or piston), a vortex ring forms at the inside of the orifice plate. Fluid is also pulled from upstream around the sides of the fluid chamber.

(B): The internal vortex ring pinches off and travels away from the orifice. Fluid is still being pulled from upstream around the exterior of the fluid chamber.

(C): As the membrane (or piston) pushes outward, another vortex ring forms at the outside edge of the orifice plate. This vortex ring is opposite in rotation to the one formed in step (A). Fluid is still being pulled from upstream around the sides of the fluid chamber. The vortex ring from steps (A) and (B) may still be present, but weakening, in the chamber.

(D): The vortex ring formed in step (C) pinches off and advects away from the orifice. Fluid is pulled from upstream around the sides of the chamber and may be entrained by this ring.

(E): As the membrane (or piston) pulls inwards, the process begins again. The ring ejected in step (D) will continue to travel away from the jet.

This simple schematic of synthetic jet flow will be used in Chapter 4 to create a force model for synthetic jets.

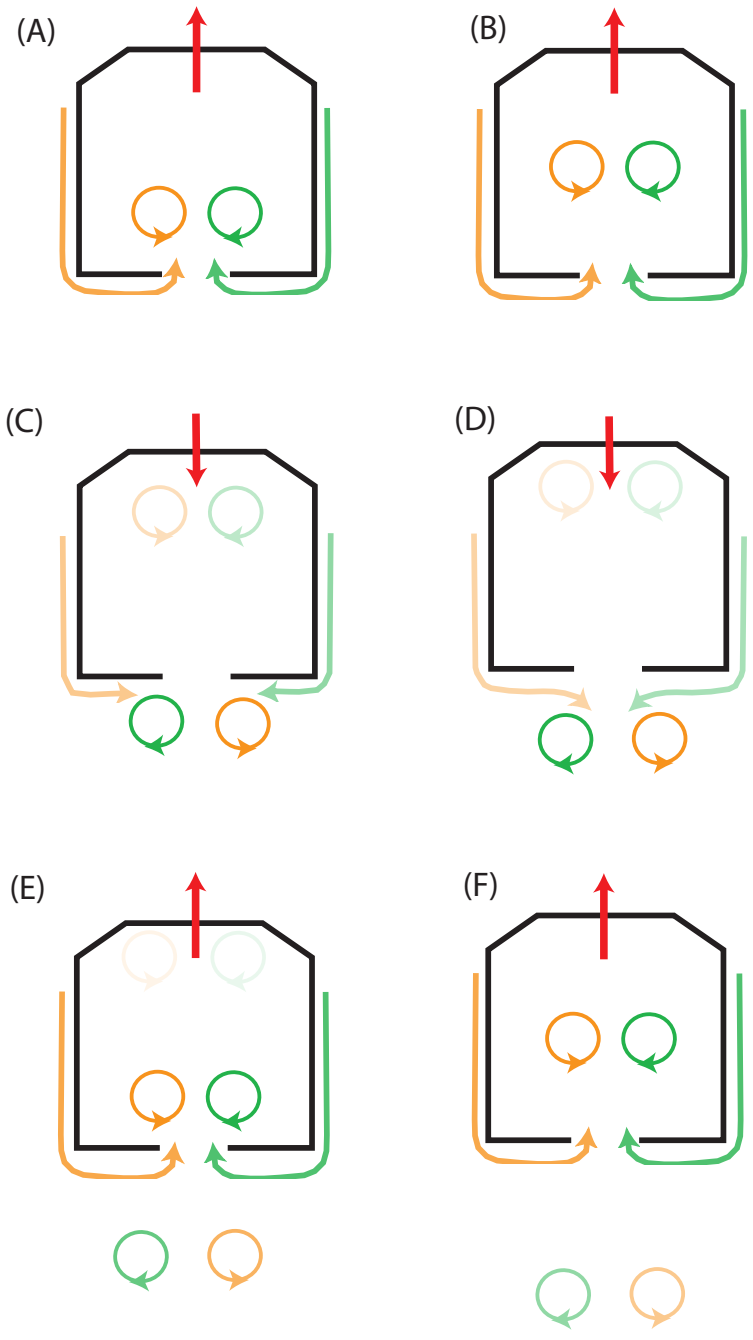

Figure 3.11: A schematic of synthetic jet flow.

Chapter 4

Modeling the Thrust Produced by a Synthetic Jet

As discussed in Chapter 1, most current synthetic jet modeling is done using computational fluid dynamics. Thus, there is not a standardly accepted closed form solution for the jet velocities nor for the thrust produced. However, for optimizing design of future devices, and for purpose of control design, such a model is needed.

There have been three models presented for force from a synthetic jet: those of Müller et al. [50, 51], Mohseni et al.[27, 28, 48, 56](both discussed in Chapter 1), and Polsenberg Thomas et al. [60, 61, 62]. As mentioned in Chapter 1, Müller's model is for a substantially different jet geometry as well as being for use in air. The models proposed by Mohseni [48] and Polsenberg Thomas [62] focus on the outflow of the synthetic jet and neglect any serious investigation of the inflow forces. Additionally, no models have incorporated the possible force contributions from self-induced coflow. This chapter will present a synthetic jet thrust model which incorporates inflow, outflow, and self-induced coflow.

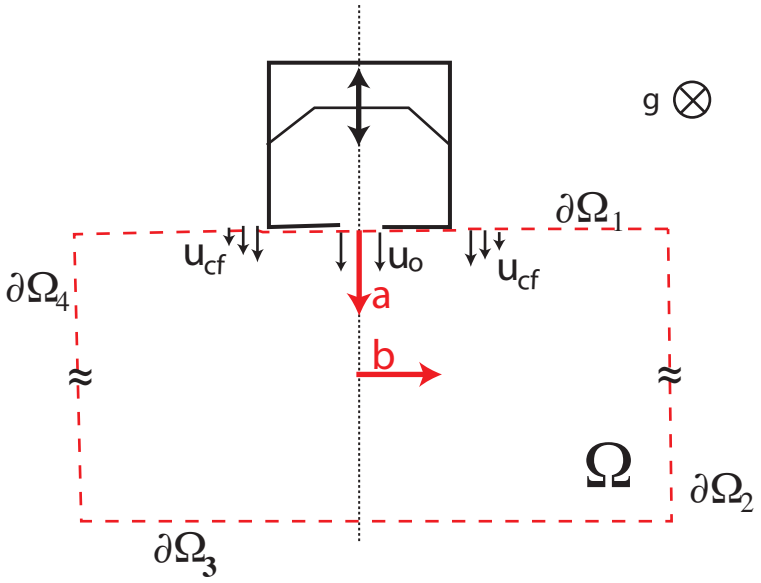

Figure 4.1: Control volume for synthetic jet force analysis.

4.1 Control Volume Analysis

As Newton's second law of motion must hold for this system, the time rate of change of the system's linear momentum must equal the sum of the external forces acting on it. An axisymmetric, fixed control volume, Ω, surrounding the synthetic jet flow downstream of the orifice plate (i.e., $a > 0$) is shown in Figure 4.1. The momentum equation for this volume of incompressible fluid can be written [68] as

$$\frac{\partial}{\partial t}\int_{\Omega}\rho\vec{u}\,dV + \int_{\partial\Omega}(\hat{n}\cdot\rho\vec{u})\vec{u}\,dA = F_{ext} + F_v - \int_{\partial\Omega}\hat{n}p\,dA + \int_{\Omega}\rho\vec{g}dV, \qquad (4.1)$$

where F_{ext} is the sum of external forces, F_v is the viscous forces, and $\vec{g}$ is the gravitational field. Following a similar control volume analysis performed by Krueger [69],

Equation 4.1 can be rewritten as

$$\frac{\partial}{\partial t}\int_{\Omega}\rho\vec{u}\,dV+\int_{\partial\Omega}(\hat{n}\cdot\rho\vec{u})\vec{u}\,dA=F_{ext}+\int_{\partial\Omega}\tau\hat{n}dA-\int_{\partial\Omega}\hat{n}p\,dA-\int_{\partial\Omega}\Phi g\hat{n}dV, \quad (4.2)$$

where $F_v=\int_{\partial\Omega}\tau\,\hat{n}\,dA$, τ is the shear stress tensor, and ϕ_g is the gravitational potential. The gravitational potential, ϕ_g, can be written as $\Phi_g=\rho gh-p_\infty\equiv-p_h$, where h is the vertical distance from the orifice center, $\vec{g}$ is acting in the $-\hat{z}$ direction, and p_∞ is the ambient pressure [69]. For this control volume, τ can be assumed to be zero. This reduces Equation 4.2 to

$$\begin{aligned}\frac{\partial}{\partial t}\int_{\Omega}\rho\vec{u}\,dV+\int_{\partial\Omega}(\hat{n}\cdot\rho\vec{u})\vec{u}\,dA &= F_{ext}-\int_{\partial\Omega}\hat{n}p\,dA-\int_{\Omega}\Phi g\hat{n}dV \quad (4.3)\\ &= F_{ext}-\int_{\partial\Omega}(p-p_h)\hat{n}dA.\end{aligned}$$

In the absence of external forces being applied to the jet, $F_{ext}=0$. Additionally, as gravity is acting in the $-\hat{z}$ direction, integrating ρgh over the axisymmetric control volume results in $\int_{\partial\Omega}(p-p_h)\hat{n}dA=0$. Thus, $\frac{\partial}{\partial t}\int_{\Omega}\rho\vec{u}\,dV+\int_{\partial\Omega}(\hat{n}\cdot\rho\vec{u})\vec{u}\,dA=0$. This dramatically simplifies Equation 4.1:

$$\frac{\partial}{\partial t}\int_{\Omega}\rho\vec{u}\,dV=-\int_{\partial\Omega}(\hat{n}\cdot\rho\vec{u})\vec{u}\,dA. \quad (4.4)$$

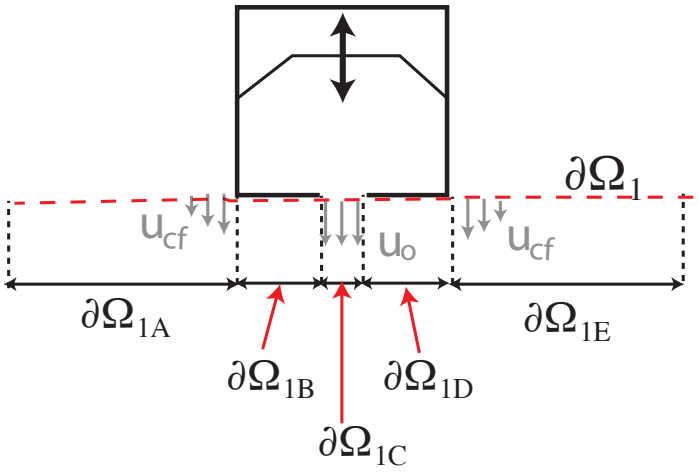

Figure 4.2: Details of surface $\partial\Omega_1$.

To easily assess the right hand side of this equation, it is convenient to break surface $\partial\Omega$ into components.

$$\begin{aligned} \rho\frac{\partial}{\partial t}\int_\Omega \vec{u}\,dV &= -\rho\int_{\partial\Omega}\vec{u}(\vec{u}\cdot\hat{n})\,dS \\ &= -\rho\int_{\partial\Omega_1}\vec{u}(\vec{u}\cdot\hat{n})\,dS - \rho\int_{\partial\Omega_2}\vec{u}(\vec{u}\cdot\hat{n})\,dS - \rho\int_{\partial\Omega_3}\vec{u}(\vec{u}\cdot\hat{n})\,dS \\ &\quad -\rho\int_{\partial\Omega_4}\vec{u}(\vec{u}\cdot\hat{n})\,dS. \end{aligned} \tag{4.5}$$

As the flow is axisymmetric about the orifice (given a cylindrical fluid chamber and circular orifice), $\int_{\partial\Omega_2}\vec{u}(\vec{u}\cdot\hat{n})\,dS = -\int_{\partial\Omega_3}\vec{u}(\vec{u}\cdot\hat{n})\,dS$. Thus, the flow through $\partial\Omega_2$ and $\partial\Omega_4$ can be ignored. Additionally, as $a\to\infty$, $\int_{\partial\Omega_4}\vec{u}(\vec{u}\cdot\hat{n})\,dS\to 0$. Thus, conservation of momentum simplifies to

$$\rho\frac{\partial}{\partial t}\int_\Omega \vec{u}\,dV = -\rho\int_{\partial\Omega_1}\vec{u}(\vec{u}\cdot\hat{n})\,dS. \tag{4.6}$$

By breaking the boundary $\partial\Omega_1$ into sections as shown in Figure 4.2, Equation 4.6

can be further simplified. As the boundary $\partial\Omega_1$ lies along the orifice plane, there is no flow through $\partial\Omega_{1B}$ and $\partial\Omega_{1D}$. The surface integral reduces to

$$\int_{\partial\Omega_1} \vec{u}(\vec{u}\cdot\hat{n})\,dS = \underbrace{\int_{\partial\Omega_1 A} \vec{u_{cf}}(\vec{u_{cf}}\cdot\hat{n})\,dS + \int_{\partial\Omega_1 C} \vec{u_o}(\vec{u_o}\cdot\hat{n})}_{\textbf{coflow}} + \underbrace{\int_{\partial\Omega_1 E} \vec{u_{cf}}(\vec{u_{cf}}\cdot\hat{n})\,dS\,dS}_{\textbf{orificeflow}} \quad (4.7)$$

where u_{cf} is the coflow velocity as discussed in Section 4.4, and u_o is the flow through the orifice.

This thesis proposes that there are at least three major thrust-producing components of synthetic jet flow: inflow, outflow, and self-induced coflow. Therefore, over a single in-out cycle, the total force produced by the jet can be written

$$\int_{t_1}^{t_3} F_{total}(\tau)\,d\tau = -\underbrace{\int_{t_1}^{t_2} F_{in}(\tau)\,d\tau}_{\textbf{Inflow}} + \underbrace{\int_{t_2}^{t_3} F_{out}(\tau)\,d\tau}_{\textbf{Outflow}} + \underbrace{\int_{t_1}^{t_3} F_{cf}(\tau)\,d\tau}_{\textbf{Coflow}}, \quad (4.8)$$

where t_1 marks the beginning of the instroke, t_2 marks the switch from instroke to outstroke, and t_3 is the end of the outstroke. Note that this is the same as Equation 4.7, with the orifice flow term broken in to inflow and outflow components.

4.2 Outflow

The outflow phase is the most important in terms of synthetic jet force production. During the membrane outstroke fluid is ejected through the orifice. As seen in the previous chapter's flow visualizations, this ejected fluid rolls up into a vortex ring which travels away from the jet. As work by Smith and Glezer [43], Mallinson et al. [45], and others has shown, the fluid flow achieves its maximum velocity during this

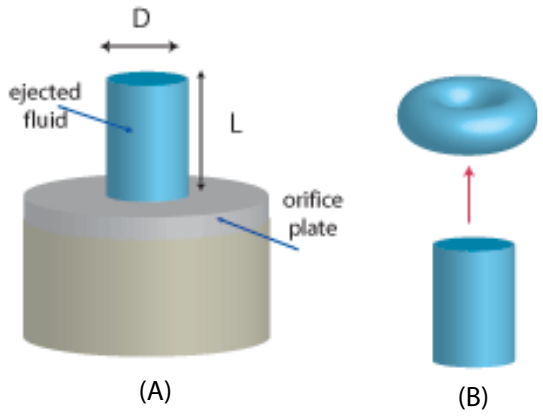

Figure 4.3: Slug Model: (A) A cylindrical slug of fluid is ejected from the orifice and (B) rolls up into a ring.

phase. Two methods for calculating the outflow force, F_{out}, are presented: the slug model and a quasi-steady model. As is show below, both models produce the same force and impulse.

4.2.1 Slug Model

As was mentioned briefly in Chapter 1, the slug model is often used in the piston-cylinder vortex ring formation literature. The slug model uses parameters from a cylindrical "slug" of ejected fluid (see Figure 4.3) to estimate the circulation of the produced vortex ring [32, 34, 36, 48, 70, 69]. Circulation is the line integral of velocity over a line enclosing a vortex; it is a measure of the vortex strength. The reaction force acting on the jet is higher for stronger vortices, so maximizing the circulation is an indirect way of maximizing thrust. This model computes the net impulse, I, of a single vortex ring formation and ejection.

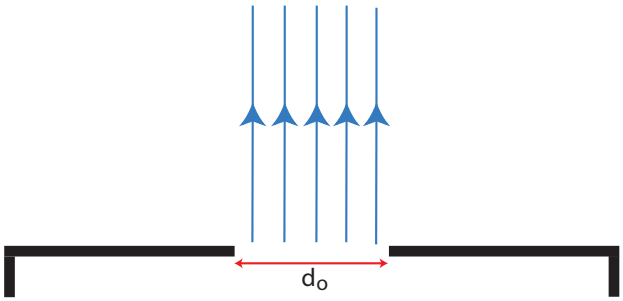

Figure 4.4: Treating the outflow as a quasi-steady jet simplifies the outflow modeling considerably.

The slug model impulse, I_{SM}, as presented by Krueger [69], is

$$I_{SM}(t) = \rho A \int_0^t U_J^2(\tau)\, d\tau, \tag{4.9}$$

where A is the orifice cross-sectional area, and U_J is the spatially average jet velocity. Thus, for the outflow of a synthetic jet with a circular orifice, this becomes

$$\begin{aligned} I_{SM}(t) &= \rho A_o \int_{t_2}^{t_3} u_{or}^2(\tau)\, d\tau \\ &= \rho \pi r_o^2 \int_{t_2}^{t_3} u_{or}^2(\tau)\, d\tau, \end{aligned} \tag{4.10}$$

where $t_3 - t_2$ is the duration (in seconds) of the outflow portion of the cycle.

4.2.2 Quasi-steady Model

An alternative to the slug model is a simple quasi-steady jet model, as illustrated in Figure 4.4. Unlike the slug flow models, which incorporate vortex ring formation, the quasi-steady model is concerned solely with mass flux and neglects vortex ring

formation. Using conservation of mass, the exit velocity of the fluid is calculated, and force is approximated using this velocity. The assumption is made here that u_{or} is constant across the entire area of the orifice. Shusser er al. [36] have considered the effect of boundary layer growth in a piston-cylinder setup on vortex ring generation. Accounting for this effect would cause u_{or} to vary over the orifice plane. However, the orifice thickness of the synthetic jets considered in this thesis is very small relative to L, reducing the importance of boundary layer effects within the orifice. The synthetic jet flow thrust model proposed by Müller et al. [50, 51] uses this approach for calculating outflow force.

Therefore, using the quasi-steady approach,

$$\begin{aligned} F_{out}(t) &= \rho A_o u_{or}^2(t) \\ &= \rho \pi r_o^2 u_{or}^2(t), \end{aligned} \tag{4.11}$$

Integrating $F_{out}(t)$ from t_2 to t_3,

$$\begin{aligned} I &= \rho A_o \int_{t_2}^{t_3} u_{or}^2(\tau)\, d\tau \\ &= \rho \pi r_o^2 \int_{t_2}^{t_3} u_{or}^2(\tau)\, d\tau \\ &= I_{SM} \end{aligned} \tag{4.12}$$

results in an impulse that is identical to the one solved for in Equation 4.10 using the slug model equation. Thus, this is the force, and impulse, that will be used for the outflow in the synthetic jet force model.

4.2.3 Reynolds Number

As was discussed in Chapter 1, synthetic jets can be created over a wide range of scales. One way to compare these jets is to look at their Reynolds number. The Reynolds number for a round synthetic jet, as used by Mallinson et al. [44],

$$Re_{do} = u_{or}\frac{d_o}{\nu} \tag{4.13}$$

is based on orifice diameter and mean exit velocity. This value is useful for comparing the performance of synthetic jets which are of different size and/or working fluid. It should be mentioned that most jellyfish, the inspiration for this project, typically operate over a range of Reynolds numbers between 100 and 10,000. Ctenophores operate between 1500 and 6000 [71], while there are a few species which have Reynolds numbers below 100. Synthetic jets, on the other hand, can be designed to cover an even larger span of Reynolds numbers.

4.3 Inflow

At first glance, it might appear that the equations for inflow should mirror those for outflow, the only difference being that during inflow the force would be exerted in the opposite direction. This would imply that for a symmetric forcing profile the inflow and outflow forces would cancel each other out.

As flow visualizations have shown, the inflow is not simply a reversal of the outflow. If that were the case, a jet would not be formed. The structure of the two flows differs

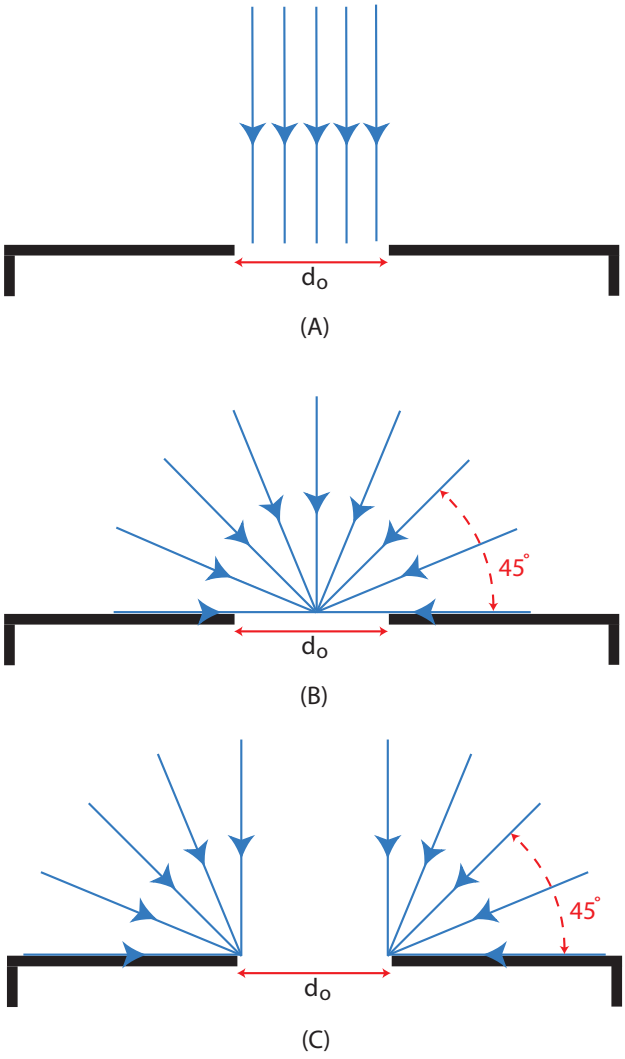

Figure 4.5: Three possible illustrations of jet inflow: (A) shows the inflow modeled as a reversal of outflow, (B) places a sink at the center of the orifice, and (C) also uses a sink; however, it is placed in such a way that fluid is drawn in along the edge of the orifice.

greatly. Despite the same volume of fluid passing through the orifice in both flows, the inflow is omni-directional whereas the outflow is directed.[1] Therefore, we can write the inflow force, F_{in}, as a fraction of F_{out}:

$$\begin{aligned} F_{in}(t) &= \eta\, F_{in} \\ &= \eta\, \rho\, \pi\, r_o^2\, u_{or}^2(t). \end{aligned} \tag{4.14}$$

We can define η as the fraction of the inflow force which is acting perpendicular to the orifice plate. Any portion of the force that is acting parallel to the plate can be neglected, as the flow is axisymmetric and thus those forces cancel out. If $\eta = 1$, implying that all inflow force vectors are perpendicular to the orifice plate, $F_{in}(t)$ has the same form as $F_{out}(t)$. This would imply that for a symmetric forcing profile, the magnitude of F_{in} and F_{out} would be equal, resulting in zero net thrust. We know that this is not the case from our own experimental results (presented in Chapter 5) and from the results of Krieg and Mohseni [27, 28]. Both sets of experiments found that a net thrust could be achieved even if the membrane moved inwards with the same velocity profile with which it moves outwards.

Rather than the uniformly directed flow pictured in Figure 4.3(A), Rathnasingham [46] suggests that the inflow of a synthetic jet acts as a sink. This possibility is roughly depicted in Figure 4.3(B). A more realistic schematic of the inflow is shown in Figure 4.3(C), as the simulations of Rizzetta et al. [29] and Mallinson and Reizes [72] suggest

[1] Blowing out a candle is a simple demonstration of this. You have probably never seen someone suck out a candle, yet you yourself have probably blown out candles. The same amount of air is inhaled and exhaled, yet the exhalation produces a more noticeable effect on the fluid flow in front of your mouth than inhalation.

that more fluid is sucked in around the outside of the orifice than in the center.

In our outflow model we assume that the fluid is ejected perpendicular to the orifice plate. Thus, all outflow vectors are at an angle of $\frac{\pi}{2}$ with respect to the orifice plate. For the inflow sink approximation, (pictured in Figures 4.3 (B) and (C), the average angle that the flow vectors make with the orifice plate is $\frac{\pi}{4}$. Again, given that the jet flow is axisymmetric, any radial component of force will cancel out, leaving only the streamwise component. Therefore,

$$\eta = \sin\frac{\pi}{4}.$$

Synthetic jet thrust is dependent on the asymmetry between the inflow and outflow phases. As was discussed in the previous section, symmetric inflow and outflow would result in zero net force. This inequality in directionality between inflow and outflow begins to explain the existence of a net force even when there is a symmetric forcing profile. However, the flow visualizations presented in Chapter 3 have raised the possibility of a third component to the net thrust equation: a self-induced coflow.

4.4 Self-induced Coflow

Our DPIV data implies that fluid is pulled from upstream during the instroke of the jet's membrane. This section explores a coflow model which is based on a simplified potential flow model where flow is driven by an inflow sink model. Given the radial symmetry of a sink, this model predicts a less directed flow than would be found by

modeling inflow using a quasi-steady jet.

4.4.1 Potential Flow Review

For a cylindrical synthetic jet, the flow field is axisymmetric about the orifice. Thus, we can use a 2D flow model and integrate over the volume. This section will present a brief summary of the elements of potential flow theory that will be used in our synthetic jet model. Potential flow makes the assumptions that the fluid flow is irrotational, i.e., $\omega = \bigtriangledown \times \vec{v} = 0$, and incompressible, i.e., $\bigtriangledown \cdot \vec{v} = 0$[73]. More information on the topic can be found in Granger [74] as well as most introductory fluid dynamics books.

For two-dimensional motion of irrotational, inviscid fluid flow, where ϕ is the velocity potential and ψ is the stream function,

$$\frac{\partial \phi}{\partial x} = \frac{\partial \psi}{\partial y}$$

and

$$\frac{\partial \phi}{\partial y} = -\frac{\partial \psi}{\partial x}.$$

Note that these are the Cauchy-Riemann relationship equations. The **complex velocity potential** of the flow is defined as $F = \phi + i\psi$. Thus,

$$real(F) = \phi$$

and

$$imaginary(F) = \psi.$$

Recalling that $z = x + iy$, we can define a function, $W = \frac{dF}{dz}$, known as the **complex velocity**. It can be shown that W can be expressed in terms of the velocity field in the Z plane (where u and v are, respectively, the x and y velocity components. Expanding $dF = d\phi + id\psi$ gives

$$dF = udx + vdy + i(-vdx + udy) = (u - iv)dz.$$

Thus,

$$W = \frac{dF}{dz} = u - iv.$$

It should be noted that, in polar coordinates, $W = (v_r - iv_\theta)\, e^{-i\theta}$.

4.4.2 Sink

In order to model a synthetic jet's inflow, it is necessary to know F and W for a sink. In $2D$, a sink is simply the center point of a purely radial inward flow, as shown in Figure 4.6. Given that the jet's flow is axially symmetric, we can define the flow rate, q, as

$$q = \int_0^{2\pi} v_r r d\theta,$$

where v_r is the radial velocity. As v_r is constant for all θ, regardless of r, $q = 2\pi r v_r$. Solving this equation for v_r gives $v_r = \frac{q}{2\pi r}$. We can then use v_r and the knowledge

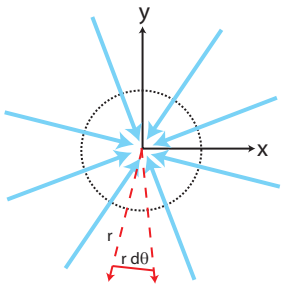

Figure 4.6: A sink is produces an axisymmetric, purely radial, flow.

that v_θ is equal to zero to solve for W:

$$\begin{aligned} W(r,\theta) &= (v_r - iv_\theta)e^{-i\theta} \qquad (4.15)\\ &= \left(\frac{q}{2\pi r} - 0\right)e^{-i\theta} \\ &= \frac{q}{2\pi r}e^{-i\theta}. \\ W(z) &= \frac{q}{2\pi}\frac{1}{z}. \qquad (4.16) \end{aligned}$$

The complex velocity potential for a sink can then be found by integrating $W(z)$ with respect to z: $F(z) = \frac{q}{2\pi}\ln z$.

4.4.3 Conformal Mapping

The equations for a sink on a flat plate are well known. The equations for a sink offset from a corner (as shown in Figure 4.7) are more complicated. Thus, solving for a sink on a flat plate and mapping the solution to the more complicated geometry simplifies the problem substantially.

Riemann's Mapping Theorem [75] states that for a simply connected domain, D,

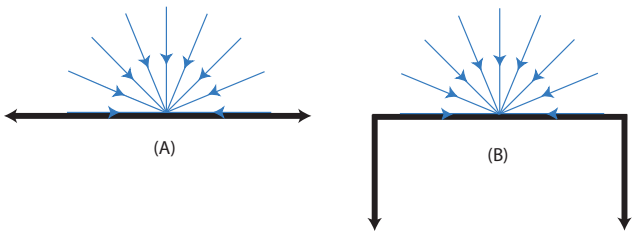

Figure 4.7: The potential flow calculations for a sink on a flat plate (A) are much simpler than those for the geometry shown in (B).

in the Z plane, there exists a univalent function, $f(z)$, such that $c = f(z)$ maps D onto the disk $|c| < 1$. Let Γ be the piecewise linear boundary of a polygon in the C plane, and let the interior angles at successive vertices be $\alpha_1\pi$, ..., $\alpha_n\pi$. The Schwarz-Christoffel Theorem states that this transformation can be written as

$$\frac{dc}{dz} = \gamma(z - k_1)^{\alpha_1 - 1}(z - k_2)^{\alpha_2 - 1} \dots (z - k_n)^{\alpha_n - 1}, \tag{4.17}$$

where γ is a complex number and $k_1, \dots, k_n$ are real numbers. Thus, the polygon is mapped to the upper half of the Z plane. The vertices of the polygon, K_1,K_2,...,K_n, are mapped to the points $k_1, \dots, k_n$ on the x axis [75].

Such a mapping, which preserves local angles, is called a *conformal map*. More precisely, a mapping, $w = f(z)$, is considered conformal if, for every point z_0, $f(z_0)$ is analytic and $f'(z_0) \neq 0$ [76].

4.4.4 Mapping Synthetic Jet Geometry

As the flow around a synthetic jet is axisymmetric, it can be treated as a $2D$ problem. If the jet orifice is centered at the origin of the axes, with the jet centerline running

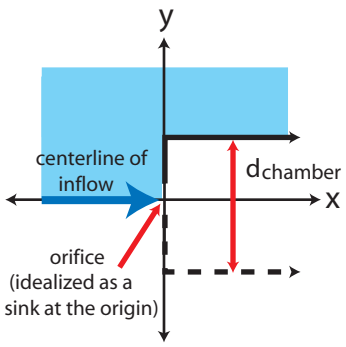

Figure 4.8: Orientation of synthetic jet in mapped fluid region.

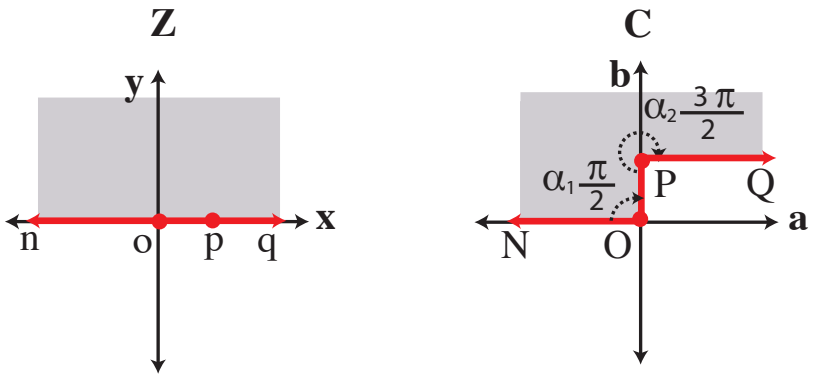

Figure 4.9: Desired mapping from Z plane to C plane.

along one of the axes, we only need to worry about half the plane. Figure 4.8 shows the jet superimposed over such a map.

As discussed in the previous section, such a map can be created using the Schwarz-Christoffel transformation. It should be noted that this transformation puts the boundary along the horizontal axis downstream of the jet. This is not a problem, as it enforces symmetry. Additionally, as flow is allowed along (but not through) the boundary, the flow along it can be calculated as follows:

$$\begin{aligned}\frac{\partial c}{\partial z} &= \gamma(z-k_1)^{\alpha_1-1}(z-k_2)^{\alpha_2-1}\dots(z-k_n)^{\alpha_n-1} \\ &= \gamma(z-0)^{(\frac{1}{2}-1)}(z-1)^{(\frac{3}{2}-1)} \\ &= \gamma(z-0)^{-\frac{1}{2}}(z-1)^{\frac{1}{2}} \\ &= \gamma\frac{\sqrt{z-1}}{\sqrt{z}}. \end{aligned} \tag{4.18}$$

Integrating with respect to z gives

$$c = h + \gamma\frac{(z-1)\sqrt{z} - \sqrt{z-1}Log\left[\sqrt{z-1}+\sqrt{z}\right]}{\sqrt{z-1}}, \tag{4.19}$$

where h is a constant ,and γ is a complex number.

For convenience, the choice was made to map the origin of the Z plane to the origin of the C plane:

$$c(0) = h - i\frac{\gamma\pi}{2} \tag{4.20}$$

$$h = i\frac{\gamma\pi}{2} \tag{4.21}$$

$$c(z) = i\frac{\gamma\pi}{2} + \gamma\frac{(z-1)\sqrt{z} - \sqrt{z-1}Log[\sqrt{z-1}+\sqrt{z}]}{\sqrt{z-1}} \tag{4.22}$$

Varying γ allows us to adjust the position point P (see Figure 4.9), thus choosing the synthetic jet's diameter. Point P in the C plane is the mapping of point z=1 in the Z plane; thus γ should be chosen such that $c(1) = ir_{oc}$ (where r_{oc} is the outer radius of the fluid chamber).

$$c(1) = i\frac{\gamma\pi}{2} = ir_{oc} \tag{4.23}$$

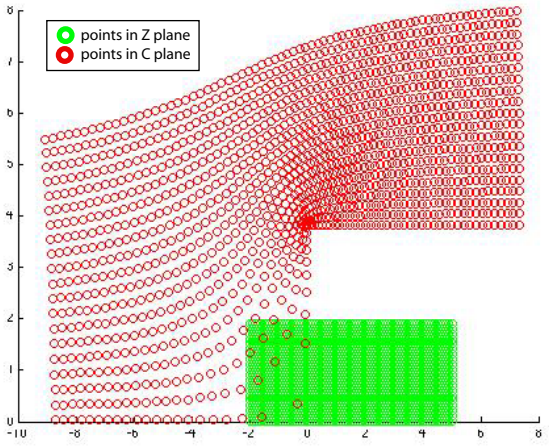

Figure 4.10: The result of the mapping described in Equation 4.25. The green circles are a set of points in the Z plane, and the red circles are the same points after the mapping.

$$\gamma = \frac{2}{\pi} r_{oc} = \frac{d_{oc}}{\pi} \tag{4.24}$$

The final Z plane to C plane mapping is:

$$\frac{\partial c}{\partial z} = \frac{d_{oc}}{\pi} \frac{\sqrt{z-1}}{\sqrt{z}} \tag{4.25}$$

$$c(z) = i\frac{d_{oc}}{2} + \frac{d_{oc}}{\pi} \frac{(z-1)\sqrt{z} - \sqrt{z-1} Log\left[\sqrt{z-1} + \sqrt{z}\right]}{,} \sqrt{z-1} \tag{4.26}$$

and can be seen in Figure 4.10.

This model treats the synthetic jet's inflow as a time varying sink placed in the center of the orifice, as shown in Figure 4.11. The sink strength, q, is a function of the orifice area and outflow velocity. For simplicity, I have made the assumption that the outflow velocity is uniform over the area of the orifice. A future model

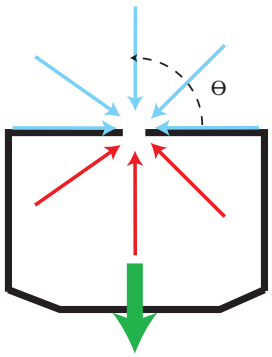

Figure 4.11: If the inflow is treated as a sink, the source strength must be scaled to account for the fact that fluid is only entering from $0 \leq \theta \leq \pi$.

could incorporate issues such as boundary layer formation, which would lead to a non-uniform velocity distribution. By definition, fluid enters a sink axisymmetrically. In the case of a synthetic jet, however, we know that physically all of the fluid is entering only half of the "sink." This does not pose a problem in our model, as the other half of the flow is on the other side of the conformal map boundary (across which fluid cannot flow). To account for this, the value of q must be double what it would be if the flow was entering truly axisymmetrically:

$$q \;=\; 2\, d_o\, u_{or}. \tag{4.27}$$

According to Brown and Churchill [76], "under a conformal transformation, a source or sink at a given point corresponds to an equal source or sink at the image of that point." Given our mapping, the sink occurs at the origin. Thus, the complex potential is

$$F(z) = -\frac{q}{2\pi} Log(z), \tag{4.28}$$

where q is the strength of the sink. Differentiating F with respect to z results in the complex velocity, W:

$$W(z) = \frac{dF}{dz} = -\frac{q}{2\pi z}. \tag{4.29}$$

The complex velocity now needs to be mapped into the C plane. A small complication arises from attempting to invert $c(z)$. There is no simple closed-form equation for $z(c)$; thus $W(c)$ must be written as a function of z. As c is also a function of z, this does not pose a problem. The velocity field $W(c(z))$ can then be plotted with respect to $c(z)$.

$$\begin{aligned} W(c(z)) &= W(z)\frac{\partial c}{\partial z}^{-1} \\ &= \frac{dF}{dz}\frac{\partial z}{\partial c} \\ &= \frac{dF}{dz}\frac{\partial c}{\partial z}^{-1} \\ &= -\frac{q}{2\pi z}\frac{\pi}{d_{oc}}\frac{\sqrt{z}}{\sqrt{z-1}} \\ &= -\frac{q}{2d_{oc}}\frac{\sqrt{z}}{z\sqrt{z-1}} \end{aligned} \tag{4.30}$$

A sample plot of W can be seen in Figure 4.12.

When calculating the thrust produced by a synthetic jet, only the real part of W adds a contribution, as the imaginary part is axisymmetric along the a axis, as shown in Figure 4.13. Thus, we are interested in the magnitude of $u_{cf} = |real(W)|$. The sink strength, q, is merely a scaling factor, thus the case $q = 1\frac{m^2}{s}$ can be considered. Then, given a constant jet geometry (i.e., an unchanging d_{oc} value) the results can be scaled for any sink strength. This nondimensional scaling factor will be called q_s.

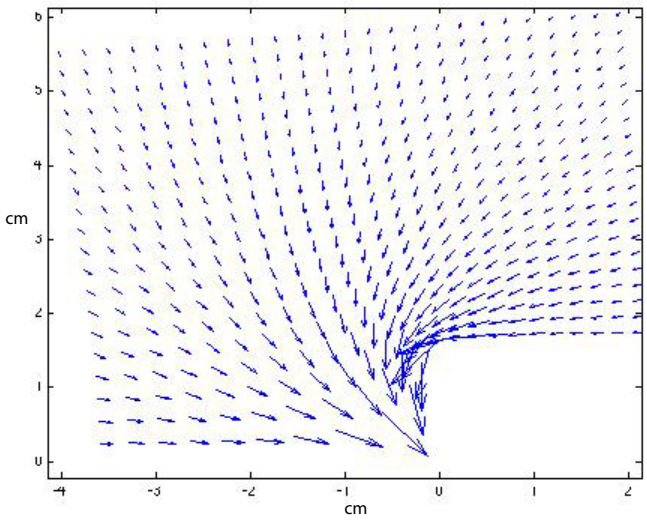

Figure 4.12: Transformed flow in the C plane.

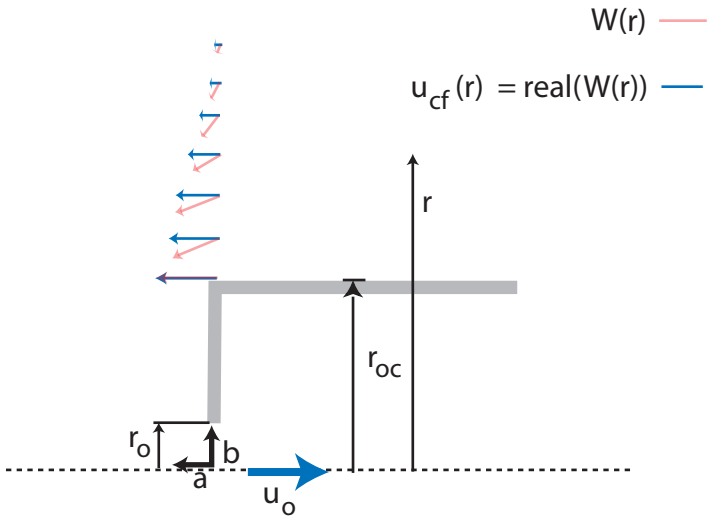

Figure 4.13: The magnitude of u_{cf} varies as a function of r, the distance from the orifice's center.

To find F_{cf} using the chosen control volume (Figure 4.1), it is necessary to calculate the value of u_{cf} for points along the line $a = 0$ (which physically represents a line from the orifice origin to ∞ lying on the surface of the orifice plate). To do this, it is necessary to find the line in the Z plane which maps to this line in the C plane. Given that there is no closed form solution for $z(c)$, a numerical method must be used to find the Z plane points which map to $a = 0$ in the C plane. A brute force way of doing this is to create a very dense grid of points in the Z plane, map these points to the C plane, and then select the points that lie on the line $a = 0$.[2] Once this has been done, u_{cf} can be plotted as a function of b. On the jet, b represents the distance from the orifice's center along a line perpendicular to the centerline of the jet. To simplify the discussion in this section, calculations will be made using r as a variable, where $r = b$, as this is a more intuitive description for the radial distance from the orifice's center.

Along Ω_1, $r_o \leq r < r_{oc}$ lies along the orifice plate, and thus no flow travels across that boundary. Therefore, $u_{cf}(r) = 0$ for $r_o \leq r < r_{oc}$. While there is flow along this surface, it is due to orifice flow, not coflow. As r_{oc} increases the velocity at $r = r_{oc}$ decreases. This is to be expected, as sink-induced velocities decrease with distance from the sink. Figure 4.14 shows u_{cf} as a function of r (distance from the orifice center) for three values of r_{oc}: 5 cm, 10 cm, and 15 cm. Plotting u_{cf} this way

[2]This method can be simplified, as the points in the Z plane that map to the points $a = 0$ are located on a roughly quadratic curve in the Z plane. Thus, the mapping process can be sped up by mapping a less dense grid of points in the Z plane to their respective C plane points, then plotting (in the Z plane) the points which correlated to the desired line in the C plane. A quadratic curve can be fit to these points. Then, points lying on, and near, this line can be mapped to the C plane. The result should be points which lie on or near the line $a = 0$. Points from this new set can then be selected based on how close to $a = 0$ they lie.

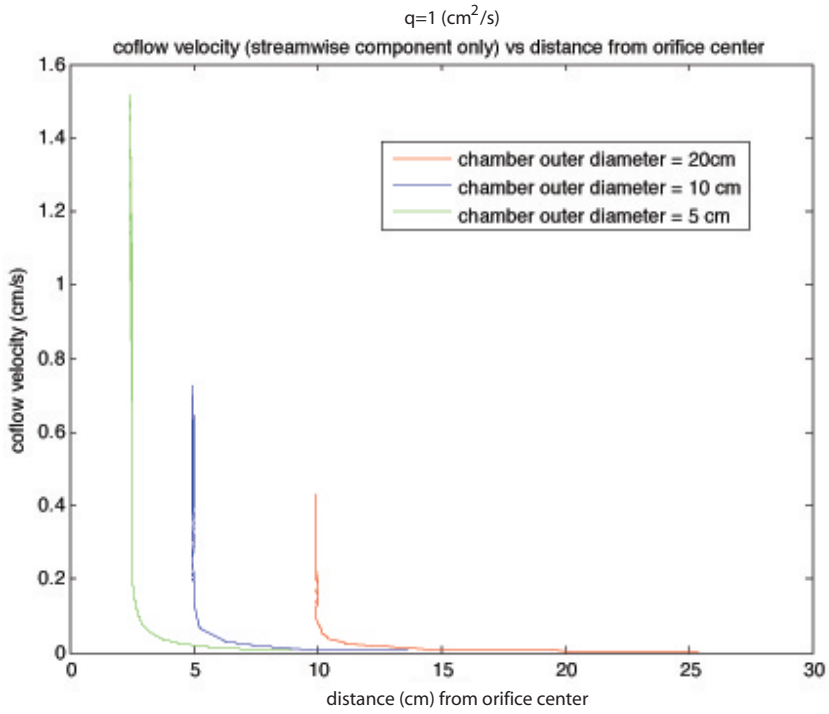

Figure 4.14: As the fluid chamber's outer radius (r_oc) increases, the coflow velocity at the point ($r = r_{oc}$) decreases.

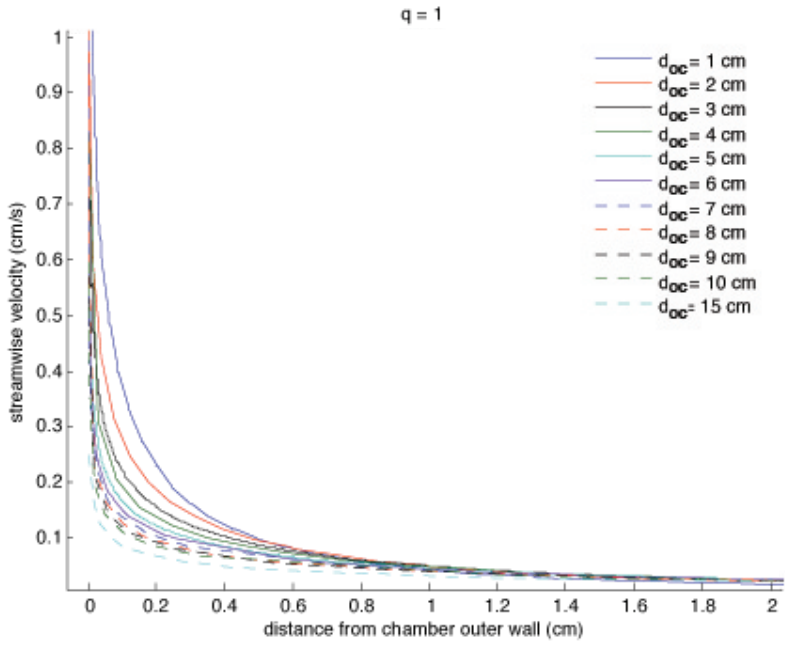

Figure 4.15: As the fluid chamber's outer radius (r_{oc}) increases, the decay rate of $u_{cf}(r - r_{oc})$ increases.

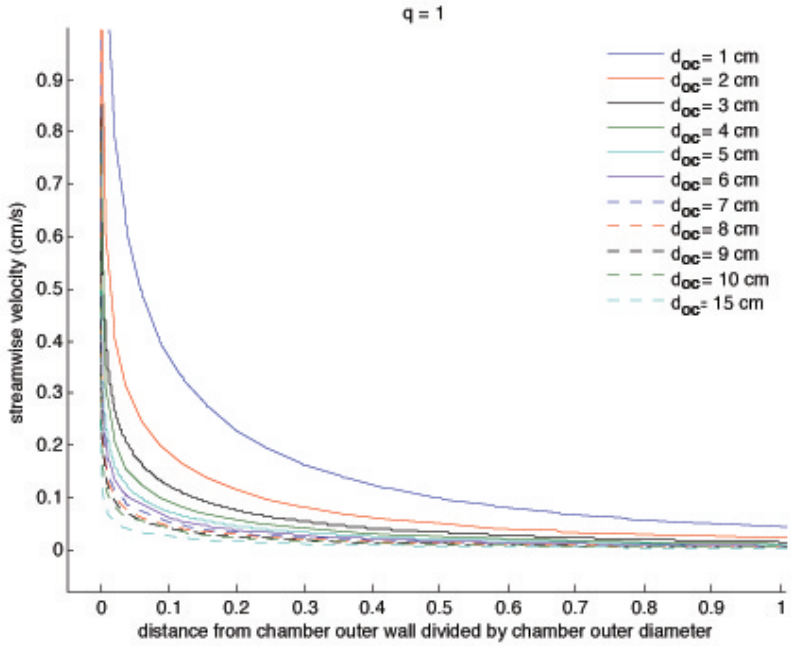

Figure 4.16: As the fluid chamber's outer radius, r_{oc}, increases, the decay rate of $u_{cf}(r - r_{oc})$ as a function of $\frac{(r-r_{oc})}{d_c}$ increases.

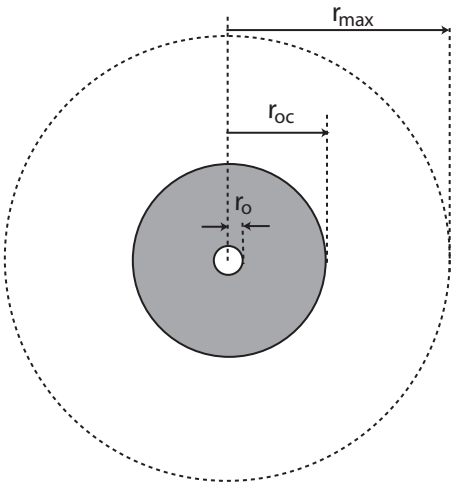

Figure 4.17: To calculate F_{cf}, u_{cf} is integrated over an annulus with an inner radius of r_{oc}.

illustrates the change in coflow velocity magnitude, however, it is harder to see the relative rates of decay. Figure 4.15 shows u_{cf} plotted as a function of $(r - r_{oc})$, the distance from the outer wall of the chamber. This plot clearly shows that the rate of velocity decay, as a function of distance from the outer wall, increases as the chamber outer diameter increases. A third way of looking at u_{cf} is with respect to r/d_{oc},(i.e., the coflow velocity normalized by the orifice outer diameter), as is shown in Figure 4.16.

The force contribution from u_{cf} can be found by integrating over the annulus illustrated in Figure 4.17, where r_{oc} is the inner radius, and the outer radius goes to ∞.

$$F_{cf} = \rho A u_{cf}^2 \tag{4.31}$$

$$= \rho \int_0^{2\pi} \int_{r_{oc}}^{\infty} u_{cf}^2 \, r \, dr \, d\theta$$

The lack of a closed form representation for u_{cf} necessitates the use of a numerical method to solve for F_{cf}. At least two approaches can be taken. One would be to attempt to fit a function $u_{cf}(r)$ to the points found using the numerical method discussed above and then integrate from r over $[r_{oc}, \infty]$. An alternative is to numerically integrate the points, skipping the curve fitting step. Both of these methods pose distinct challenges. The latter approach is presented in the next section.

4.4.5 Numerical Integration of Coflow Force

The numerical integration method requires an outer limit of integration to be chosen. Figures 4.15 and 4.16 show that u_{cf} quickly approaches 0 as r increases. However, as r_{oc} increases, the area of the annulus also increases. Therefore, even a small value of u_{cf} can produce a significant force if acting over a large enough area. For this reason, choosing a constant distance $(r - r_{oc})$ as an upper limit of integration for all r_{oc} can result in physically unrealistic forces for large r_{oc}. This raises a problem with the potential flow approach to calculating u_{cf}: potential flow neglects viscous effects. For a real fluid, $u_{cf}(r)$ will decay more rapidly than predicted by potential flow due to viscosity. Similarly, friction along the orifice plate will reduce the value of $u_{cf}(r = r_{oc})$. Therefore, this analysis should be considered only as an approximation of self-induced coflow effects.

To find the force contribution from the coflow, the streamwise component of the

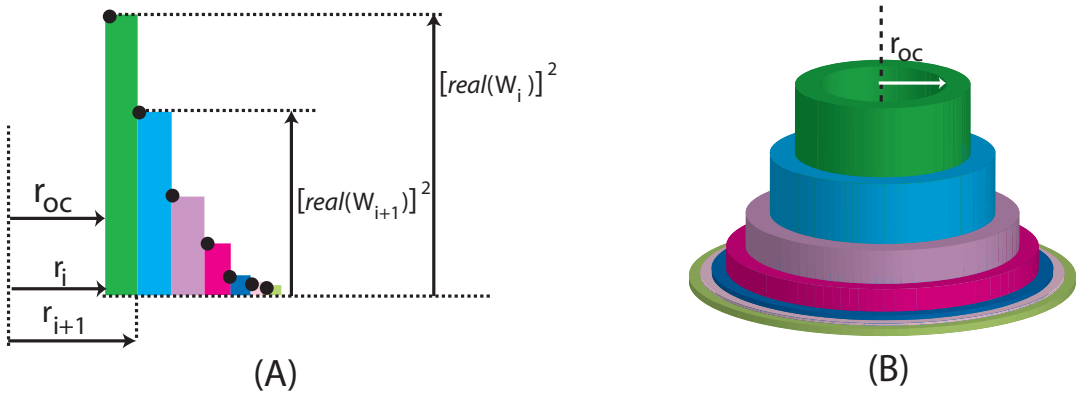

Figure 4.18: The integral $\int_0^{2\pi} \int_{r_c}^{r_{max}} u_{cf}^2 \, r \, dr \, d\theta$ can be solved numerically using cylindrical shells.

velocity must be integrated over the control volume surface $\partial\Omega_1$:

$$F_{cf}(t) = \rho \int_0^{2\pi} \int_{r_{oc}}^{\infty} u_{cf}^2 \, r \, dr \, d\theta$$

As shown in Section 4.4, u_{cf} scales with q (the sink strength), where $q = 2d_o u_{or}$. If the coflow velocity, u_{cf}, is know for some value of q, $q = k$, this is written as $u_{cf:(q=k)}$. The coflow velocity can then be scaled for any desired value $q = d$:

$$u_{cf(q=d)} = q_s \, u_{cf:(q=k)}, \tag{4.32}$$

where $q_s = \frac{d}{k}$. Note that q_s is a dimensionless value.[3]

Given a set of points lying along the line $a = 0$ in the C plane, let n equal the number of points for which $(r - r_{oc}) \leq r_{max}$, where r_{max} is the outer limit of

[3]For example, if $u_{cf:(q=1m^2/s)}$ is known and $u_{cf:(q=5m^2/s)}$is desired, $q_s = \frac{d}{k} = 5$; thus $u_{cf:(q=5m^2/s)} = 5u_{cf:(q=1m^2/s)}$.

integration, and $q = 1\frac{m^2}{s}$. A new function $\chi(r_{oc})$ can be defined as

$$\begin{aligned} \chi(r_{oc}) &= \int_0^{2\pi} \int_{r_c}^{r_{max}} u_{cf:(q=k)}^2 \, r \, dr \, d\theta & (4.33) \\ &\cong \sum_{i=2}^{n} \pi(r_i^2 - r_{i-1}^2)[u_{cf:(q=k)}^2]_{i-1}, & (4.34) \end{aligned}$$

where χ represents the integration illustrated in Figure 4.18. This equation can now be combined with Equation 4.31:

$$\begin{aligned} F_{cf} &= q_s^2 \rho \chi & (4.35) \\ &= \left(\frac{d}{k}\right)^2 \rho \chi \\ &= (2\, d_o\, u_{or})^2 \, (k)^{-2} \rho \chi \\ &= (4\, r_o\, u_{or})^2 \, k^{-2} \rho \chi \\ &= 16\, r_o^2\, u_o^2\, k^{-2} \rho \chi \end{aligned}$$

4.5 Synthetic Jet Force Model

Combining the inflow, outflow, and coflow equations presented in the preceding section allows for the expansion of Equation 4.8:

$$\int_{t_1}^{t_3} F_{total}(\tau)\, d\tau = -\underbrace{\int_{t_1}^{t_2} F_{in}(\tau)\, d\tau}_{\textbf{Inflow}} + \underbrace{\int_{t_2}^{t_3} F_{out}(\tau)\, d\tau}_{\textbf{Outflow}} + \underbrace{\int_{t_1}^{t_3} F_{cf}(\tau)\, d\tau}_{\textbf{Coflow}}.$$

If it is assumed that there are no external forces acting on the jet and that the self-induced coflow is only present during the inflow,[4] the impulse, I_{SJ}, for a synthetic jet with a circular orifice becomes

$$
\begin{aligned}
I_{SJ} &= \int_{t_1}^{t_3} F_{total}(\tau)\, d\tau && (4.36)\\
&= -\int_{t_1}^{t_2} F_{in}(\tau)\, d\tau + \int_{t_2}^{t_3} F_{out}(\tau)\, d\tau + \int_{t_1}^{t_3} F_{cf}(\tau)\, d\tau && (4.37)\\
&= \underbrace{\eta\, \rho\pi r_o^2 \int_{t_1}^{t_2} u_o^2(\tau)\, d\tau}_{\textbf{Inflow}} + \underbrace{\rho\pi r_o^2 \int_{t_2}^{t_3} u_o^2(\tau)\, d\tau}_{\textbf{Outflow}}\\
&\quad + \underbrace{\rho q_s(t) \int_{t_1}^{t_2} \int_0^{2\pi} \int_{r_{oc}}^{\infty} u_{cf}^2(r,\tau) r\, dr\, d\theta\, d\tau}_{\textbf{Coflow}},
\end{aligned}
$$

where the period of a single in-out cycle is $T = (t_3 - t_1)$. The instroke occurs during $t_1 < t < t_2$ and the outstroke during $t_2 < t < t_3$. This generic equation allows for the substitution of any model for u_{cf}, u_{or}, and η. In the next section I will present assumptions that allow this equation to be solved for our proposed jet geometry.

4.6 Model for a Sawtooth Forcing Profile

Equation 4.37 is a generic equation for a synthetic jet's impulse. F_{in}, F_{out}, and F_{cf} are all dependent on the geometry of the synthetic jet (see Figure 4.6). In this next section, each of these terms will be solved for explicitly using jet geometry parameters. As discussed previously, the assumption $\int_{t_2}^{t_3} u_{cf}^2(\tau)\, d\tau = 0$ is made.

[4]The preliminary DPIV data presented in Chapter 3 suggests that while there is coflow induced during the outflow, it is of a smaller magnitude than during the inflow. Additionally, a strong argument can be made for the presence of coflow during the inflow using a potential flow model. It is harder to use such an argument during the outflow. Thus, this model will assume the $F_{coflow} \approx 0$ during the outflow. Our data suggests that this will result in an under-prediction of total force.

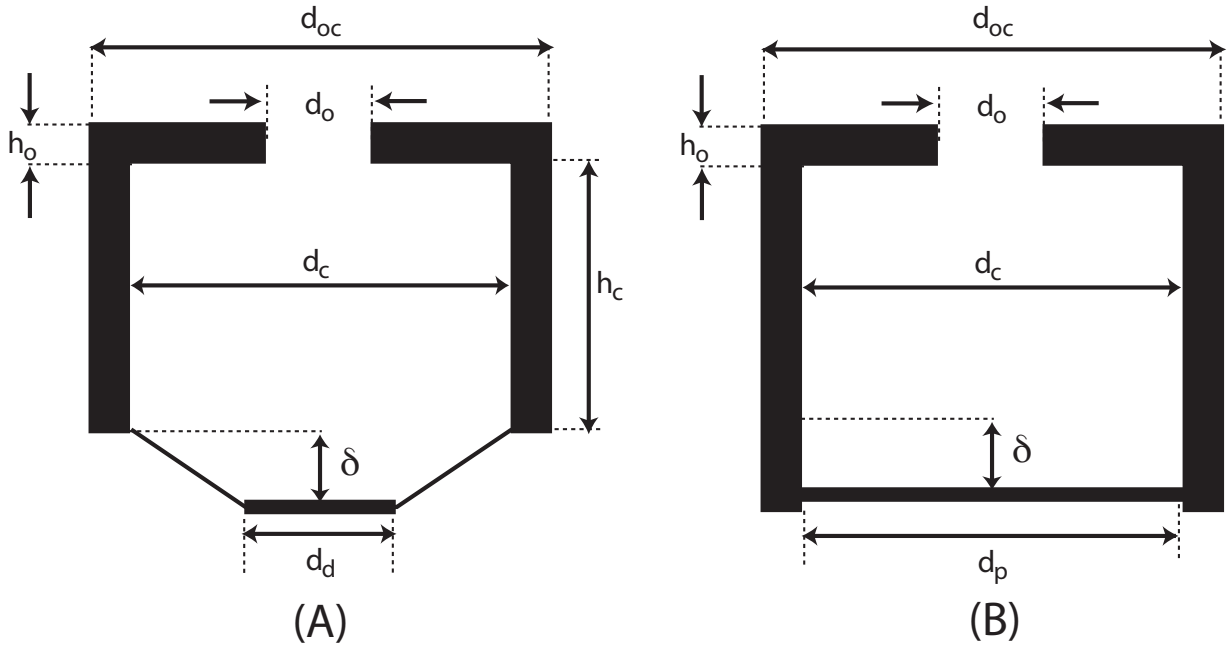

Figure 4.19: Jet geometry for a membrane-with-disk configuration (A) and for a piston configuration (B). Section 4.6 assumes that configuration (B) is used.

All three components are dependent on the variable u_{or}, the velocity of fluid moving through the orifice. This velocity is determined by the area of the orifice and the volume, V, of the fluid that exits the orifice during the outstroke of the membrane:

$$V = \frac{\pi\delta}{3}(r_d^2 + r_c^2 + r_c r_d). \tag{4.38}$$

For a piston, $r_d = r_c$, which simplifies V to $V = \delta\pi r_c^2$. *This is the case that will be considered in this section.*

To satisfy the conservation of mass, the amount of fluid pushed by the piston must be equal to the amount of fluid that exits the orifice.

$$\rho\pi r_o^2 u_{or}(t) = \rho\pi r_c^2 u_p(t) \tag{4.39}$$

$$r_o^2 u_{or}(t) = r_c^2 u_p(t) \tag{4.40}$$

$$u_{or}(t) = u_p(t)\left(\frac{r_c}{r_o}\right)^2 \tag{4.41}$$

This equation for $u_{or}(t)$ can now be used to solve for $F_{in}(t)$ and $F_{out}(t)$ in terms of jet geometry and $u_p(t)$, which is the velocity of the piston.

$$\begin{aligned} F_{out}(t) &= \rho\pi r_o^2 u_o^2(t) \\ &= \rho\pi r_o^2\left[u_p(t)\left(\frac{r_c}{r_o}\right)^2\right]^2 \\ &= \rho\pi u_p^2(t)\frac{r_c^4}{r_o^2} \end{aligned} \tag{4.42}$$

Using the relation $\eta = \frac{\sqrt{2}}{2}$ from Section 3.2,

$$\begin{aligned} F_{in}(t) &= -\eta\rho\pi r_o^2 u_o^2(t) \\ &= -\frac{\sqrt{2}}{2}\,\rho\pi r_o^2\left[u_p(t)\left(\frac{r_c}{r_o}\right)^2\right]^2 \\ &= -\frac{\sqrt{2}}{2}\rho\,\pi u_p^2(t)\frac{r_c^4}{r_o^2}. \end{aligned} \tag{4.43}$$

If a sawtooth piston velocity profile (as was used in the experiments presented in Chapter 5) is assumed, piston velocity can be written in terms of δ, f, and vp.

$$T = \frac{1}{f} \tag{4.44}$$

$$\begin{aligned} t_{in} &= vp \times T \\ &= \frac{vp}{f} \end{aligned} \tag{4.45}$$

$$\begin{aligned} t_{out} &= (1 - vp) \times T \\ &= \frac{1 - vp}{f}, \end{aligned} \tag{4.46}$$

where T is the period of piston actuation (duration of a complete in-out cycle), t_{in} is the amount of time required for the piston to pull in, and t_{out} is the amount of time required for the piston to push out. All quantities are measure in seconds. As before, $0 < vp < 1$.

Instroke ($t_1 < t < t_2$):

$$u_{p:in} = \frac{\delta}{t_{in}} \tag{4.47}$$

$$= \frac{\delta f}{vp}.$$

Outstroke ($t_2 < t < t_3$):

$$\begin{aligned} u_{p:out} &= \frac{\delta}{t_{out}} \\ &= \frac{\delta f}{1 - vp}. \end{aligned} \tag{4.48}$$

Using these equations for u_{or}, F_{in} and F_{out} can be written explicitly in terms of jet geometry and forcing parameters, and thus $\int_{t_1}^{t_2} F_{in}\, dt$ and $\int_{t_2}^{t^2} F_{out}\, dt$ can also be solved for explicitly.

For a sawtooth forcing profile,

$$\begin{aligned} F_{in} &= \eta\rho\,\pi r_o^2 u_o^2 \\ &= \frac{\sqrt{2}}{2}\,\rho\pi r_o^2 \left(u_p \frac{r_c^2}{r_o^2}\right)^2 \\ &= \frac{\sqrt{2}}{2}\,\rho\pi u_p^2 \frac{r_c^4}{r_o^2} \\ &= \frac{\sqrt{2}}{2}\,\rho\pi \left(\frac{\delta f}{vp}\right)^2 \left(\frac{r_c^2}{r_o}\right)^2 \\ &= \frac{\sqrt{2}}{2}\rho\pi \frac{\delta^2\, f^2\, r_c^4}{vp^2\, r_o^2} \end{aligned} \tag{4.49}$$

$$\begin{aligned} F_{out} &= \rho\,\pi r_o^2 u_o^2 \\ &= \rho\pi r_o^2 (u_p \frac{r_c^2}{r_o^2})^{\,2} \\ &= \rho\pi u_p^2 \frac{r_c^4}{r_o^2} \end{aligned} \tag{4.50}$$

$$
\begin{aligned}
&= \rho\pi \left[\frac{\delta f}{(1-vp)}\right]^2 \left(\frac{r_c^2}{r_o}\right)^2 \\
&= \rho\pi \frac{\delta^2 f^2 r_c^4}{(1-vp)^2 r_o^2}
\end{aligned}
$$

Therefore, for a single in-out cycle, the impulses generated are:

$$
\begin{aligned}
I_{in} &= \int_{t_1}^{t_2} F_{in}(\tau)\, d\tau && (4.51)\\
&= \int_{t_1}^{t_2} -\eta\rho\,\pi r_o^2 u_o^2(t)\, dt \\
&= \frac{\sqrt{2}}{2}\,\rho\,\pi\, r_o^2 \int_{t_1}^{t_2} u_o^2(\tau)\, d\tau \\
&= \frac{\sqrt{2}}{2}\,\rho\,\pi r_o^2\,(t_2-t_1)\left(u_p \frac{r_c^2}{r_o^2}\right)^2 \\
&= \frac{\sqrt{2}}{2}\,\rho\,\pi\,\frac{vp}{f}\,u_p^2\,\frac{r_c^4}{r_o^2} \\
&= \frac{\sqrt{2}}{2}\,\rho\,\pi\,\frac{vp}{f}\,[\frac{\delta f}{vp}]^2\,[\frac{r_c^2}{r_o}]^2 \\
&= \frac{\sqrt{2}}{2}\,\rho\,\pi\,\frac{\delta^2 f}{vp}(\frac{r_c^2}{r_o})^2
\end{aligned}
$$

$$
\begin{aligned}
I_{out} &= \int_{t_2}^{t_3} F_{out}(\tau)\, d\tau && (4.52)\\
&= \int_{t_2}^{t_3} \rho\,\pi\, r_o^2 u_o^2(\tau)\, d\tau && (4.53)\\
&= \rho\,\pi\, r_o^2 \int_{t_2}^{t_3} u_o^2(\tau)\, d\tau \\
&= \rho\,\pi\, r_o^2\,(t_3-t_2)\left(u_p \frac{r_c^2}{r_o^2}\right)^2 \\
&= \rho\,\pi\,\frac{(1-vp)}{f}\,u_p^2\,\frac{r_c^4}{r_o^2} \\
&= \rho\,\pi\,\frac{(1-vp)}{f}\left[\frac{\delta f}{(1-vp)}\right]^2 \left(\frac{r_c^2}{r_o}\right)^2 \\
&= \rho\,\pi\,\frac{\delta^2 f}{(1-vp)}\left(\frac{r_c^2}{r_o}\right)^2
\end{aligned}
$$

Combining these equations,

$$\begin{aligned} I_{sj} &= \int_{t1}^{t3} F(\tau)\, d\tau \\ &= \underbrace{-\frac{\sqrt{2}}{2}\rho\pi\delta^2 \frac{f}{vp}^2 \left(\frac{r_c^2}{r_o}\right)^2}_{\textbf{Inflow}} + \underbrace{\rho\pi\delta^2 \frac{f}{(1-vp)}\left(\frac{r_c^2}{r_o}\right)^2}_{\textbf{Outflow}} + \underbrace{\int_{t1}^{t3} F_{cf}(\tau) d\tau}_{\textbf{Coflow}} \\ &= \rho\pi\delta^2 f \left(\frac{r_c^2}{r_o}\right)^2 \left[\frac{1}{(1-vp)} - \frac{\sqrt{2}}{2\,vp}\right] + \int_{t1}^{t3} F_{cf}(\tau) d\tau, \end{aligned} \tag{4.54}$$

where I_{sj} is the impulse generated by an entire in-out cycle. Division of I_{sj} by the period, T, results in the average force over a full cycle.

$$\begin{aligned} \bar{F} &= \frac{I_{sj}}{T} \\ &= \frac{1}{T}\left[\rho\pi\delta^2 f \left(\frac{r_c^2}{r_o}\right)^2 \left(\frac{1}{(1-vp)} - \frac{\sqrt{2}}{2\,vp}\right) + \int_{t_1}^{t_3} F_{cf}(\tau)\, d\tau\right] \\ &= f\left[\rho\pi\delta^2 f \left(\frac{r_c^2}{r_o}\right)^2 \left(\frac{1}{(1-vp)} - \frac{\sqrt{2}}{2\,vp}\right) + \int_{t_1}^{t_3} F_{cf}(\tau)\, d\tau\right] \\ &= f\left[\rho\pi\delta^2\, f \left(\frac{r_c^2}{r_o}\right)^2 \left(\frac{2\,vp - \sqrt{(}2)(1-vp)}{2\,vp\,(1-vp)}\right) + \rho \int_{t_1}^{t_3}\int_0^{2\pi}\int_{r_{oc}}^{\infty} u_{cf}^2 r\, dr\, d\theta\, d\tau\right] \end{aligned} \tag{4.55}$$

For configurations in which $u_{cf} = 0$ (where d_{oc} approaches ∞) this equation reduces to

$$\bar{F}_{(u_{cf}=0)} = \rho\pi\delta^2 f^2 \left(\frac{r_c^2}{r_o}\right)^2 \left[\frac{2\,vp - \sqrt{2}(1-vp)}{2\,vp\,(1-vp)}\right]. \tag{4.56}$$

4.7 Geometric and Actuation Profile Force Dependencies

The derivations in the previous sections make it clear that the amount of force produced by a synthetic jet is dependent on both the jet's geometry and the velocity profile with which the membrane is actuated. As a design tool, it is beneficial to have these relationships written explicitly. This section contains relationship tables for both the general case (a synthetic jet with any piston actuation profile, $u_p(t)$) and the specific case of a sawtooth actuation profile.

4.7.1 Force Relationships: General (Table 4.1)

	F_{out}	F_{in}	F_{cf}
$t_1 < t < t_2$	$F_{out}(t) = 0$	$F_{in}(t) = \eta\rho\,\pi\,u_p^2(t)\frac{r_c^4}{r_o^2}$	$F_{cf}(t) = 16\rho\,u_p^2(t)\frac{r_c^4}{r_o^2}\frac{\chi}{k^2}$
$t_2 < t < t_3$	$F_{out}(t) = \rho\,\pi\,u_p^2(t)\frac{r_c^4}{r_o^2}$	$F_{in}(t) = 0$	$F_{cf}(t) \approx 0$
$\Uparrow r_c$	$\uparrow \propto r_c^4$	$\uparrow \propto r_c^4$	$\uparrow \propto r_c^4$
$\Uparrow r_{oc}$	no change	no change	see discussion
$\Uparrow r_o$	$\downarrow \propto r_o^2)$	$\downarrow \propto r_o^2$	$\downarrow \propto r_o^2$
$\Uparrow u_p(t)$	$\uparrow \propto u_p^2(t)$	$\uparrow \propto u_p^2(t)$	$\uparrow \propto u_o^2$

Table 4.1: Effect of changes in synthetic jet geometry and actuation on force.

	F_{out}	F_{in}	F_{cf}	$\bar{F}$
$t_1 < t < t_2$	$F_{out} = 0$	$F_{in} = \frac{\sqrt{2}}{2}\rho\pi\frac{\delta^2 f^2 r_c^4}{vp^2\ r_o^2}$	$F_{cf} = 16\rho\frac{\delta^2\ f^2\ r_c^4}{vp^2\ r_o^2}\frac{\chi}{k^2}$	
$t_2 < t < t_3$	$F_{out} = \rho\pi\frac{\delta^2 f^2 r_c^4}{(1-vp)^2\ r_o^2}$	$F_{in} = 0$	$F_{cf} \approx 0$	
$\Uparrow f$	$\uparrow \propto f^2$	$\uparrow \propto f^2$	$\uparrow \propto f^2$	$\Uparrow$
$\Uparrow r_c$	$\uparrow \propto r_c^4$	$\uparrow \propto r_c^4$	$\uparrow \propto r_c^4$	$\Uparrow$
$\Uparrow r_{oc}$	no change	no change	see discussion	see discussion
$\Uparrow r_o$	$\downarrow \propto r_o^2)$	$\downarrow \propto r_o^2$	$\downarrow \propto r_o^2$	$\Downarrow$
$\Uparrow \delta$	$\uparrow \propto \delta^2$	$\uparrow \propto \delta^2$	$\uparrow \propto \delta^2$	$\Uparrow$
$\Uparrow vp$	$\uparrow \propto (1-vp)^{-2}$	$\downarrow \propto (vp)^{-2}$	$\downarrow \propto (vp)^{-2}$	$\Uparrow$

Table 4.2: Effect of changes in synthetic jet geometry and actuation on force, *assuming a sawtooth forcing profile.*

4.7.2 Force Relationships: Sawtooth Profile (Table 4.2)

4.8 Potential Sources of Error in this Model

There are a few clear reasons for any discrepancies between the model's predictions and experimental results. As each part of the force equations was derived, the following assumptions were mentioned and explained. This section reiterates these assumptions and the possible effect they may have on the total force calculations.

4.8.1 Outflow Assumptions

The outflow calculating presented in Equations 4.11 and 4.10 make the same assumption. First, it is assumed that u_{or} is constant across the entire orifice area. We know that this is not the case. While $u_o(\theta)$ is constant, $u_o(r)$ is definitely not. However, as F_{out} is dependent on the integration of u_{or} over the area of the orifice, and conservation of mass must be satisfied, this assumption is reasonable.

The second assumption that is made is that d_o for the outflow is the physical

diameter of the orifice plate. This minimizes the impact that a boundary layer forming along the orifice's walls may have. Given that the orifice plates built and modeled for this thesis are relatively small compared to the jet's other dimensions, this seems to be a fair assumption. However, Shusser et al. [36] have calculated the effect that boundary layer growth has on the formation of vortex rings generated using a traditional piston/cylinder arrangement. For thick orifice plates, their findings can be applied to the F_{out} formulations.

4.8.2 Inflow Assumptions

The value of η, the average angle of inflow, effects the value of $\bar{F}$. The value $\eta = \frac{\sqrt{2}}{2}$ was calculated assuming that the inflow vectors are the same as they would be if the inflow was a perfect sink. While this is consistent with the rest of the model presented in this thesis, this is clearly an approximation.

4.8.3 Coflow Assumptions

Self-induced coflow in synthetic jets has not been discussed prior to this thesis. Thus, much work is needed to gain a thorough understanding of this phenomenon and its contribution to net thrust. The magnitude of the coflow velocity, using the sink model presented in Section 4.4, is based on the distance from the sink to the outside wall of the fluid chamber. The model in its current configuration places the sink in the center of the orifice (as illustrated in Figure 4.3B). The strength of the sink is based on u_{or} and d_o, yet the distance from the sink's center to the outer chamber wall, r_{oc},

is constant regardless of d_o. For the reasons discussed in Section 4.3, it is likely that a "split sink," as picture in Figure 4.3C, is a more accurate depiction of the inflow. This would mean that r_{oc} would actually decrease as d_{oc} increases. This would increase the velocity of the coflow and, by extension, F_{cf}. As more flow visualization is needed to verify the validity of this claim, the more conservative coflow velocity model is used.

It must also be reiterated that the current coflow model is created using potential flow. As a potential flow model assumes an irrotational, inviscid fluid, the velocities calculated using it must be taken only as a rough estimate. Finally, the assumption that $\int_{t_2}^{t_3} F_{cf}(\tau)\, d\tau = 0$ is made. This means that there is no coflow force generated during outflow. This assumption is made based on the flow visualization result shown in Figure 3.6.

4.9 Notes on Parameter Coupling

Realistically, not all of the parameters in the above equations can be uncoupled. Clearly, for a fixed piston throw, δ, increasing the chamber radius, r_c, will increase the volume flux through the orifice and thus the amount of thrust produced. However, this also increases the amount of force that the piston must exert on the fluid. For membrane actuation techniques that do not have a mechanically enforced throw distance (ie., voice coil, solenoid, etc.), the increase in required force will typically decrease the the throw. A solution to this problem is to mechanically enforce the throw distance (using a scotch yoke, cam, or other method). This approach is also not without its tradeoffs, as the increased force will require an increase in input energy.

4.10 Modeling Conclusions

This chapter presented a new model for synthetic jet force production. It was proposed that there are three force-producing elements to synthetic jet flow: inflow at the orifice, outflow at the orifice, and a self-induced coflow. A derivation was presented for the asymmetry of the orifice inflow term. The proposed inflow model explains the occurrence of a measured net thrust despite the use of symmetric membrane actuation profile.

A potential flow, conformal mapping approach was presented for the self-induced coflow velocities. From this, a coflow thrust model was derived. While the contribution from the self-induced coflow is relatively small, it raises the possibility that careful design of the thruster housing (or robot) shape can augment this term and add additional thrust.[5]

[5]In a power-limited application such as autonomous underwater vehicle operations, even small improvement in efficiency can have substantial impact on mission duration.

Chapter 5

Experimental Thrust Measurement

When this project was begun, no data on synthetic jet thrust was available. Mohseni [48] reported having used synthetic jets to spin a submerged cylinder, but no data or video was presented. Thus, no quantified proof that synthetic jets produce a net thrust was available. Additionally, the model presented by Müller [50] proposes that, in the absence of a free stream flow, no thrust is generated during the instroke. As the model presented in Chapter 4 asserts that a net thrust is produced and thrust is produced during the instroke, experimental verification was necessary.

5.1 Force Measurement Setup

For synthetic jets to prove useful as a propulsion method, it must be shown that an appreciable amount of force is produced. A simple device was constructed to measure the produced thrust from several of the prototypes described in Chapter 2. A force sensor (an Interface Advanced Force Measurement Part WMC-5 strain gauge[1]) was

[1]It should be noted that we used three different force sensors over the course of this project. The first was a Kistler 9212 load cell. We found the drift on this sensor to be rather high, and thus used it only for the automated optimization experiments discussed in Section 5.5 Experiments using the Kistler sensor will be noted as such. All other experiments were conducted using Interface Force load cells.

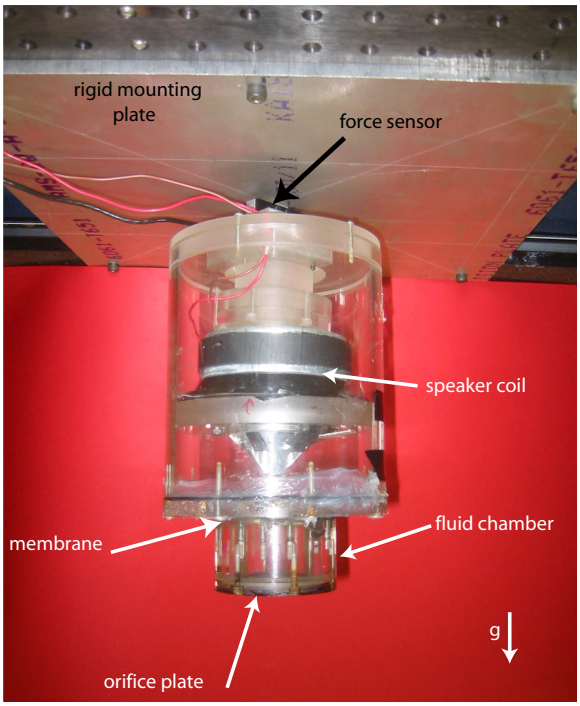

Figure 5.1: Force measurement setup.

mounted between the back of the jet prototypes and a metal mounting plate, as shown in Figure 5.1. The setup was then submerged (as shown in Figure 5.2). The jet was only submerged part way, so that the drag could be ignored (as opposed to covering the entire jet and thus needing to consider the added mass and drag produced by the flat circular back of the jet.) The average thrust was measured by taking the average of at least 5 seconds of data (at a sampling rate of 8 kHz). To account for any possible sensor drift, the sensor's zero force level was calibrated before each set of trials.

5.2 Voice Coil Results

For the experiments described in this section, $d_c = 3.81$ cm, $d_d = 2.85$ cm, $d_o = 0.95$ cm, as labeled in Figure 5.3. The maximum throw of the disk, δ, is approximately

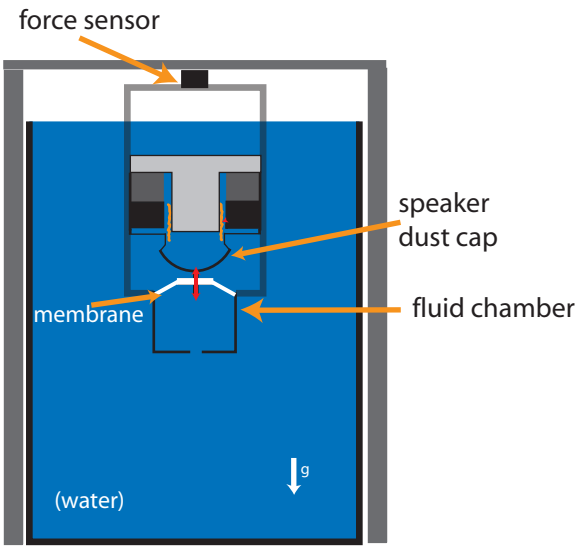

Figure 5.2: Illustration of force measurement setup with jet submerged.

3 mm. The throw was measured by inspection using a high speed camera. The membrane throw changes with frequency and velocity profile. Measuring the throw by looking at video images, over the range of 1-7 Hz (for velocity profiles .2, .5, and .8), the throw varied from 2-4 mm (while the jet is submerged). No clear relationship between throw and frequency is evident over this range, though typically a speaker's throw will decrease with increased frequency. Given that the exact throw of the membrane is unknown, it is difficult to compare the resulting forces with the model predictions (as the model is dependent on membrane throw.)

5.2.1 Relationship Between Forcing Frequency and Thrust

This thesis will focus on the forces produced for membrane oscillation frequencies of 10 Hertz or less. This decision was made for a variety of reasons. First, lower frequencies are less likely to cause resonance effects on our particular apparatus. The

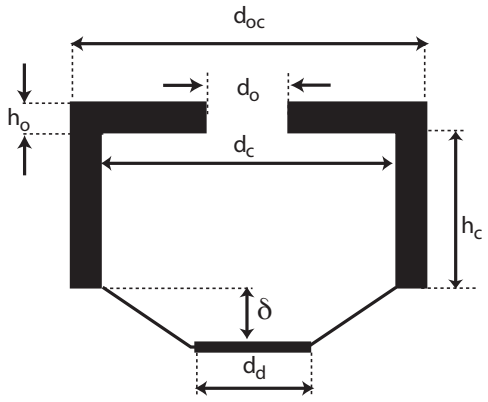

Figure 5.3: Speaker driven synthetic jet parameters.

exact frequency at which this transition occurs is likely dependent on the geometry of the jet, as the various natural resonances (membrane, chamber, mounting platform, etc.) are dependent on geometry and construction. Second, the higher the frequency the greater the amount of power that is needed. As we are trying to test the feasibility of using synthetic jets for slow moving vehicles it makes more sense to focus on lower frequencies. Third, sea creatures using pulsatile jet propulsion tend to do so at low frequencies. Thus, I hypothesize that synthetic jets operating at low frequencies are less likely to bother sea life.

As the jet is hanging from the force sensor there will be a force measurement offset even before turning the jet on. This is shown in Figure 5.4A. The average "jet off" sensor reading must be subtracted from the average reading taken with the jet on in order to get an accurate reading of the force contribution due to the jet's thrust. Figure 5.4B shows a typical force sensor reading for a running jet. (In this particular plot the jet actuation frequency is 5 Hz.) It is clear that the jet contributes a force throughout its entire cycle, and that during the instroke the sign of the force

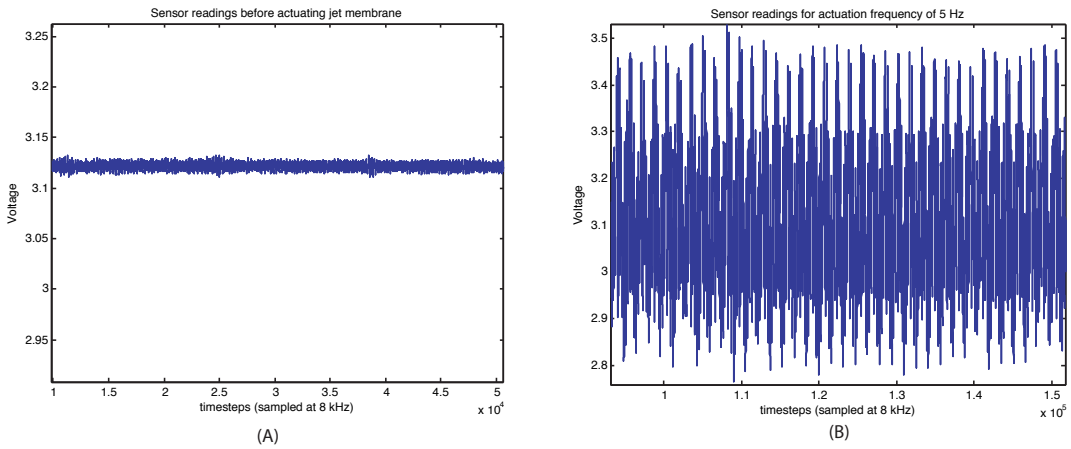

Figure 5.4: (A) shows a sensor reading before actuating the jet's membrane; (B) shows the sensor reading while actuating the membrane at 5 Hz.

is opposite that of the force produced during the outstroke. This is consistent with Chapter 4's model which predicts thrust production during both the instroke and outstroke.

Figure 5.5 shows the effect of frequency on measured average force for the speaker driven jet Note that for this experiments the programmed membrane velocity profile was symmetric (i.e. the membrane instroke velocity is the same as the outstroke velocity). It is clear that the average thrust increases with increased membrane actuation frequency.

Currently, in the synthetic jet literature, only membrane forcing profiles which are symmetric in their instroke and outstroke velocity profiles are considered. As the model presented in Chapter 4 shows, changing the relative inflow and outflow rates is likely to have an impact on the net thrust. This chapter presents a preliminary study into the effects of modifying this variable. Perhaps the simplest way of doing this is to specify the membrane's displacement as a sawtooth function. As shown in Figure

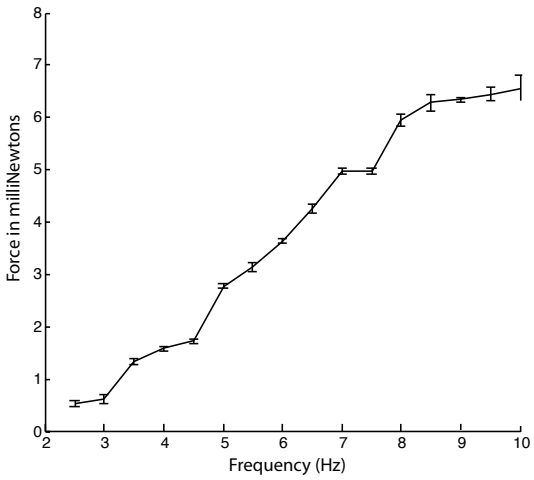

Figure 5.5: Force as a function of frequency

5.6, by changing the point in a cycle at which the switch from inflow to outflow occurs will allow for the ratio of inflow to outflow velocities to be altered.

As this experiment is performed using the apparatus illustrated in Figure 2.6, it can not be assumed that the signal sent from the computer, as shown in Figure 5.7A, is an accurate representation of the membrane displacement. Figure 5.7B shows a reading taken at the speaker's leads. Note that the increase in amplitude is intentional, due to the use of the audio amplifier. Clearly the signal read at the speaker leads is not a perfect triangle. There are a few possible causes for this. First, the noise and clipping that occur at the sawtooth peaks in Figure 5.7B may be due to an impedence mismatch between the speaker and the card being used to read the signal. Thus it is possible that that particular effect may simply be a measurement artifact. The curvature of the instroke and outstroke signal line may have many possible causes. Moving the speaker cone (even without a power source) will generate

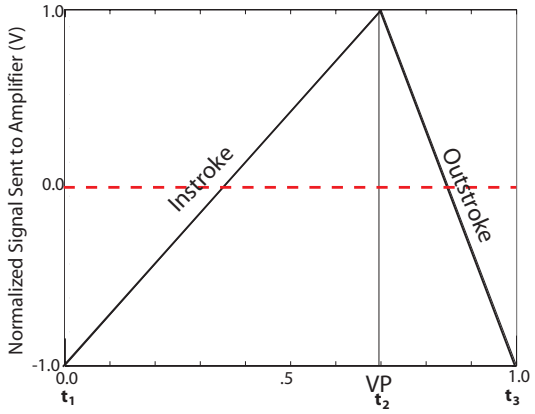

Figure 5.6: Parametrization for the signal sent to the speaker, showing programmed signal as a function of time for a single period of duration T. The vertical line marks the point l_p, where the velocity attains its maximum amplitude A.

a signal since the process of moving the magnet through the wire coil will generate current. Thus, it is reasonable to assume that if the voltage is increasing the speaker cone (and thus the jet membrane) is also moving outwards. Similarly, a decreasing voltage would signify an inward movement. The exact membrane position can not, however, be extrapolated from this voltage. Therefore, for the purpose of this chapter I will use the phrase *programmed velocity profile* to refer to the signal sent from the computer to the amplifier.

5.2.2 Relationship Between Programmed Velocity Profile and Thrust

Figure 5.8 shows the average thrust for five different *programmed* velocity profiles (0.2, 0.4, 0.5, 0.6, and 0.8) in the 1–10 Hz region. A direct correlation between programmed velocity profile and measured thrust can be seen. The measured thrust

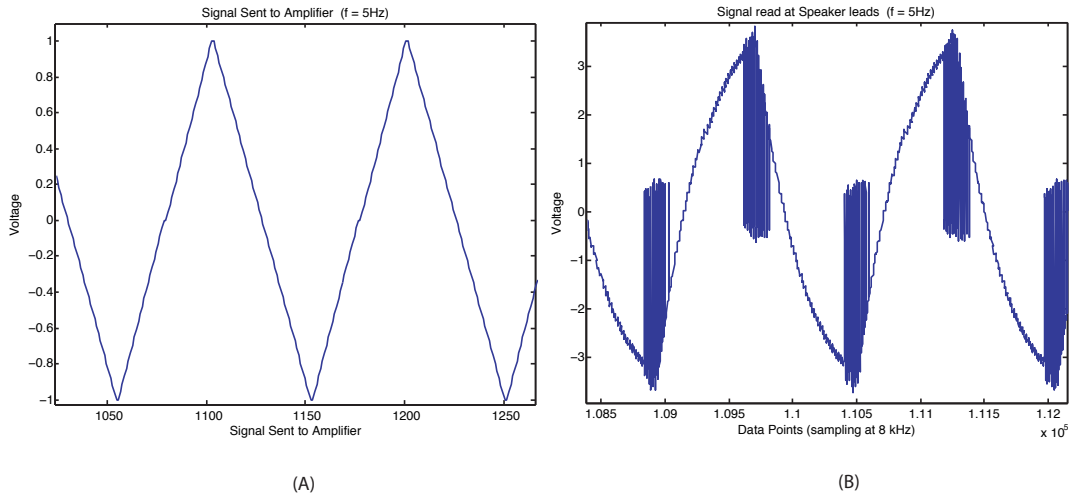

Figure 5.7: (A) shows the signal sent from the computer to the signal amplifier; (B) shows the voltage read at the speakers leads.

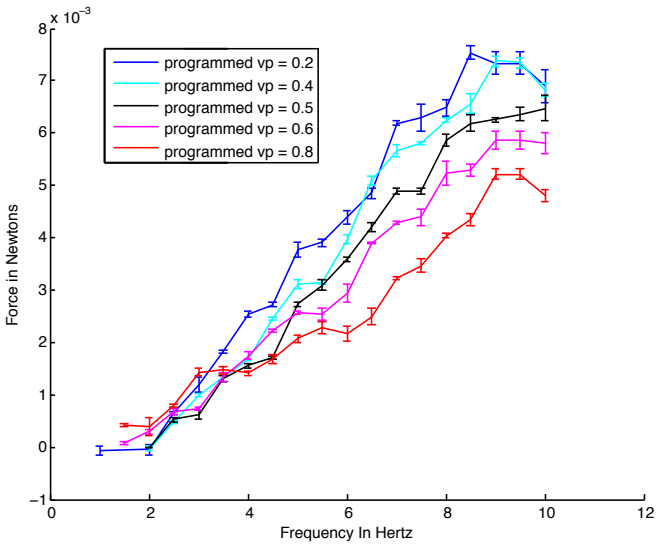

Figure 5.8: Average force as a function of frequency and velocity profile.

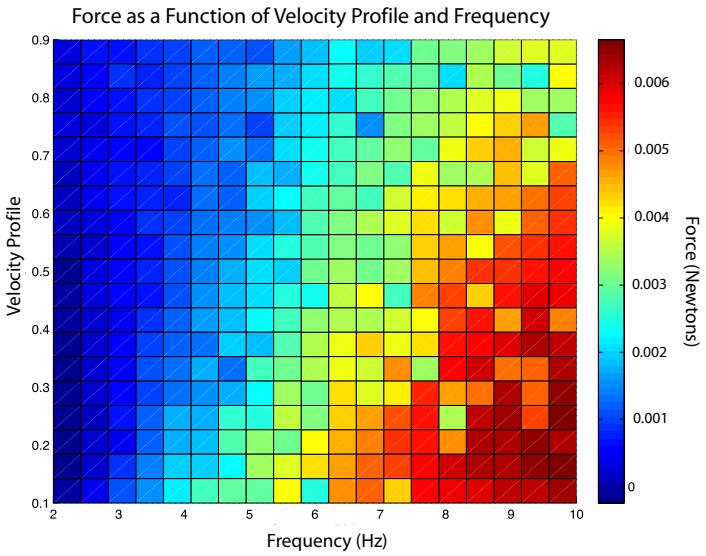

Figure 5.9: Force as a function of frequency and velocity profile

increases as the velocity profile index decreases. This correlates to a lower outflow velocity than inflow velocity, but to a longer time spent ejecting fluid. It should be noted that the points shown in this plot were taken randomly out of order so as to rule out any sensor drift as a possible explanation for such a trend. Each point on this plot is the average of 5 trials, with the error bars representing a standard deviation. This result was confirmed by an experiment, performed by Dr. Michele Milano, which took, and averaged, five measurements at all combinations of frequencies 2-10 Hz (in increments of 8/19 Hertz) and programmed velocity profile 0.1 - 0.9 (in increments of 0.8/19 using the same equipment as used to produce figure 5.8). The results of these trials are shown in Figure 5.9. Section 5.5 will illustrate that an automated optimization experiment using the laboratory grade voice coil prototype also confirmed the advantage of a programmed velocity profile less than 0.5.

5.3 Additional Verification of Force Measurements

Given that the synthetic jet forces measured above are among the first such measurements ever performed, further verification of the validity of the measurements was desired. For that reason, a second set of experiments (presented below) were performed. For these experiments a 16-bit data acquisition card was used so as to obtain higher resolution in the results (a 12 bit card was used in the previous section). In the interest of performing these experiments in a completely new setup (for verification purposes) a new force sensor, an SML-10 tension/compression load cell from Interface Force. The sensor signal was amplified using an Interface DCA amplifier. The sensor was mounted as shown in Figure 5.1, and the mounting plate was $\frac{1}{4}$ inch aluminum so as to minimize any vibrations. The sensor was calibrated, as shown in Figure 5.11, [2] The jet was taken apart and a new speaker was put in. The membrane throw, δ for this second set of experiment was not formally measured, though spot checks indicate that the throw is less than that of the previous experiment. This is likely due to the fact that the speaker in the previous experiment had been run in hundreds of experiments over the course of two years, and thus the speaker's suspension is more flexible.

This second set of force measurements was taken on the same jet as used in the previous section, however the orifice diameter was changed to $d_o = 0.7$ cm. (The other dimensions stayed unchanged: $d_c = 3.81$ cm, $d_d = 2.85$ cm).

[2] To verify the sensor's reliability in for measuring small forces in the appropriate region of its range, the calibration was done by adding weights *in addition* to the jet.

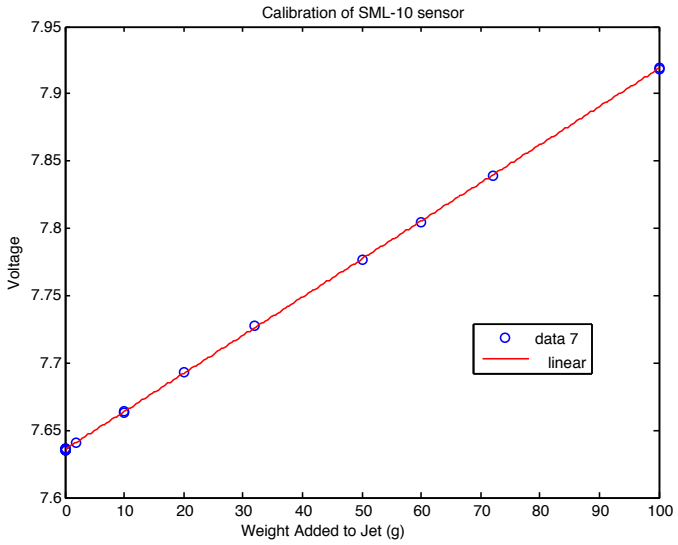

Figure 5.10: Calibration for SML-10 sensor used in Section 5.3.

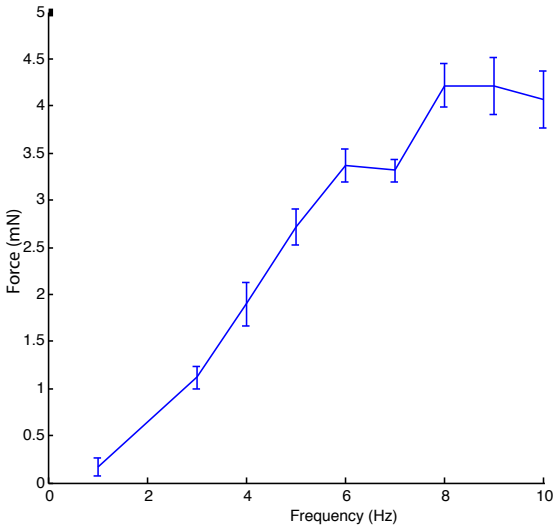

Figure 5.11: Force as a function of frequency. Each point is the average of 10 trials, and the error bar represents ± one standard deviation.

5.4 Force Results for Solenoid Driven Prototype

In Chapter 2 designs for solenoid driven synthetic jets were presented. However, we found that the range of frequencies over which force could be produced using these synthetic jets was suprisingly small. Figure 5.12 shows the steep drop in force as frequency is increased. Krieg, Mohseni, et al. [27] present the results of force measurements performed on solenoid driven synthetic jets. They, too, found that the stroke length of the piston was dramatically reduced when the actuation frequency was increased. In their experiment the throw decreased from ≈ 0.3 inches to ≈ 0.03 inches over the range $0 - 40Hz$.

Given our results, and those of Krieg, it is unlikely that solenoid actuation would be chosen as an actuation method for synthetic jets in configurations where a wide range of frequencies are desired. It is, however, possible that solenoids may be ideal for applications in which the jet is designed to be driven at a particular frequency. The solenoid, and the restoring spring's constant, could be chosen to meet specific design criteria. This would be similar to the use of piezoelectric membrane actuation in air synthetic jets which are tested and designed to be driven at their resonance frequency.

5.5 Automated Optimization of Velocity Profile

The research presented in this section was done in collaboration with Dr. Michele Milano and Maxwell Grazier G'sell. [60]. This thesis was begun with the hope that

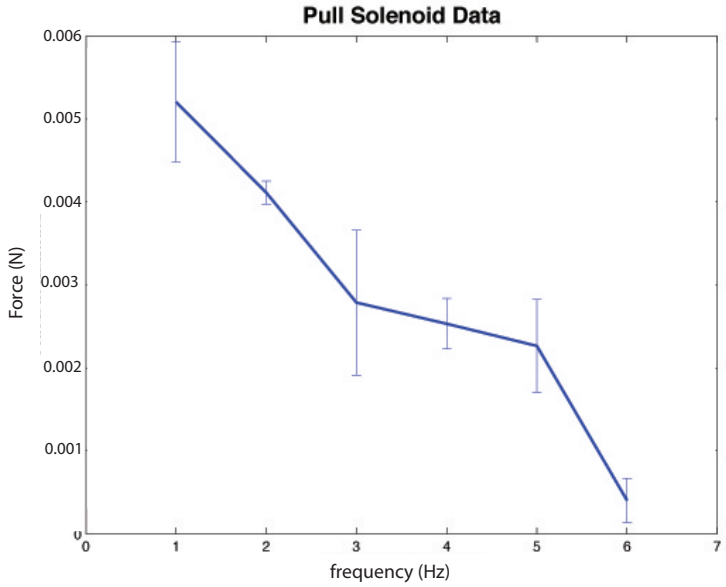

Figure 5.12: Force as a function of frequency for solenoid driven prototype (5 trials were performed for each frequency.

synthetic jets may prove a viable propulsion method for small underwater vehicles. For that to be the case, the jets would need to be produced in larger quantities. As our prototyping in Chater 2 shows, subtle variations in the design such as quality of construction, tightness of the membrane, and variations in response from voice coil to voice coil, which can have significant implications on the efficiency and force output of the jets. For this reason, we sought to create an automated multi-variable optimization technique to find parameter combinations resulting in maximum thrust, as an alternative to the prohibitive task of exhaustively testing all possible parameter combinations.

5.5.1 Genetic Algorithm

The genetic algorithm used in this experiment is a modification of the Controlled Random Search (CRS) method of [77]. For convenience, a brief summary is provided below. A more thorough explanation can be found in Michele Milano's dissertation [78]. The algorithm used for this experiment wass written by Dr. Milano.

Let $G(\lambda)$ be a cost function to be minimized by the choice of design parameters, $\lambda \in R^n$. For this work, G is the inverse of the average thrust produced by the synthetic jet (produced over a 7 second period). In a first phase, a set of S parameters vectors, or "population points," are initially chosen at random according to a uniform distribution within a defined n-dimensional search. The inequality $S \gg n$ must hold for the algorithm to work properly. The algorithm proceeds as follows:

1) Find the parameter λ_{max} from the initial set of S points which maximizes G: $\lambda_{max} = arg\Big[\max_{i=1,...,M} G(\lambda_i)\Big]$; $G_{max} = G(\lambda_{max})$

2) Randomly choose $n+1$ different population points: $\lambda_1, ..., \lambda_{n+1}$ (breeding set). All subsequent operations are performed on this set

3) Mutation step: for all breeding set points, with probability $P_i = (1-\alpha^I) \cdot \left(1 - \beta^{\frac{(G(\lambda_i)-G_T)}{\overline{G}}}\right) \cdot \gamma$, replace the point λ_i with one randomly chosen within the search volume limits

4) Recombination step: for each of the $n+1$ points determine the centroid, $\underline{\lambda_i}$, of the other n points, i.e. $\underline{\lambda_i} = \frac{1}{n}\sum_{j=1}^{n} \lambda_j$

4.a) Generate offspring $\lambda_{si} = 2\underline{\lambda_i} - \lambda_{n+1}$; if λ_{si} is not contained in the search volume, process next point in breeding set

4.b) Calculate $G(\lambda_{si})$: if $G(\lambda_{si}) < G_{max}$ then purge λ_{max} from population, and substitute by offspring λ_{si}

5) Compute the new G_{max}, if necessary

6) Iterate steps 4 and 5 on the whole breeding set

7) If convergence test fails, return to step 1

There are 4 parameters (α, β, γ, and G_T) and two variables(I and $\overline{G}$) that must be chosen by the user in this optimization scheme. The variable I is the number of consecutive iterations in which the population has not changed. It provides an empirical measure of the need for fresh information through increased mutation probability. The variable $\overline{G}$ is the average population fitness, used as a scaling factor. The most important parameter is G_T, a threshold value used for the convergence test: we declare convergence once all of the population's fitness values are below it. With this convergence criterion, population points will be clustered inside the domain defined as: $\{\lambda | G(\lambda) < G_T\}$. According to the formula defining mutation probability, the parameter $0 \leq \alpha \leq 1$ modulates the mutation rate during the optimization process, and the parameter $0 \leq \gamma \leq 1$ enforces its upper bound, since $0 \leq \beta \leq 1$. The term containing the parameter β causes population members far from convergence (with fitness $> G_T$) to mutate more frequently. (CRS can be regarded as a GA with zero mutation probability.)

5.5.2 Experimental Parameters

We used a GA population of 50 elements, with the parameters α and β fixed to 0.25, the upper bound γ to 0.02 and the threshold G_T to 0.1, which is small enough to ensure a sufficient exploration of the search volume. This algorithm yielded a satisfactory result in about 1000 iterations. The number of iterations would be substantially reduced by removing the amplitude parameter, as we found that the maximum allowed voltage amplitude to result in the maximum force. However, leaving this parameter in the optimization provides a more thorough test. It is also possible that for different types of speakers there may be a noticeable membrane throw versus input voltage relationship, and the optimization would catch this. Additionally, any other desired parameters could be added to this optimization as long as the parameters could be physically changed automatically by the system.

It is probable that a jet's performance characteristics will change over time as it ages and mechanical considerations, such as the stretching of the membrane, vary. Thus, it is recommended that an automated optimization process is used in the future testing of synthetic jets.

5.5.3 Optimization Results

We tested this optimization scheme on a synthetic jet prototype using the Brul and Kjael minishaker as an actuator. The optimization was run shortly after constructing the first prototype, and before any other force measurements had been made. Figures 5.13 - 5.19 show the distribution of parameters in the population as the number of

iterations increases.

An alternate way of viewing the results is to plot the mean amplitude (Figure 5.20), velocity profile (Figure 5.21), and frequency (Figure 5.22) as a function of iteration number. As the thrust was maximized, the population's frequency increases. This is unsurprising, as an increased frequency leads to an increased fluid velocity across the orifice. Similarly increasing the signal amplitude, which leads to an increased membrane throw, was also found to increase average produced thrust. The one surprising result of the optimization was the dominance of low velocity profiles in the final population. (Low velocity profile corresponds to a membrane forcing profile in which the outstroke is slower than the instroke.) This is the opposite of what we had been expecting; however it is consistent with the results shown in section 5.2.2.

5.5.4 Future Applications of this Optimization Technique

The automated optimization process was useful for getting an initial sense of the effect of frequency, amplitude and velocity profile on produced thrust. While there appears to be a clear relationship between frequency and force for the frequencies tested, the automated optimization may be useful if it is decided that frequencies well above this range wish to be tested. A potentially more powerful application of this technique would be the testing of more complex velocity profiles. The simplicity of the sawtooth profile, while ideal for this preliminary exploration of synthetic jet thrust, likely limits the amount of force produced by the jet. Krueger's work on the effects of overpressure on the thrust produced by pulsed jets [1, 38] highlights the advantage of maximizing

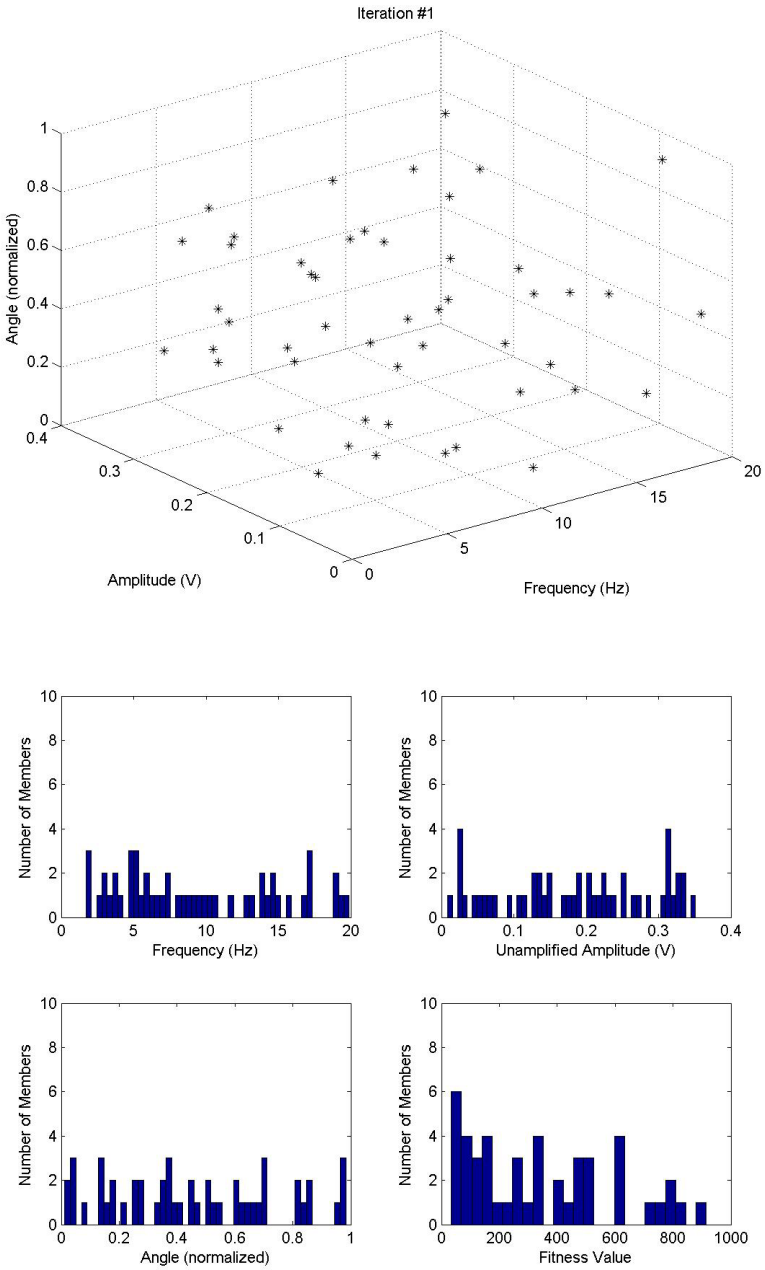

Figure 5.13: Distribution after one iteration

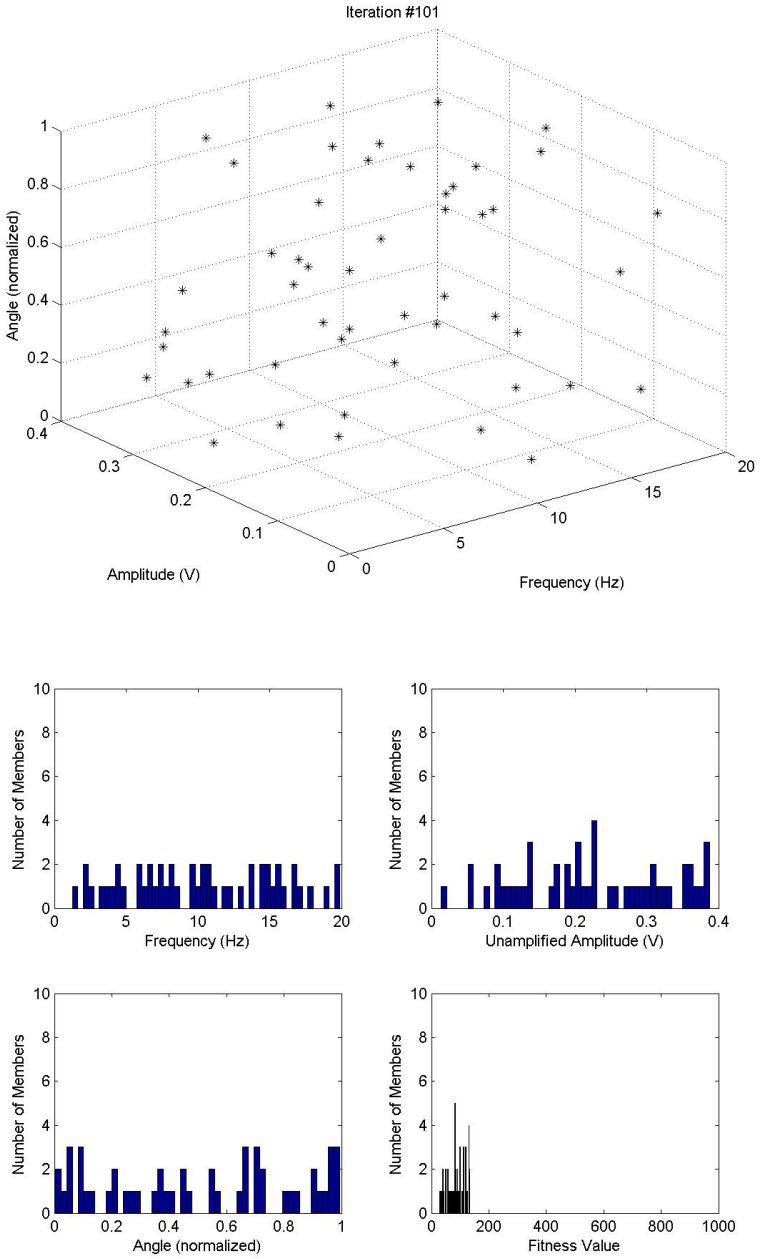

Figure 5.14: Distribution after 101 iterations.

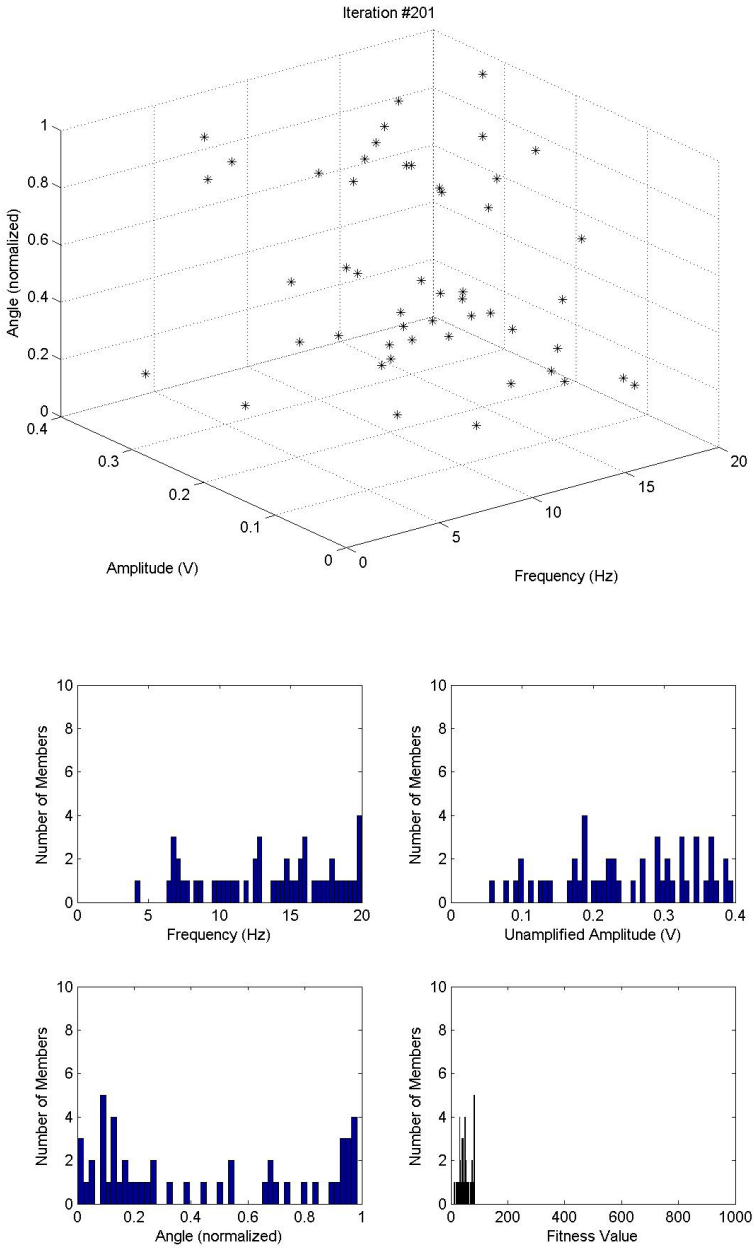

Figure 5.15: Distribution after 201 iterations.

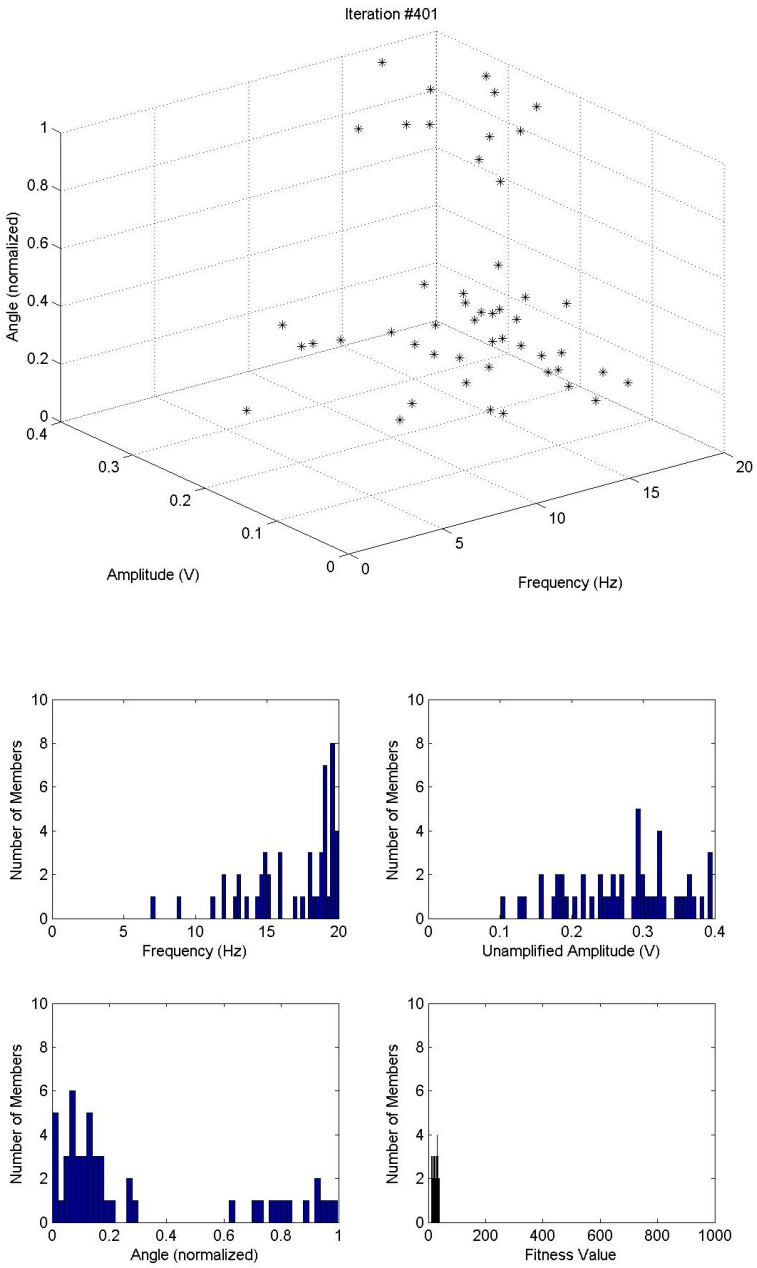

Figure 5.16: Distribution after 401 iterations.

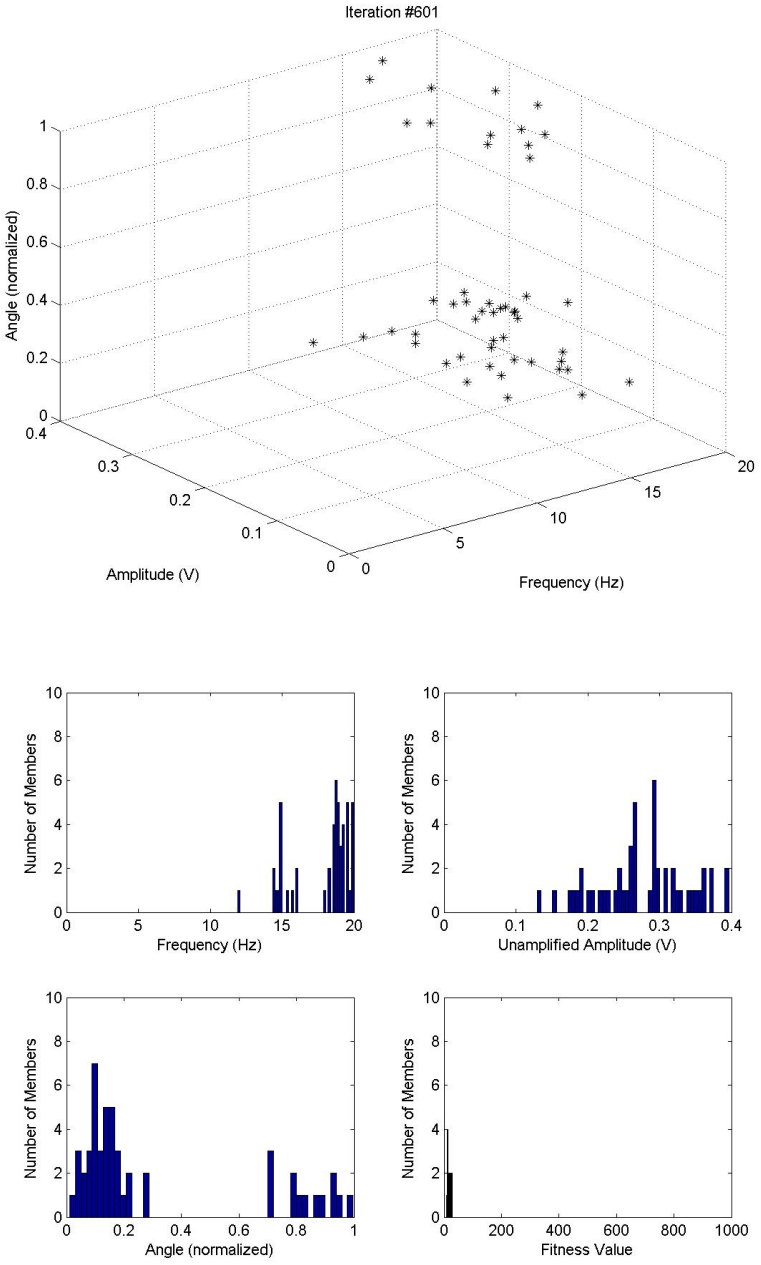

Figure 5.17: Distribution after 601 iterations.

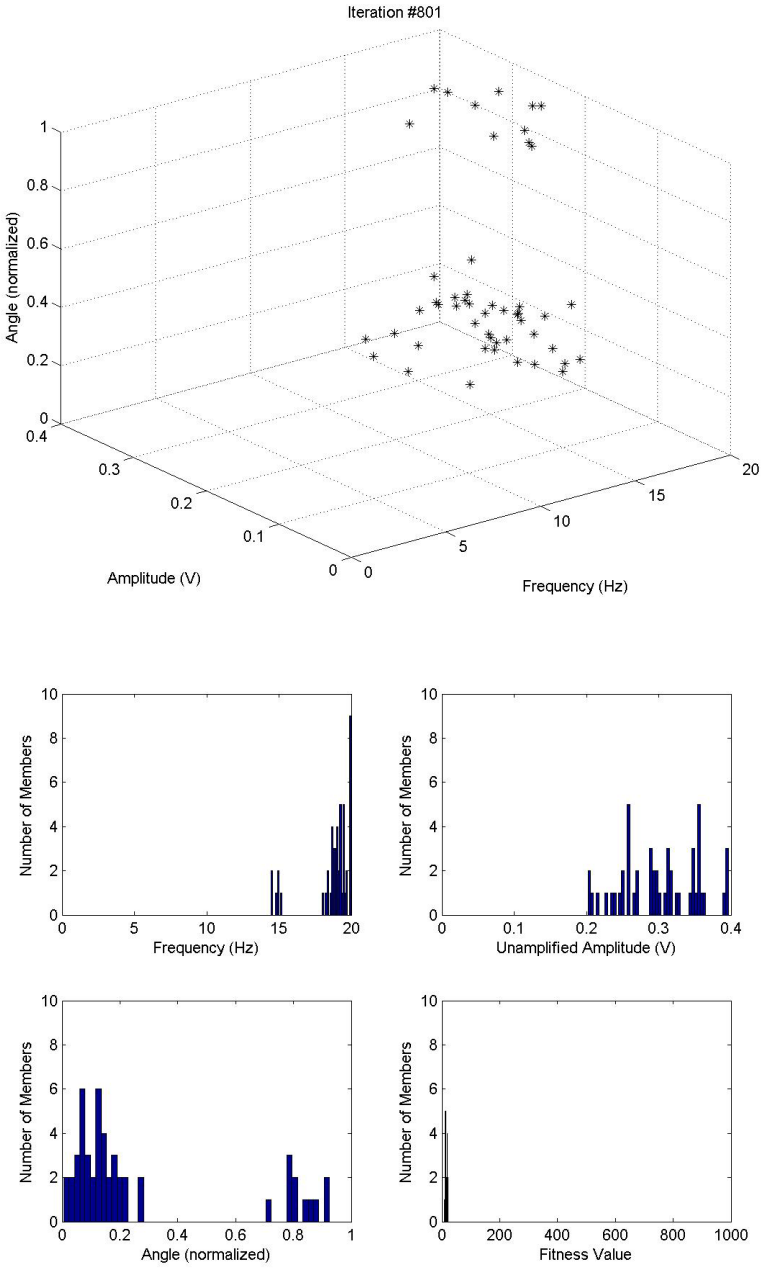

Figure 5.18: Distribution after 801 iterations.

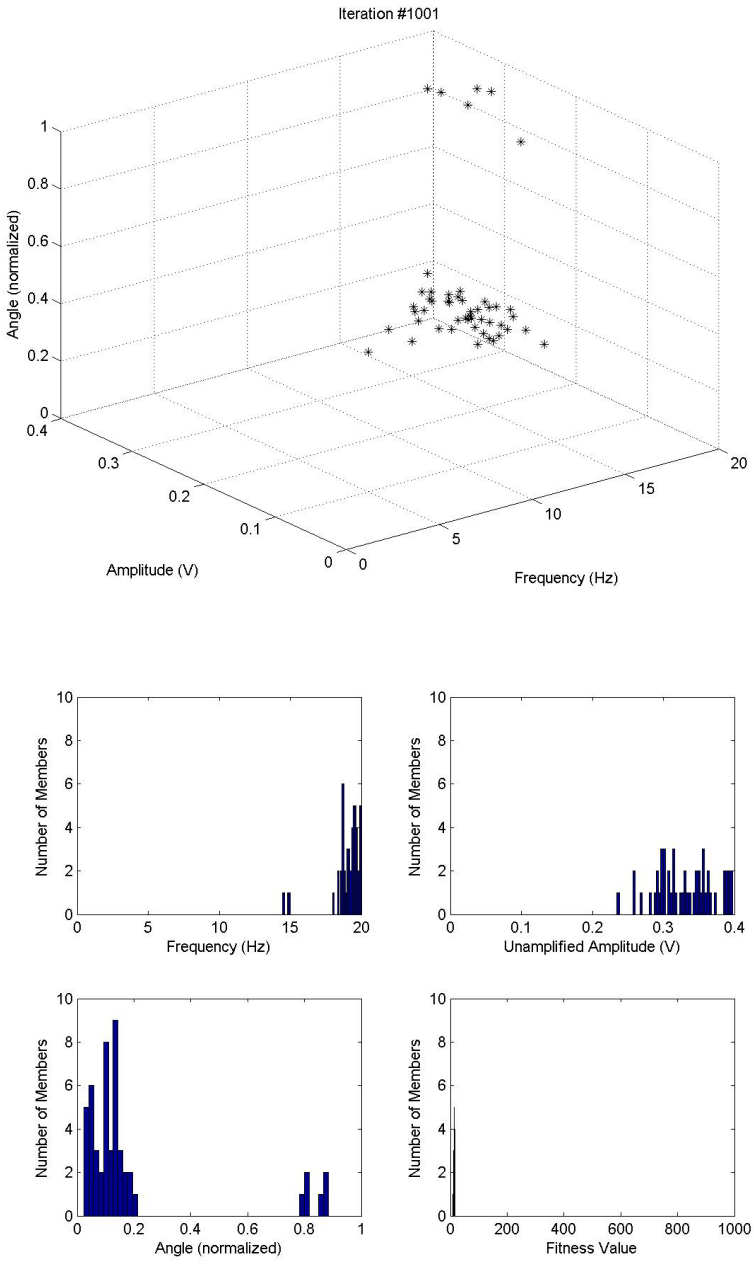

Figure 5.19: Distribution after 1001 iterations.

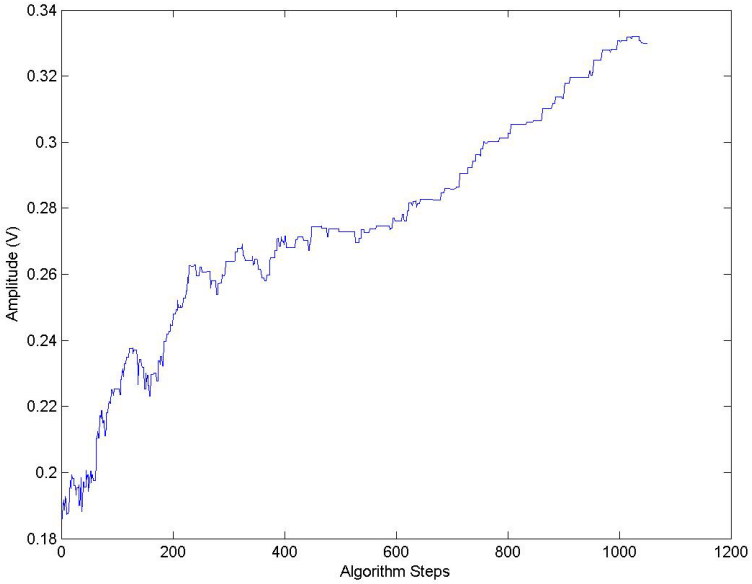

Figure 5.20: Mean population amplitude versus iteration number.

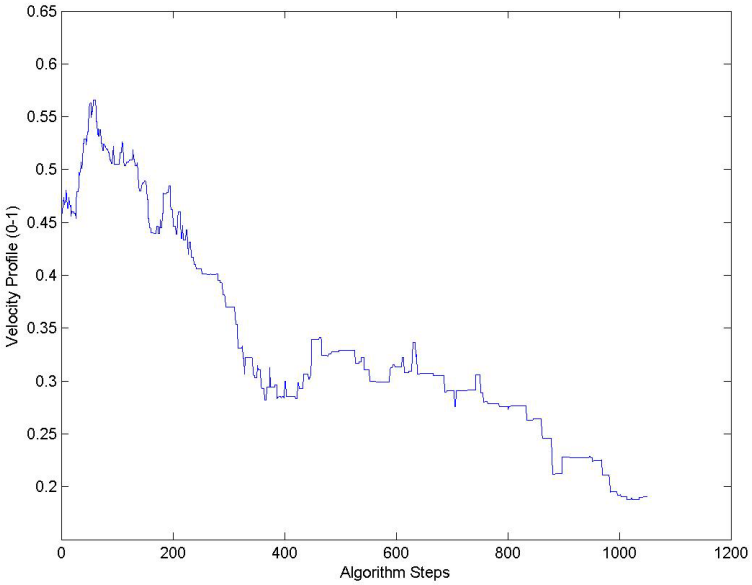

Figure 5.21: Mean population angle versus iteration number.

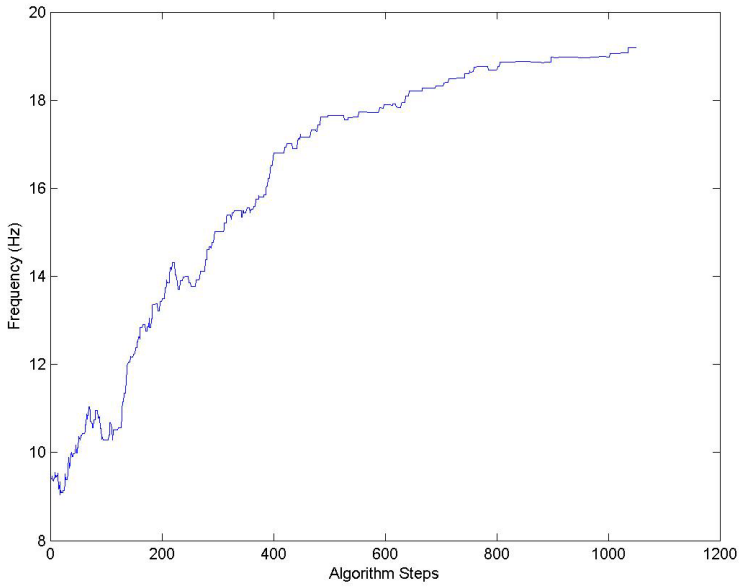

Figure 5.22: Mean population frequency versus iteration number.

the acceleration of membrane. The approximately constant velocity of the membrane following a sawtooth profile fails to take advantage of this finding. Therefore, an optimization experiment that tests dramatically different velocity profiles has the potential to provide great insight into ways of increasing the thrust production of synthetic jets.

5.5.5 Comparison with Model

We can use Equation 4.55 to predict the average force produced by the voice coil-driven synthetic jet prototype described in Section 2.1 and compare the result with the forces measured in Section 5.2. For this jet, $r_o = 0.4763cm$, $r_c = 1.905cm$, $r_{oc} = 3.805cm$, and $\delta = 0.3cm$. The frequency, f, ranged from $1 - 10$ Hz, while the

velocity profile, vp, ranged from $0.1 - 0.9$. This was for a sawtooth forcing profile.

From Equation 4.50:

$$\begin{aligned} F_{out} &= \rho\pi \frac{\delta^2 f^2 r_c^4}{(1-vp)^2 r_o^2} \\ &= \left(1000\frac{kg}{m^3}\right) \pi \frac{(0.003m)^2 (f\frac{1}{s})^2 (0.01905m)^4}{(0.004763m)^2 (1-vp)^2} \\ &= \left(\frac{f}{vp}\right)^2 (1.6414 \times 10^{-4})N. \end{aligned}$$

From Equation 4.49:

$$\begin{aligned} F_{in} &= \eta\rho\pi \frac{\delta^2 f^2 r_c^4}{vp^2\ r_o^2} \\ &= \frac{\sqrt{2}}{2} \left(1000\frac{kg}{m^3}\right) \pi \frac{(0.003m)^2 (f\frac{1}{s})^2 (0.01905m)^4}{(0.004763m)^2 vp^2} \\ &= (\frac{f}{1-vp})^2 (1.1606 \times 10^{-4})N. \end{aligned}$$

Plugging $u_0 = \frac{\delta f}{vp}(\frac{r_c}{r_o})^2$ into Equation 4.35:

$$\begin{aligned} F_{cf} &= 16\, r_o^2\, u_o^2 \rho\ \frac{\chi}{k^2} \\ &= 16\, \rho \frac{r_c^4 \delta^2}{r_o^2} \frac{f^2}{vp^2}\, k^{-2} \chi \\ &= 16(1000\frac{kg}{m^3}) \frac{(0.01905m)^4 (0.003m)^2}{(0.004763)^2}\ \frac{f^2}{vp^2}\, k^{-2} \chi \\ &= \left(\frac{f}{vp}\right)^2 \left(\frac{\chi}{k^2}\right)\ (8.3595 \times 10^{-4})\ N. \end{aligned} \tag{5.1}$$

As this experiment was performed with a prototype with $d_{oc} = 7.62cm$, χ was calculated, using the numerical method discussed in Section 4.4.5 for both $d_{oc} = 7cm$

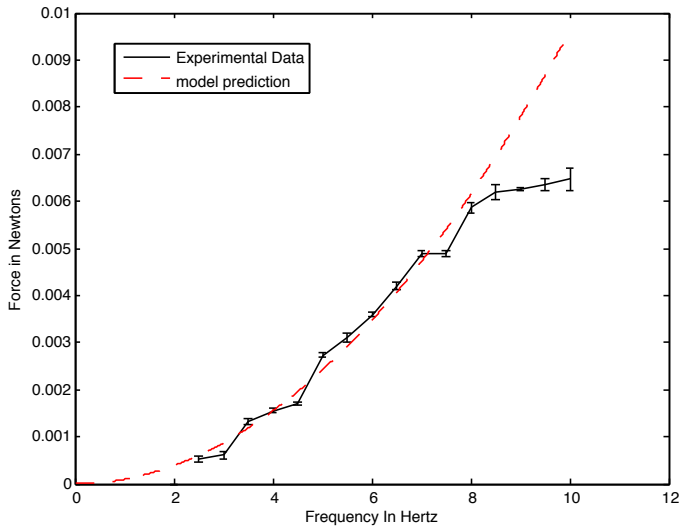

Figure 5.23: A comparison of predicted force versus experimental results (using $\eta = \frac{\sqrt{2}}{2}$) *assuming a membrane displacement of 3mm.*

and $d_{oc} = 8cm$ to see the sensitivity of χ relative to d_{oc}. What was found was that *chi* was larger for $d_{oc} = 7cm$. As d_{oc} does not impact F_{in} or F_{out}, F_{cf} will be calculated for both values to see the difference this makes on the force's magnitude.

$$\begin{aligned} F_{cf(d_c=7cm)} &= \left(\frac{f}{vp}\right)^2 \left(0.3681 \times 10^{-8}\right) \left(8.3595 \times 10^{-4}\right)\ N \\ &= \left(\frac{f}{vp}\right)^2 \left(3.0771 \times 10^{-12}\right)\ N \\ F_{cf(d_c=8cm)} &= \left(\frac{f}{vp}\right)^2 \left(0.5796 \times 10^{-8}\right) \left(8.3595 \times 10^{-4}\right)\ N \\ &= \left(\frac{f}{vp}\right)^2 \left(4.8452 \times 10^{-12}\right)\ N \end{aligned}$$

Thus, the contribution of force from coflow is negligible in this case. This is unsurprising given that d_{oc} is 8 times greater than d_o, and u_{or} is very small. In contrast, the scotch yoke apparatus on which the coflow was first noticed had a d_{oc} that

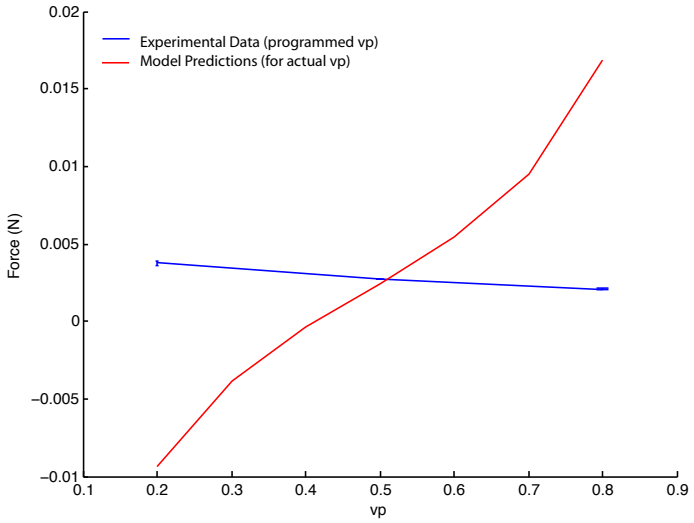

Figure 5.24: Comparison of experimental results with model predictions for variation in velocity profile, *vp*.

was only 4 times greater than d_o and a relatively large magnitude of u_{or}. Plotting the experimental average measured force versus the model predictions (using $\eta = \frac{\sqrt{2}}{2}$ and $vp = 0.5$) as a function of frequency results in a plot (Figure 5.23). This simple model does a surprisingly good job at fitting the experimental data *if we use the assumption that the average membrane displacement is 3 mm*. Given that a precise measurement of membrane displacement is not available for this apparatus, the comparison with the model should be taken as an initial validity check and not an exact comparison. Future comparisons of the model against other experiments will be needed to quantify the model's accuracy.

The model shows a positive correlation between measured and predicted forces, as a function of geometry and frequency, for both of the cases shown above. A trend that is not matched between the experimental results and the model is that of the effect

of velocity profile on force. As can be seen in Figure 5.24, our experimental results show that a lower velocity profile (representing a sawtooth profile in which the piston velocity during instroke is faster than during outstroke) produces a greater thrust. The model, however, has the opposite prediction. The model also predicts that the direction of the force will switch as a function of vp. It is likely that this discrepancy is due, at least in part, to the issues discussed above regarding the relationship between programmed velocity profile and membrane displacement. Thus, the only conclusions that can safely be drawn is that changing the programmed velocity profile does effect the thrust produced.

5.6 Summary of Force Measurement Results

This chapter presented force measurements for an aquatic synthetic jet. A procedure for measuring the synthetic jet's average thrust was developed and experimental repeatability was demonstrated. A direct relationship between frequency of membrane actuation and average thrust was evident. Additional investigations into the effect of membrane velocity profile on thrust were performed, and it was shown that changing the relative in/out flow rates does have an effect on the thrust produced. An automated thrust optimization procedure was demonstrated and its results were shown to be consistent with the other findings in this chapter. Finally, a preliminary comparison of measured versus modeled forces is presented.

Chapter 6

Feasibility of Using Synthetic Jets for Vehicle Propulsion

As discussed in Chapter 1 the motivation for this research is determining the suitability of synthetic jets for small vehicle propulsion. Discussions with biologists revealed that there is a desire among scientists for vehicles small enough to be transported, launched, and recovered by a single person. An application for such a vehicle is the tracking of slow moving creatures that are often carried with the ocean currents. Given the results of the force measurement presented in Chapter 5 have the potential to be used in exactly this sort of vehicle. Small, slow moving vehicles are an ideal application for synthetic jets.

Synthetic jets are clearly not the best method for generating large magnitude thrust. From an efficiency standpoint, applications which require large thrust forces are better suited for the use of propellers (ducted, unducted, or water-jet configuration). Synthetic jets are, however, an attractive AUV (and ROV) propulsion alternative for other reasons. Given that discussions with marine biologists was a motivator for this research, the effect of the propulsors on marine life is particularly interesting.

When vehicles are being used for close observation, or collection, of sea life, propellers pose a risk to the animals. The spinning blades can maim or kill the very creatures the vehicle is trying to observe. Additionally, synthetic jets could be built into the hull of a vehicle without any parts protruding. As protruding parts are more likely to break, using synthetic jets for propulsion may add additional robustness to the vehicle.

A more anecdotal downside of propeller driven vehicles is the unnatural form of their wake. Propellers, on a scale larger than the flagella of microorganisms, do not occur in nature. Thus, it seems reasonable to conjecture that creatures may be scared off by the wake of AUVs and ROVs that are propeller-driven.[1] As vortex ring propulsion is common among ocean animals, it is possible that a vortex ring-propelled AUV would be able to get closer to sea creatures.

Given the relatively small forces produced by synthetic jets, they may prove useful as a *primary propulsion scheme* for only a small class of vehicle applications. More useful may be their possible use as a *secondary propulsion system*. As synthetic jets could be embedded into the vehicle's hull, it is easy to imagine a vehicle with both propeller and synthetic jet capabilities. A traditional torpedo-shaped vehicle with embedded synthetic jets has been built by Mohseni et al.[56], but no performance results have yet been published. As discussed in Chapter 1, synthetic jets have been explored as flow controllers in air. They could very well be used for the same thing

[1] I have spoken to a biologist who describes expeditions in small one-person submarines. When they turn the propellers off, creatures will come very close to them, and they are more likely to see animals that they have never seen before. Turning on the propellers, in his opinion, scares off many creatures.

underwater on AUVs and ROVs. Embedding synthetic jets on a vehicle's hull could prove useful in reducing drag forces. A final intriguing vehicle application of synthetic jets is the design of micro-AUVs. Designing a very small "jellyfish-like" vehicle with a single synthetic jet would allow for the optimization of F_{cf}. Thus, it is conceivable that a fairly efficient small AUV could be designed using a synthetic jet even without needing to incorporate the complicated flexible, variable-diameter fluid chamber of a jellyfish.

6.1 Propulsion Force Requirements

Discussions with biologists[2] revealed that there is a desire for small vehicles (less than a meter in characteristic length[3]) that are capable of slow movement. Given that one of the applications suggested for such a vehicle is the tracking of slow moving creatures that are often carried with the ocean currents. For such an application speeds on the order of 10 cm/s would be desirable. This section will do a feasibility study for a *theoretical vehicle* to asses the practicality of using synthetic jets to meet these velocity requirements.

[2]A meeting with Dr. George Matsumoto and Dr. Bruce Robison, both biologists specializing in marine invertebrates, was held at the Monterey Bay Aquarium Research Institute to discuss the need for, and practicality of, small vehicles with propulsion schemes other than propellers.

[3]The size is driven by the desire of these scientists to have a vehicle which could be transported, launched and recovered by a single person

6.1.1 Steady State Propulsion

For a vehicle moving at a constant velocity the propulsion force must overcome the drag force. The drag force, F_D, for a vehicle as

$$F_D = \frac{1}{2} C_D \rho v_v^2 A_v, \tag{6.1}$$

where v_v^2 is the vehicle's velocity, A_v is the vehicle's characteristic area, and C_D is the coefficient of drag. This equation can also be rearranged to find the coefficient of drag when the drag force is know:

$$C_D = \frac{F_D}{\frac{1}{2}\rho v_v^2 A_v}. \tag{6.2}$$

C_D is dependent on the vehicle's geometry and velocity. As this thesis is a feasibility study for synthetic jets, this section will provide equations for an idealized spherical vehicle. A sphere is an interesting hull shape to consider as it would allow for equal drag in all directions. Thus, for a truly neutrally buoyant vehicle, the necessary thrust needed for a given velocity would be independent of desired direction of motion (though the configuration of the thrusters on the sphere's hull would dictate the directions which the vehicle could travel). The calculations in this section will be performed for a spherical vehicle with a 12 cm diameter. The thrusters embedded in this vehicle will be loosely based on the dimensions of the voice coil-driven jets presented in Chapter 5. Thus, they will have an initial chamber diameter, d_c, of 3.81 cm. I will assume that they have a piston configuration as shown in Figure 4.6.

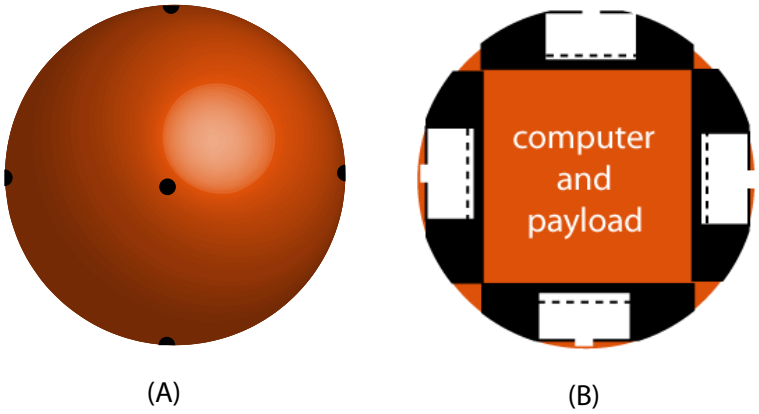

Figure 6.1: (A) depicts a hypothetical synthetic jet propelled spherical vehicle. The synthetic jets are the black circles on the hull. (B) shows a the vehicle sliced in half.

Given that the jet's are embedded in a spherical hull, where $r_s \gg r_o$, we would expect the force contribution from coflow to be negligible. Thus we can use Equation 4.56 to calculate the expected average thrust for the jet:

$$\bar{F}_{(u_{cf}=0)} = \rho\pi\delta^2 f^2 \left(\frac{r_c^2}{r_o}\right)^2 \left[\frac{2\,vp - \sqrt{2}(1-vp)}{2\,vp\,(1-vp)}\right]. \tag{6.3}$$

For simplicity let's assume a sawtooth membrane velocity profile of $vp = 0.5$, a frequency of 8 Hz, and an initial piston displacement, δ, of 3 mm. Thus,

$$\bar{F} = 1000 \times \pi \times (0.003)^2 \times (8)^2 \times \left(\frac{(0.0191)^2}{0.00475}\right)^2 \left[\frac{2 \times 0.5 - \sqrt{2}(1-0.5)}{(2\times 0.5)\times(1-0.5)}\right] \tag{6.4}$$

$$= 0.0063N. \tag{6.5}$$

Returning to Equation 4.56, we can calculate the speed that the spherical vehicle

could move based on this $\bar{F}$. The value of C_D for a smooth sphere can be found using a look-up chart such as the one presented in Newman [79]. This value is Reynolds number dependent. For a 12 cm diameter sphere moving at between 5 and 15 $\frac{cm}{s}$, C_D is roughly 0.5.

Thus, the drag force that needs to be overcome is

$$\begin{aligned} F_D &= \frac{1}{2} C_D \rho v_v^2 A_v && (6.6) \\ &= \left(\frac{1}{2}\right)^2 \times 1000 \times v_v^2 \times \left(\pi \times 0.06^2\right) && (6.7) \\ &= 2.8274 \times v_v^2. && (6.8) \end{aligned}$$

From the above equation, it follows that a thruster producing 6.3 mN of force could propel the spherical vehicle at 4.7 $\frac{cm}{2}$. This is below the 8 to 10 $\frac{cm}{s}$ velocities we would like to achieve, so a method of increasing the thrust must be found. Using the design tables in Chapter 4 we can see that force increases with δ^2, so doubling the membrane throw would quadruple the force. At 25.2 mN of thrust, the vehicle could be propelled at 9.4 $\frac{cm}{s}$. Alternatively, force increases with r_c^4, so increasing the fluid chamber diameter would have a great impact on the thrust produced.

6.1.2 Acceleration and Deceleration

It is important to remember that the calculations presented in the previous section are for *steady state* propulsion of a vehicle. This thesis is motivated by the idea of propulsion in regimes where a high level of maneuverability is important. Therefore,

additional calculations must be performed to evaluate the acceleration and deceleration capabilities of a vehicle propelled by synthetic jets. When a vehicle is moving through fluid it is necessary to accelerate (or decelerate) not only the vehicle itself but also the fluid surrounding the body. In other words, the inertia of the fluid must be overcome. This inertia is referred to as the **added mass**, m_a. Thus, when calculating the force needed to accelerate the vehicle, the mass to be accelerated can be written $m = m_v + m_a$, where m_v is the vehicle's mass and m_a is the added mass.

For a sphere:

$$m_a = \frac{1}{2}\rho V_s \tag{6.9}$$

where V_s is the sphere's volume. Therefore:

$$\begin{aligned} m &= m_s + m_a && (6.10)\\ &= \rho\pi\frac{4}{3}r_s^3 + \frac{1}{2}\rho\pi\frac{4}{3}r_s^2 && (6.11)\\ &= \rho\pi\frac{4}{3}r_s^3\left(1+\frac{1}{2}\right) && (6.12)\\ &= 2\rho\pi r_s^3. && (6.13) \end{aligned}$$

Thus, the force needed to accelerate the vehicle can be written as

$$\begin{aligned} F &= ma && (6.14)\\ &= 2\rho\pi r_s^3\, a_s && (6.15) \end{aligned}$$

Thus, the sphere's acceleration, a_s, is

$$a_s = \frac{F}{2\rho\pi r_s^3}. \tag{6.16}$$

Using the same parameters as in the previous section (for a sphere with a 6 cm radius), an average thrust of 0.0063 N would result in an acceleration of 4.6 $\frac{mm}{s^2}$.

$$\begin{aligned} a_s &= \frac{F}{2\rho\pi r_s^3} && (6.17)\\ &= \frac{0.01}{2\rho\pi(0.06)^3} && (6.18)\\ &= 0.0046\frac{m}{s^2} && (6.19) \end{aligned}$$

At this acceleration rate it would take approximately 17.3 seconds for the vehicle to reach a velocity of 8 $\frac{cm}{s}$. Such a slow acceleration rate would probably be unacceptable for maneuverability critical vehicle regimes. However, making the jet modifications discussed above that would bring the predicted average thrust for a single synthetic jet to 0.0252 N (by doubling the piston throw)would increase the acceleration rate to 5.8 $\frac{cm}{s^2}$. At $a_s = 5.8\frac{cm}{s^2}$, it would take approximately 1.3 second to achieve a velocity of $8\frac{cm}{s}$. This is a much more reasonable acceleration time. However, it is clear that other modifications, particularly increasing the fluid chamber diameter, could increase the acceleration time even further.

The calculations in this section are intended to demonstrate feasibility, not optimization. It is unlikely that a perfectly spherical vehicle shape would be chosen. If omni-directionality is not a concern, a much more streamlined body can be designed.

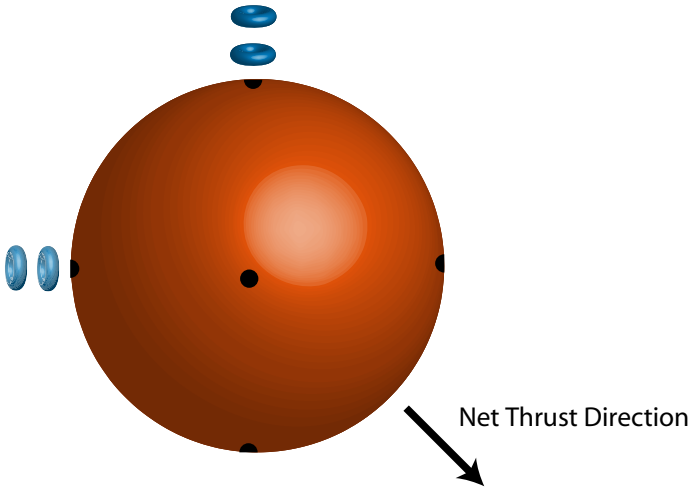

Figure 6.2: Illustration of the use of two thrusters to augment net thrust.

Such a design would require smaller jet forces for both steady state propulsion and acceleration. Additionally, if a spherical body *were* chosen, using a single thruster at a time would be the minimum force production case. One can envision using multiple thrusters at once, as shown in Figure 6.2, to achieve greater thrusts.

Based on these calculations, it seems reasonable to propose that synthetic jets *can* produce enough thrust to be considered for the propulsion of small vehicles needing to achieve velocities on the order of 8 $\frac{cm}{s}$ with reasonable acceleration rates.

6.2 Practical Concerns

In Chapter 1 practical reasons for using synthetic jets for vehicle propulsion were listed. This section will address these reasons in more depth.

Robustness is an attribute of synthetic jets which should prove beneficial if they are integrated into an underwater vehicle. Synthetic jets, in the simple designs presented

in this thesis, have a single moving part (the membrane actuator). For underwater robotic applications, the minimization of moving parts is important as it reduces the vehicle's number of potential failure points. Thus, the simpler the thruster design the better.

For applications that entail maneuvering in tight spaces, the minimization (if not elimination) of appendages protruding from the vehicle's hull becomes important. As mentioned above, the minimization of the vehicle's potential failure points is an important design consideration. The single orifice needed for a synthetic jet seems ideally suited for flush integration into a vehicle hull. This is demonstrated in the vehicle designed by Mohseni et al. [56].

In addition to minimizing moving and external parts, minimizing seals is important to the robustness of a vehicle. The reasoning for seals is twofold: to prevent water (particularly corrosive seawater) from getting into the vehicle and damaging electronics and other components, and to prevent any of the vehicle's internal components from escaping into the environment. This latter consideration would be particularly important for applications involving pristine, unexplored bodies of water (Lake Vostok, in Antarctica, for example). To prevent water from entering around the shaft of a propeller (on a propeller driven vehicle) a shaft seal must be used. Designing such a seal has challenges as a propeller shaft is rotating. Our voice coil-driven synthetic jet needs only one critical seal[4]. This seal is the one between the membrane and the fluid chamber.

[4]The phrase "critical seal" is being used here to denote a seal which, if compromised, would allow water to leak into the vehicle. A "non-critical seal" would be one which, if compromised, would not threaten the hull's integrity.

For animal tracking applications, creating a vehicle which does not scare off the intended targets is crucial. Obviously the impact of any lighting system or active sensor must be considered carefully. Additionally, the wake structure of the vehicle should be examined. Currently, practically all AUVs and ROVs are propeller driven. Above the micro-organism level, propeller-like propulsion systems are non-existent.[5] It seems reasonable to expect that a creature confronted with a wake pattern that it has never previously encountered would be scared off. Synthetic jets produce a wake structure similar to that of jellyfish. Thus, we hypothesize that this wake structure would be less disturbing to creatures.

6.3 Comparison to Other Propulsion Systems

The direct comparison of synthetic jets to other means of underwater propulsion must be done carefully. As there is not one single metric of comparison, a propulsion scheme must be chosen depending on the circumstances under which it will be used. This section will compare synthetic jets, using a number of performance characteristics, to other propulsion methods: ducted and unducted propellers, water jets, and flapping foils.

The typical propulsor for an underwater vehicle (AUV or ROV) is a propeller. As discussed in Chapter 1 this propeller may be ducted or unducted. Propellers, like synthetic jets, have a single moving part (a rotating shaft) and a single seal. However, unlike the seal on a synthetic jet, a propeller's seal must accommodate

[5] At the micro-organism level, the rotary motion of the flagellum of some bacteria comes to mind.

a rotating shaft which adds to the difficulty of achieving a water-tight seal. More importantly, a propeller must stick out of the vehicle's hull (unless a waterjet design, discussed in detail below, is used). This leaves the propeller prone to breakage during launch, recovery, and operation. The helical wake of a propeller does not have a biological analog, with the microscale exception discussed previously.

A water jet is a through jet which pulls water in through one orifice and expels it through another orifice. This fluid pumping is *typically* achieved using a rotor/stator propeller system. Similar to a propeller, this can entail as little as one moving part and a single seal. However, unlike a propeller, a water jet system is internal to the hull. This approach to AUV propulsion can be seen on Stanford's OTTER vehicle [10]. As with propellers, a water jet's wake would not be mistaken for that of a biological organism. Clearly the water jet configuration has many advantages over a traditional propeller driven system in terms of its suitability for low-speed applications requiring maneuverability. However, there are mechanical design tradeoffs to the use of water jets on AUVs and ROVs. As separate inflow and outflow orifices are needed, the placement of both orifices and and the connecting piping must be considered. This is substantially more complex than the embedding of a single orifice synthetic jet with no connective tubing needed.

An additional aspect of any propeller driven system, be it in a ducted, unducted or water jet configuration, is directionality. Propellers are inherently right or left handed, and thus their helical wake is not truly axisymmetric. Thus, a vehicle often heels slightly to counteract the torque. Synthetic jet flow, as produced by a cylindrical

jet with a circular orifice, is axisymmetric.

Flapping foil propulsion, which is still in its infancy as far as oceangoing AUVs and ROVs are concerned, typically entails multiple moving parts (servos and linkages). This increases the possible points of failure. The number of seals is dependent on the particular design. For a flapping foil to work, particularly in a biologically inspired carangiform configuration, the fin must protrude from the hull. As mentioned above for propellers, this adds to the likelihood of damage due to impact with objects. Clearly the wake produced by a flapping foil has a great similarity to that produced by a fish.

A more complicated comparison between synthetic jets and other propulsors is efficiency. As can be seen in the models presented in Chapter 4 during the instroke of the membrane the force (with the exception of any self-induced coflow forces) is acting in an opposite direction than during the outflow stroke. Thus, energy used during the instroke is being used to produce a force in the *opposite* direction that thrust is desired. This is inherently wasteful, energy efficiciency-wise. It is unlikely that synthetic jets would ever be chosen for their efficiency. A study of synthetic jet efficiency has never been done and thus direct comparison to other propulsion schemes is not currently possible.

6.4 Vehicle Conclusions

This chapter is intended to serve as an initial feasibility discussion of using synthetic jets as underwater vehicle propulsors. The ability of these jets to propel small, slow

moving robots was shown. Additionally, a comparison of synthetic jets to traditional underwater vehicle propulsors is presented.

Chapter 7

Conclusions and Future Work

As discussed in Chapter 1, the motivation for this research is determining the suitability of synthetic jets for small vehicle propulsion. Prototype synthetic jets were constructed to gain a further understanding of the fluid structures and forces that they could produce. A synthetic jet force model was developed to aid in the design of such devices. This chapter will briefly summarize the findings of this thesis and discuss future directions for work in this area.

7.1 Summary of Results

7.1.1 Force

This thesis confirmed that a net thrust can be produced using a synthetic jet underwater. As was shown in Chapter 5's force measurement experiments, thrust increases with frequency. This trend is also clearly captured in the model presented in Chapter 4. A genetic algorithm-driven automatic optimization process is presented and shown to produce the same results as a brute force sampling of the parameter space. Applications of this process to creating more complex membrane forcing profiles are

described.

7.1.2 Flow Structure

Fluid visualization performed using both dye and digital particle image velocimetry (DPIV) confirmed that vortex rings are formed during synthetic jet outstroke. This is not a new result, as it has been previously reported in both air and water synthetic jets. A more intriguing result is the confirmation of a vortex ring forming internal to the fluid chamber during the instroke stage. This formation has been previously predicted in flow models (initially by Rizzetta et al. [29]), yet this was the first experimental visualization of this phenomenon.

The most significant fluid visualization result presented in this thesis is the presence of a self-induced coflow. As earlier visualization experiments and simulations have focused on synthetic jets on a flat plate, or with an orifice diameter (or slit width in the case of rectangular jets) much greater that the outer diameter of the fluid chamber, little attention has been paid to the flow upstream of the orifice. The DPIV visualizations presented in Chapter 3 and Appendix A show that the upstream fluid is effected by the jet and that this effect has the potential to add to the jet's net thrust.

7.1.3 Modeling

In Chapter 4 a new model for synthetic jet force was presented. This model builds on earlier force models (Mohseni [48], Müller et al.[50], and Polsenberg Thomas et al.[62])

and contributes new insight into the inflow stage. A model of the self-induced coflow contribution is constructed using a conformally mapped potential flow approach. The model is then compared to Chapter 5's force measurements, and a good agreement between model and experiment is found. A design table is created which details the effects that varying jet geometry parameters will have on the force produced by the jet.

7.1.4 Vehicle Feasibility

Chapter 6 presents a discussion on the feasibility of using synthetic jets to propel small underwater vehicles. Based on the model (Chapter 4) and force measurements (Chapter 5) it is reasonable to conclude that synthetic jets do offer a reasonable method of propulsion for small vehicles to be used in slow speed applications. Calculation of projected vehicle velocity and acceleration are shown.

7.2 Future Directions

The possibility of synthetic jets inducing a coflow that augments their thrust production is a new idea. This thesis raises the question of what effect the jet's outer geometry has on the fluid velocities upstream of the orifice. The coflow model presented here is a very preliminary study meant primarily to verify that the inflow could produce appreciable upstream velocities for a cylindrical synthetic jet and thus explain the results of Chapter 3's flow visualization experiments. A more thorough analysis of this portion of the flow will undoubtedly require a closer look at viscous

effects and boundary layer formation on both the orifice plate and outer chamber walls.

While the model presented here seems to accurately predict the effect of jet geometry and membrane actuation frequency on produced force, it was not successful in predicting the effect of membrane velocity profile. As the force results show that changing the profile *did* have an effect on thrust. this is an area for further research that has the potential to broaden the range of forces that a given jet geometry can produce. The automated optimization process presented in Section 5.5 should prove a useful tool for this exploration.

In conclusion, this thesis has demonstrated that a net thrust can be produced by a synthetic jet and that the jet's geometry and forcing profile can be altered so as to modify the magnitude of the thrust. The practical benefits, from both an engineering and marine ecology standpoint, of using synthetic jets on AUVs and ROVs were presented. The modeling and design charts presented here can serve as a starting point for the design optimization of synthetic jets given size and/or thrust constraints.

The driving goal of this thesis was to determine whether synthetic jets may be useful for propelling AUVs and ROVs. I believe the answer to that query is "yes."

Appendix A

DPIV Visualization of Self-Induced Coflow

This Appendix presents DPIV velocity images for an entire in-out cycle of the scotch yoke driven synthetic jet prototype as presented in Chapter 3. This yoke's wheel spun at a frequency of ≈ 1.2 Hz. Image pairs were taken at a rate of 15 Hz, with a 5 ms time step between images in a pair. The data was processed using the process described by Willert [67], with a processing window of 32×32 pixels and a step size of 16 pixels. Figure A.1 shows a sample pair of photographs from this experiment, for orientation and size comparison. Note that this experiment was performed on the prototype described in Section 2.2 and the dimensions for this jet can be found there.

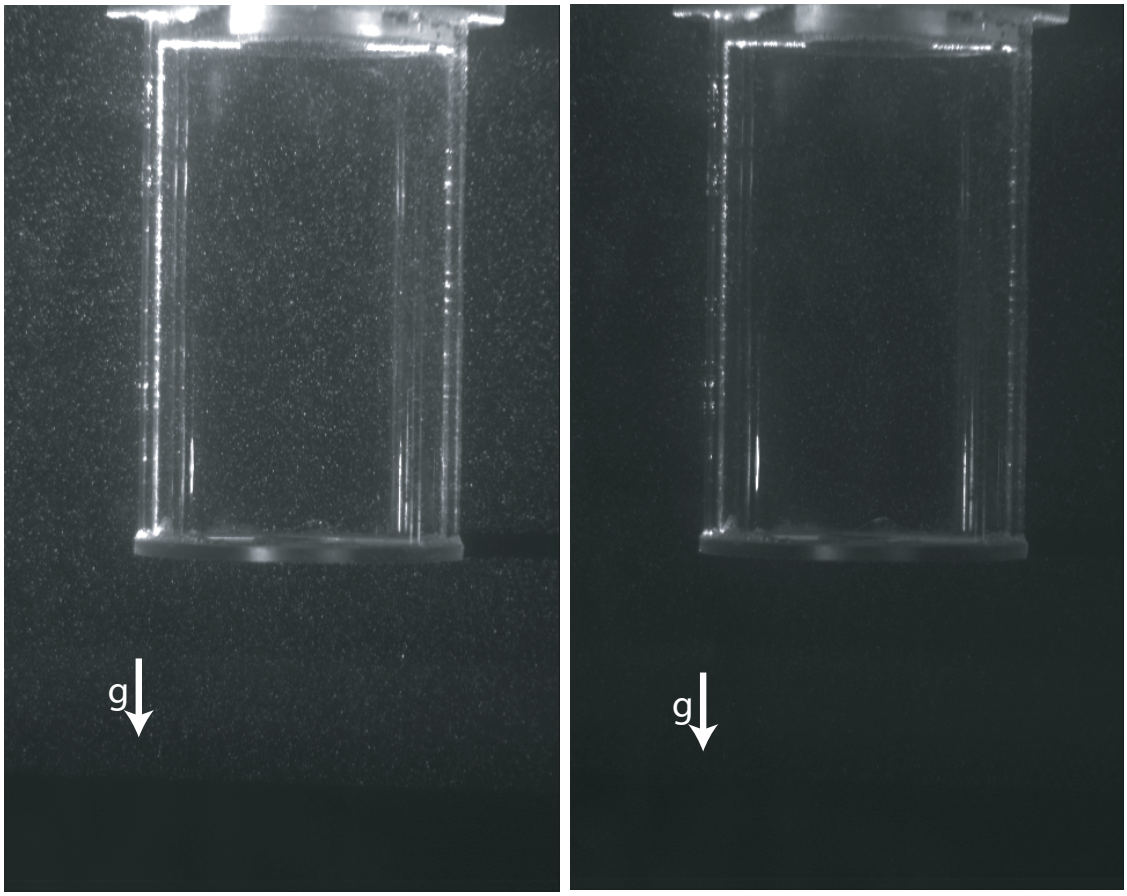

Figure A.1: A sample pair of photographs used for this DPIV experiment.

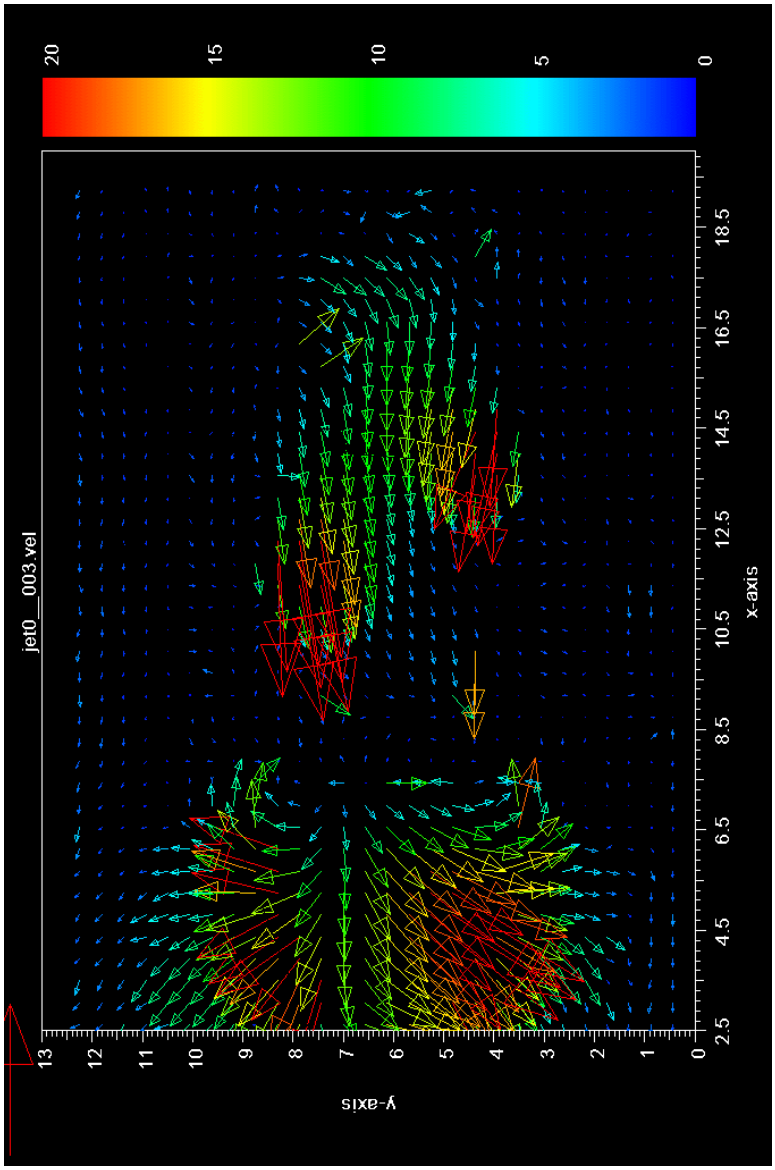

Figure A.2: Velocity comparison of DPIV frames 2 and 3.

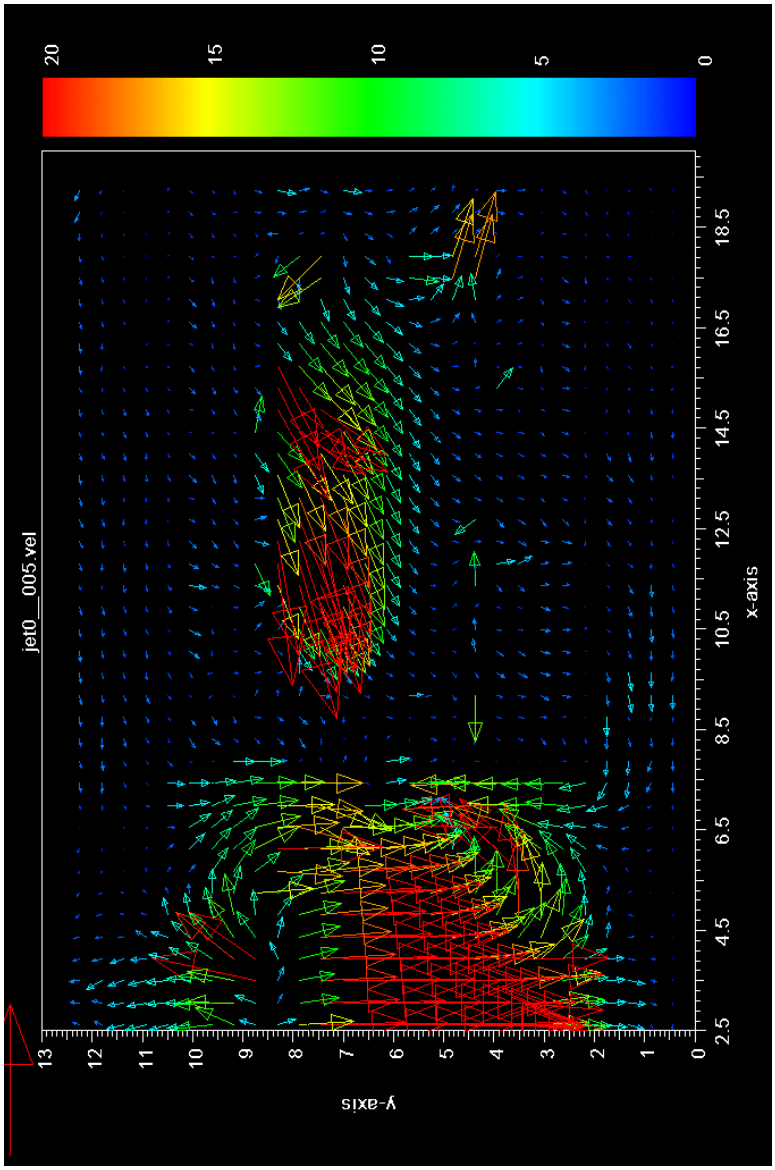

Figure A.3: Velocity comparison of DPIV frames 4 and 5.

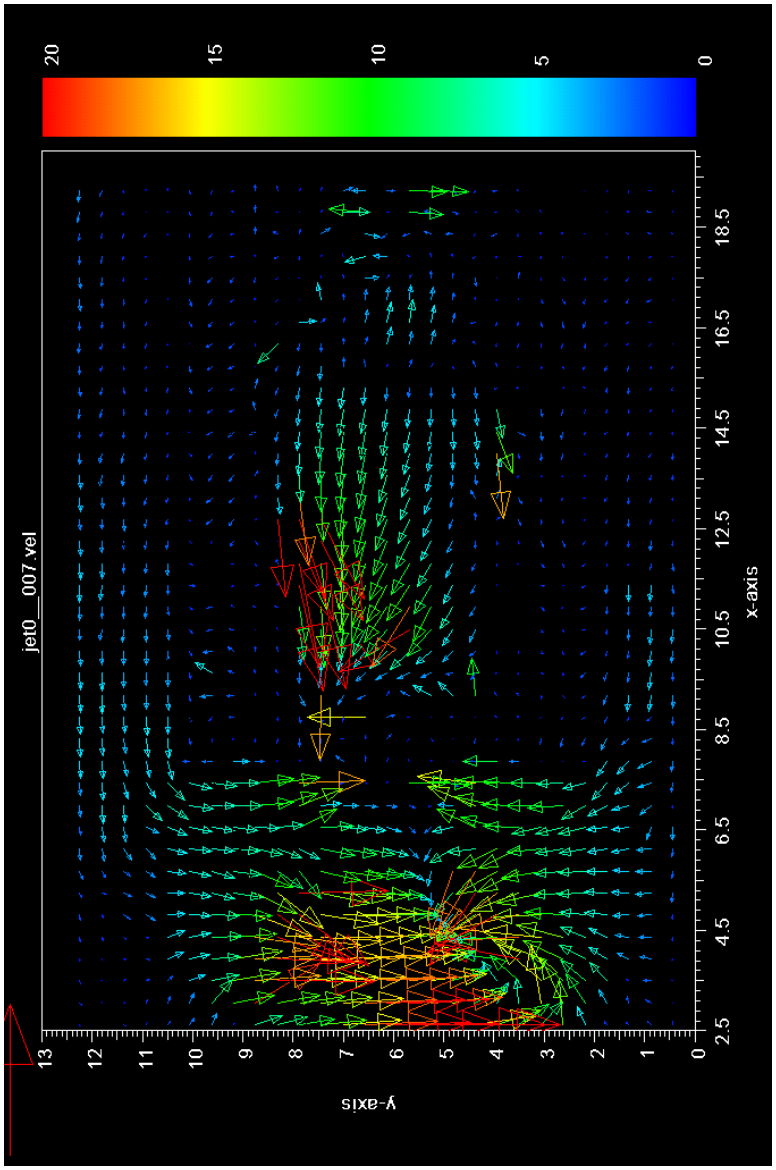

Figure A.4: Velocity comparison of DPIV frames 6 and 7.

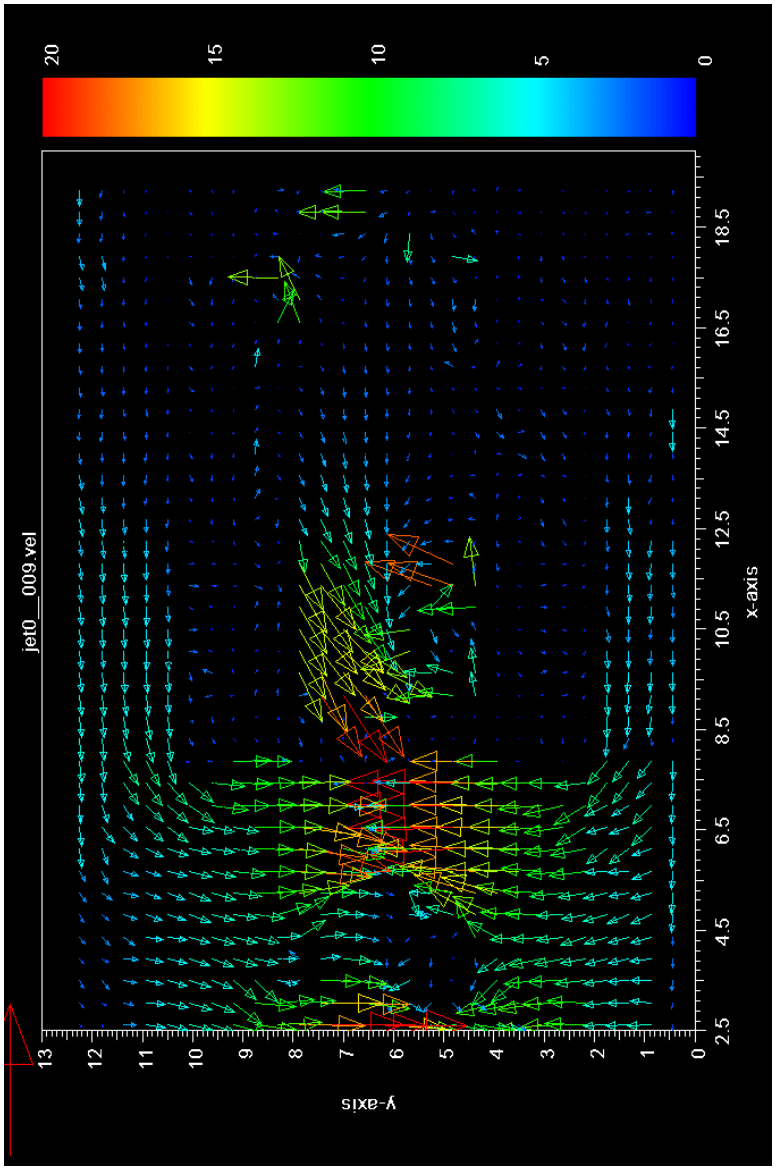

Figure A.5: Velocity comparison of DPIV frames 8 and 9.

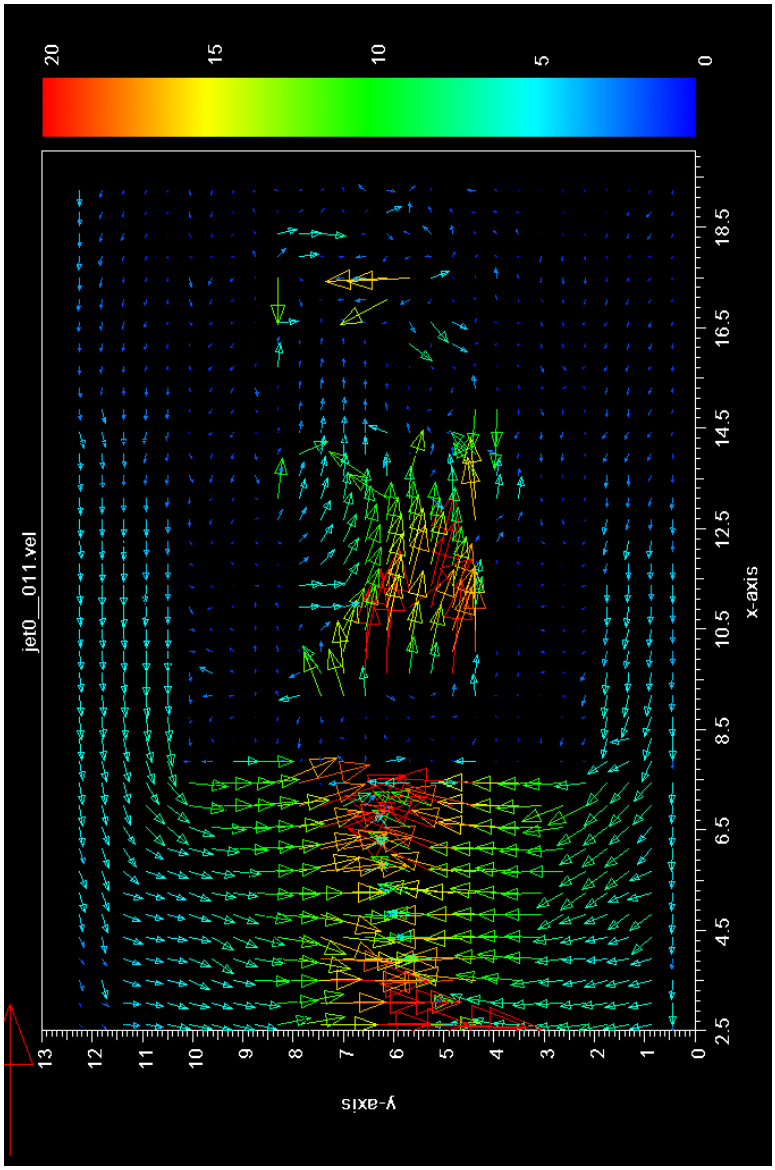

Figure A.6: Velocity comparison of DPIV frames 10 and 11.

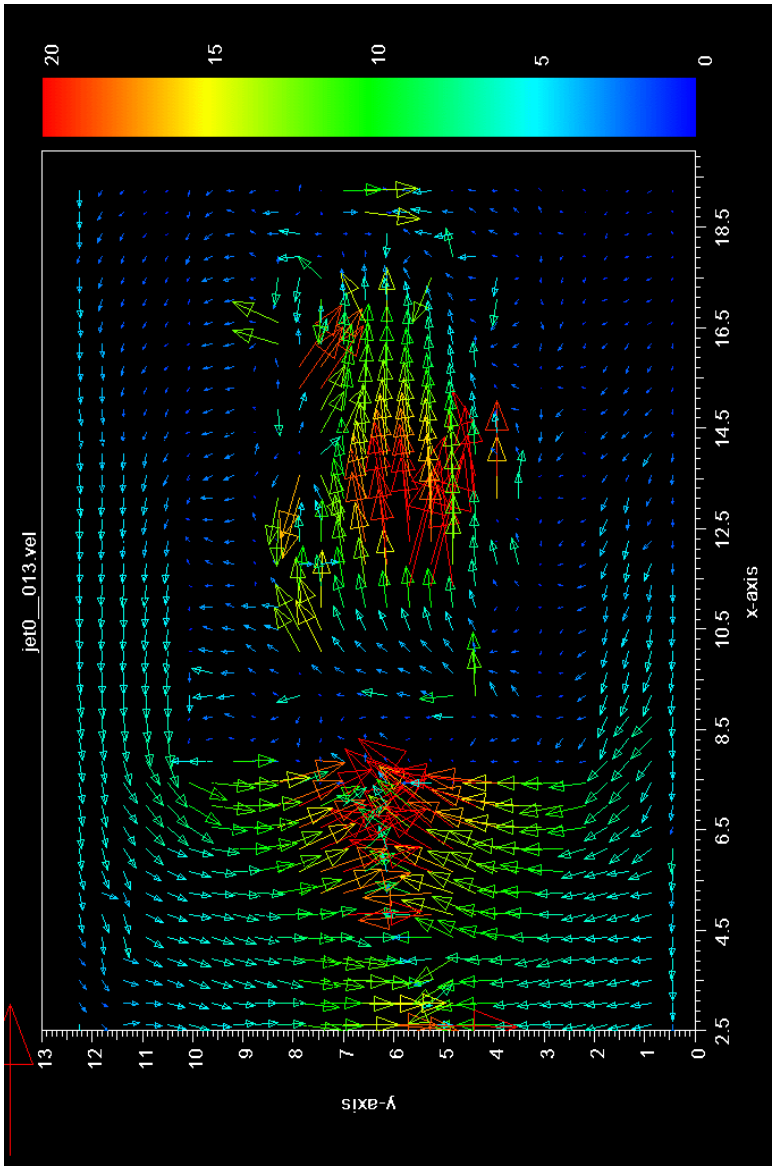

Figure A.7: Velocity comparison of DPIV frames 12 and 13.

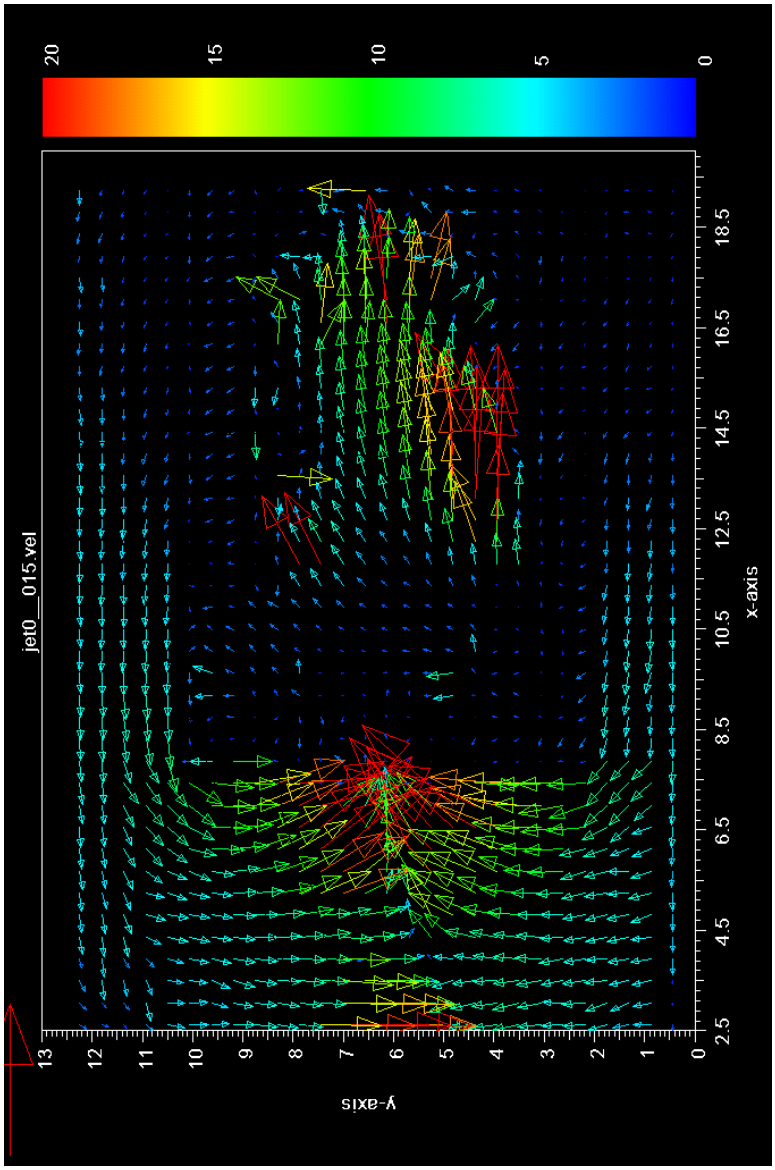

Figure A.8: Velocity comparison of DPIV frames 14 and 15.

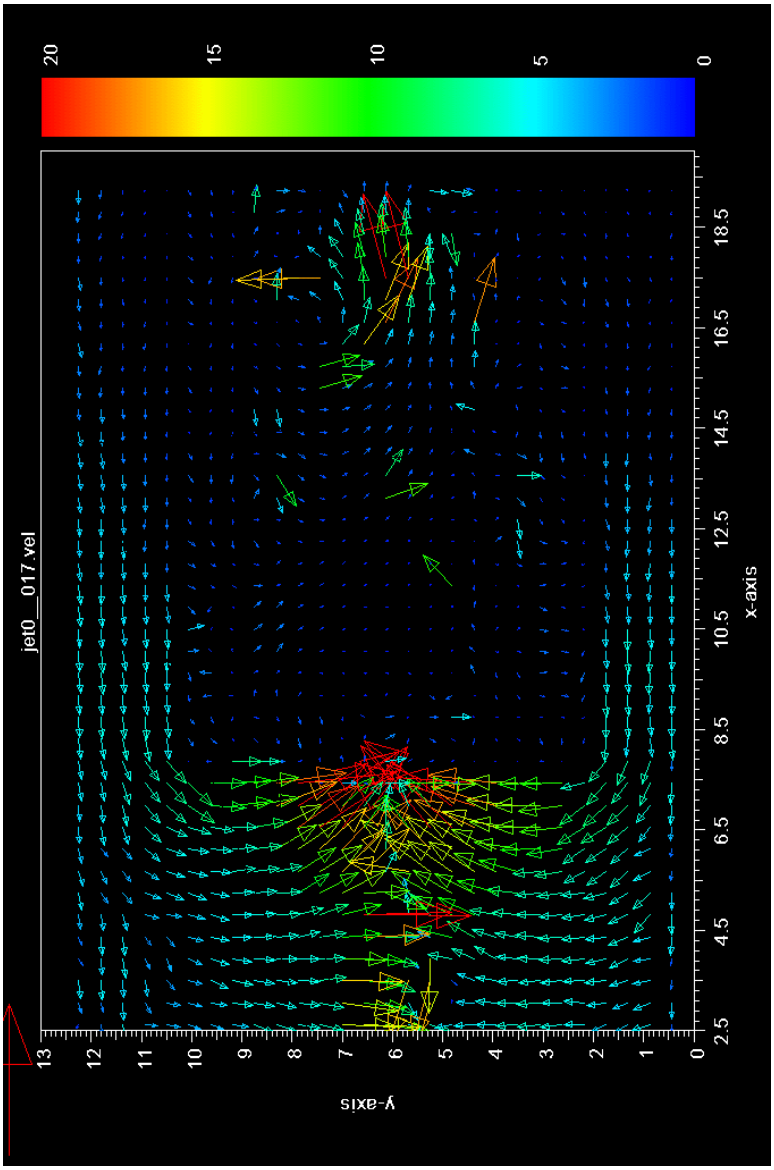

Figure A.9: Velocity comparison of DPIV frames 16 and 17.

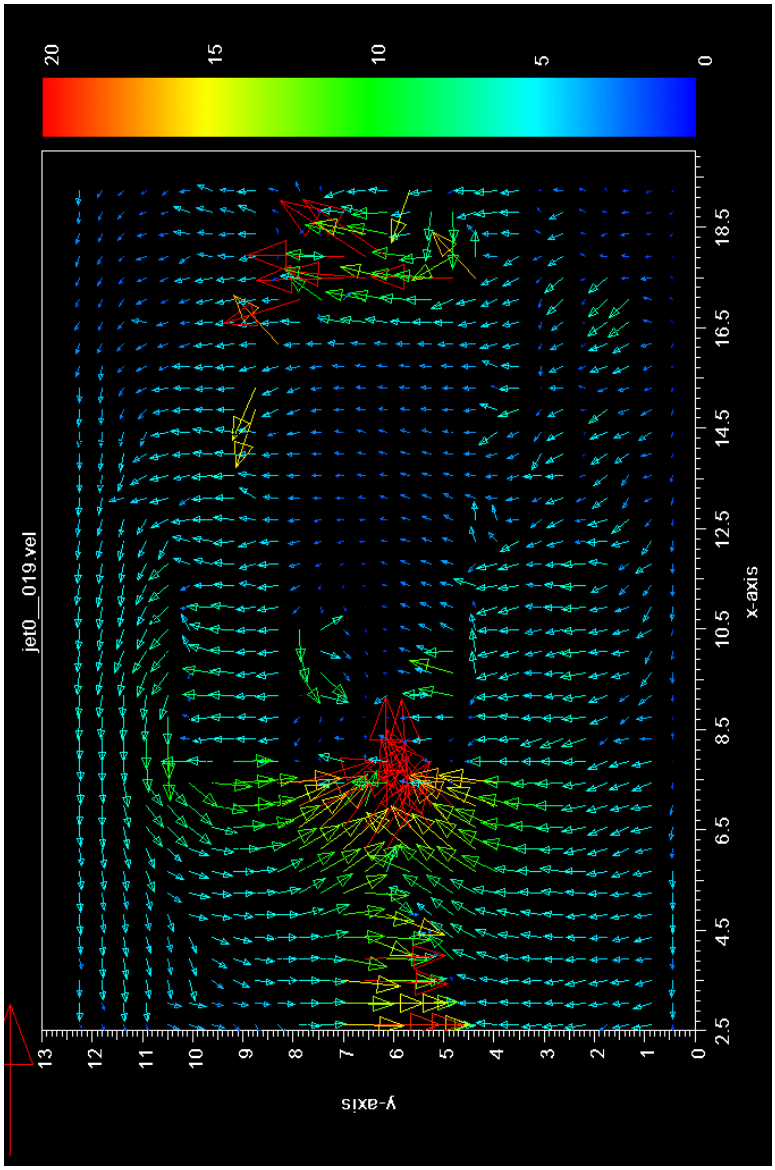

Figure A.10: Velocity comparison of DPIV frames 18 and 19.

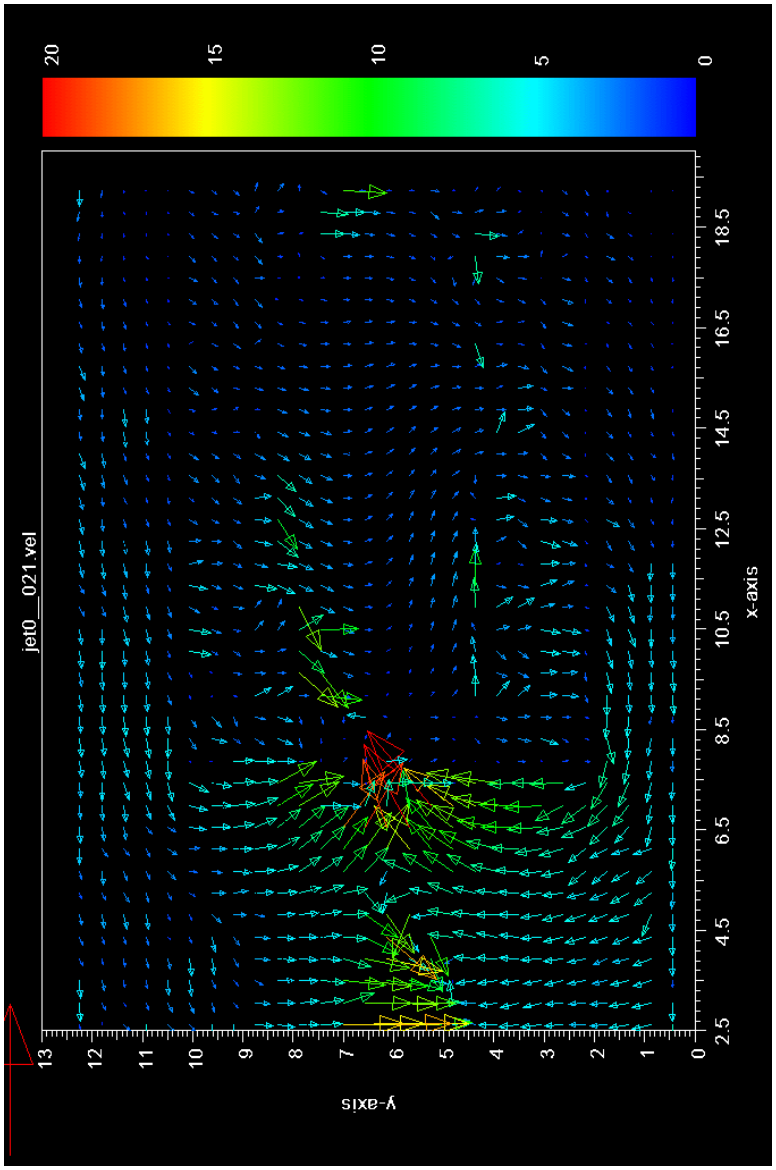

Figure A.11: Velocity comparison of DPIV frames 20 and 21.

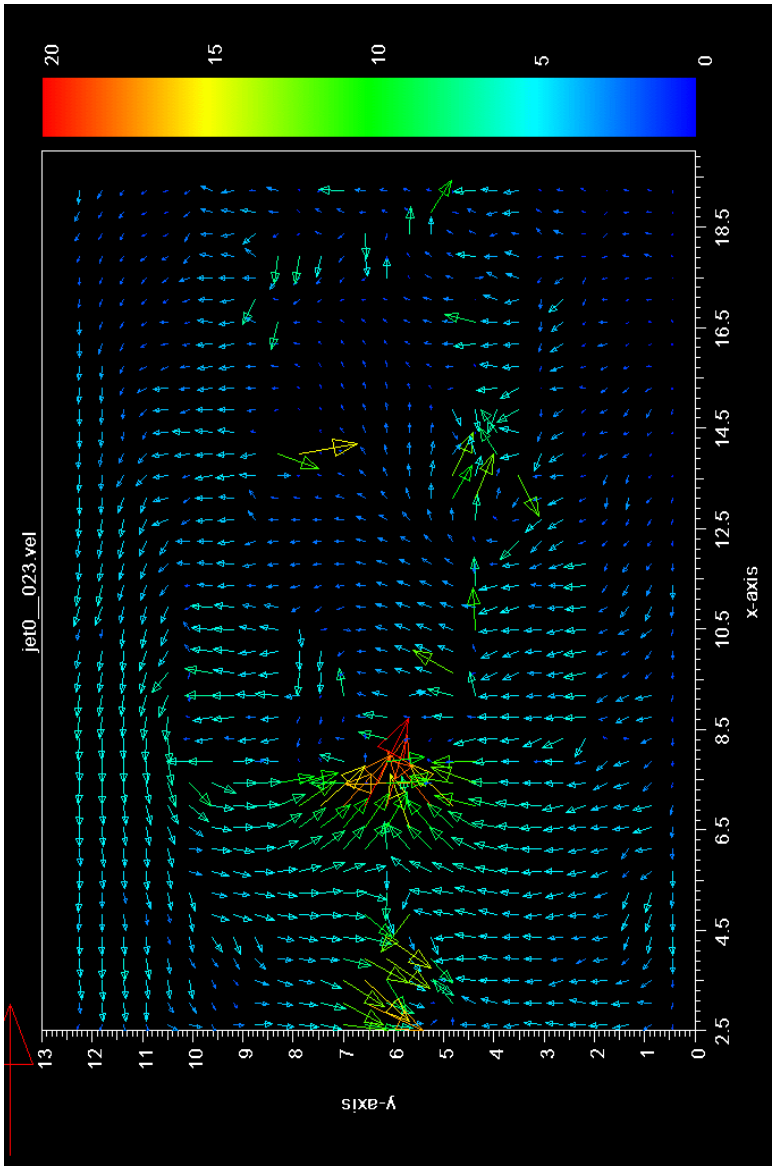

Figure A.12: Velocity comparison of DPIV frames 22 and 23.

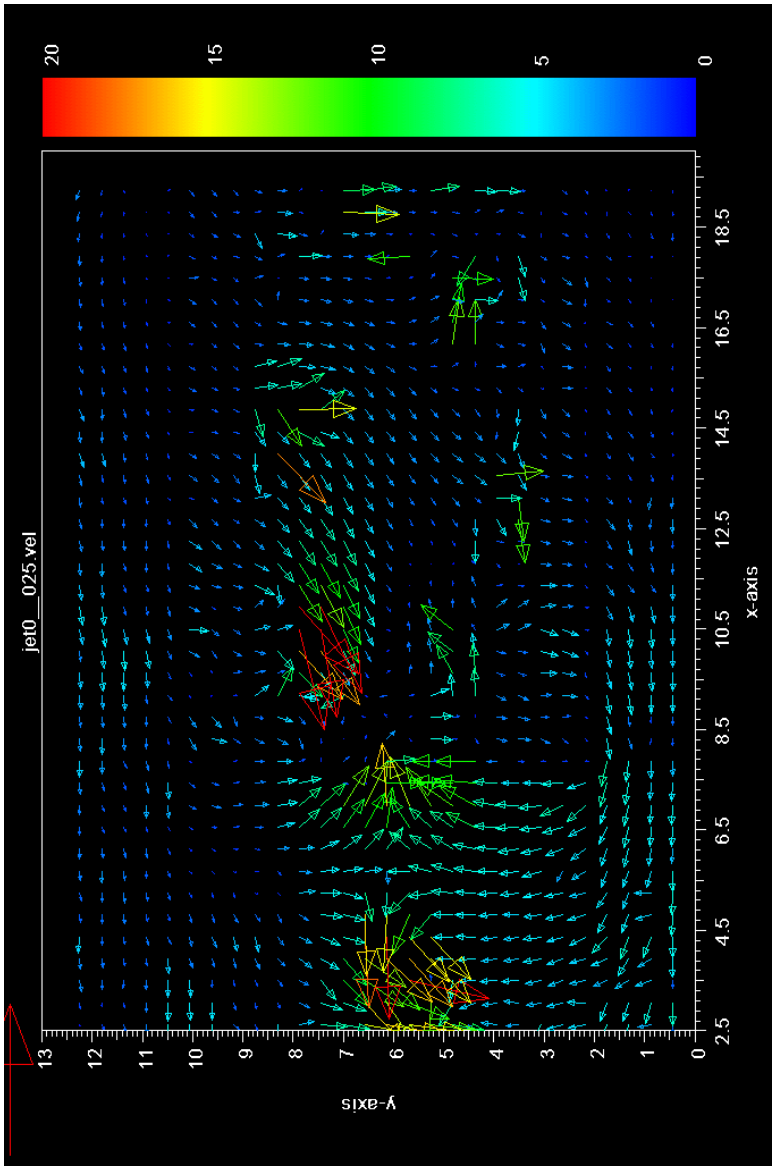

Figure A.13: Velocity comparison of DPIV frames 24 and 25.

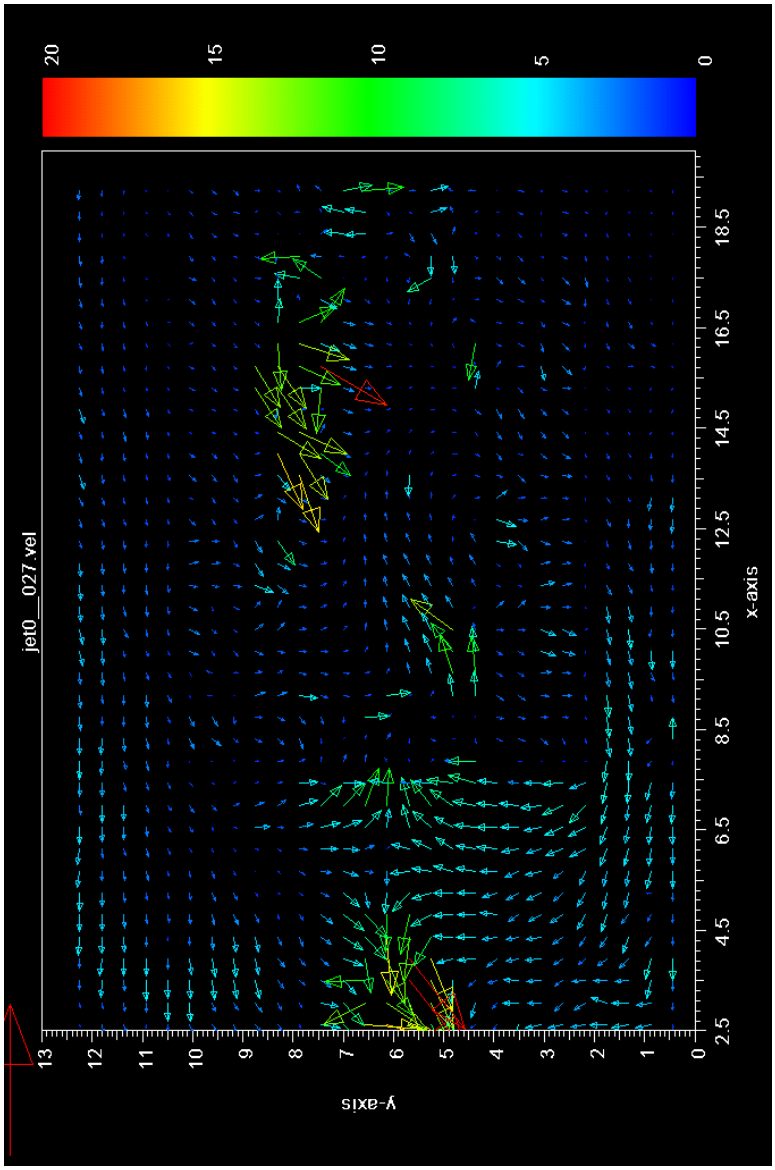

Figure A.14: Velocity comparison of DPIV frames 26 and 27.

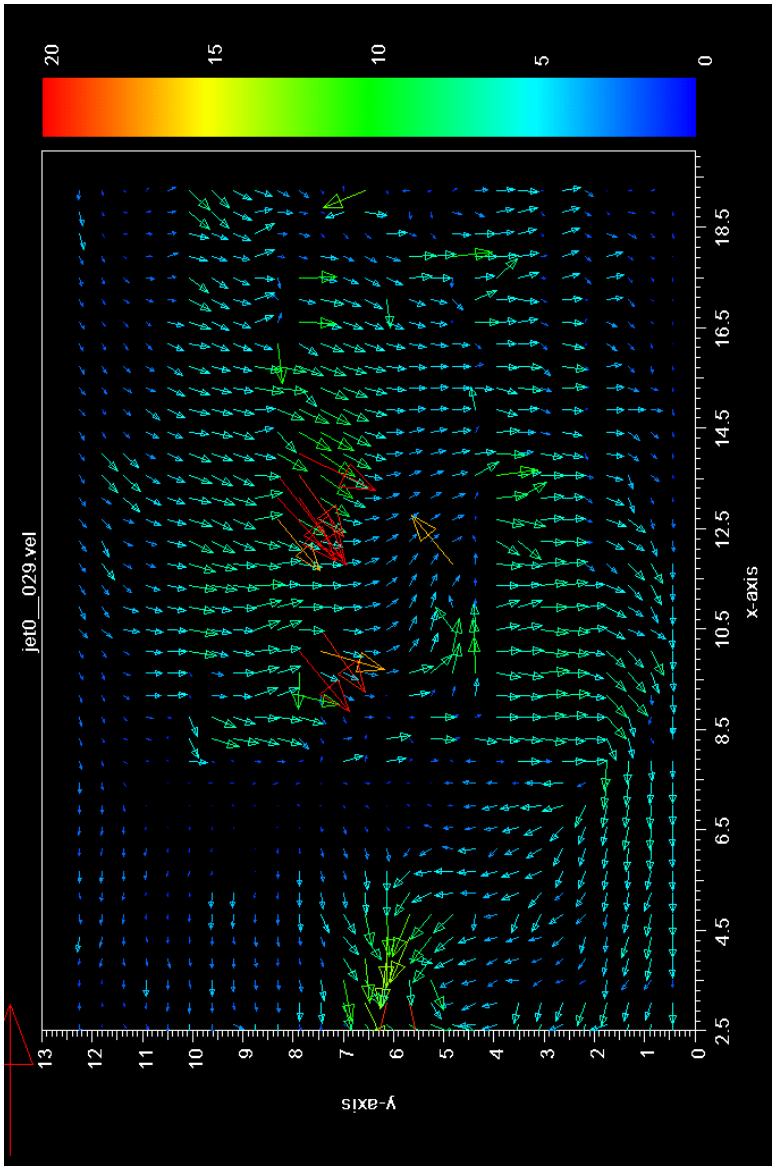

Figure A.15: Velocity comparison of DPIV frames 28 and 29.

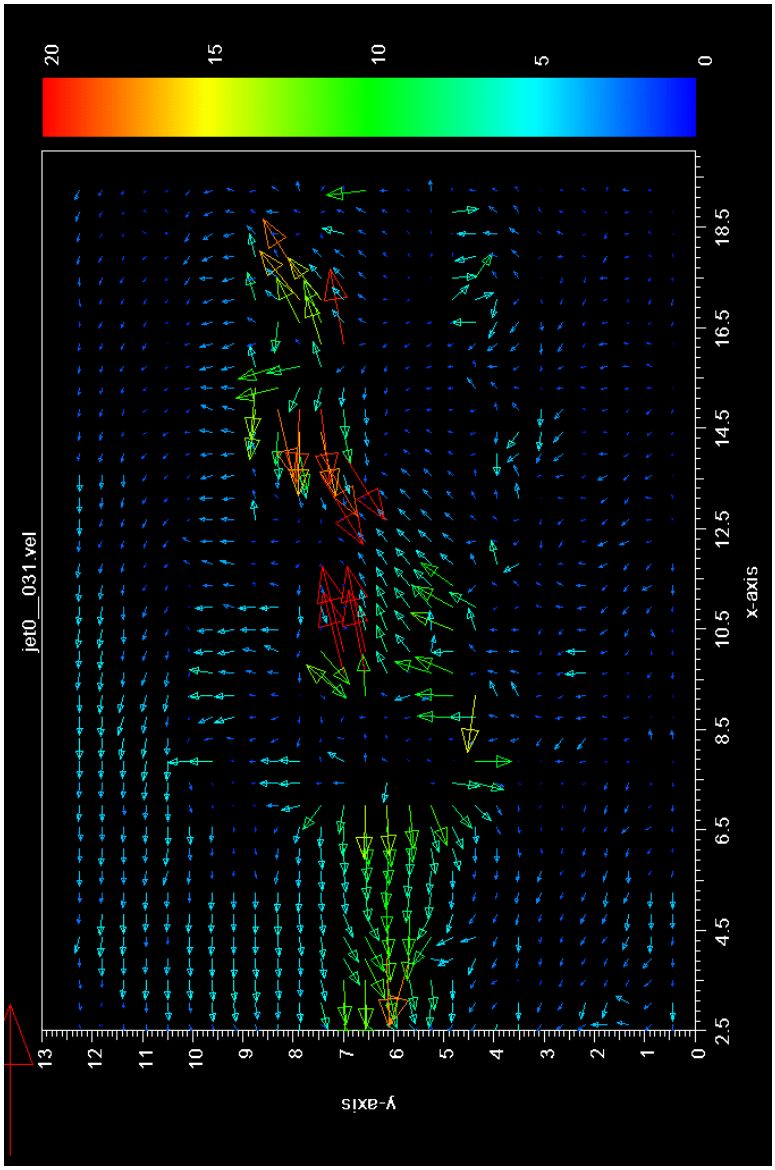

Figure A.16: Velocity comparison of DPIV frames 31 and 31.

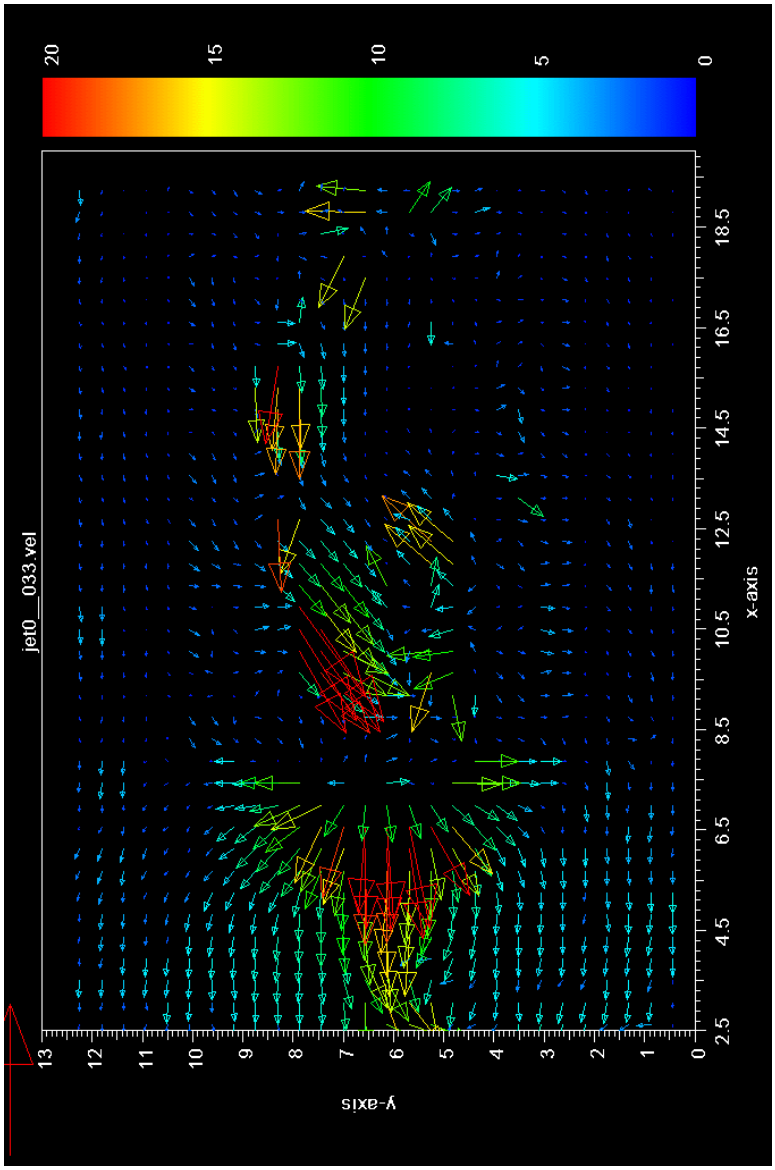

Figure A.17: Velocity comparison of DPIV frames 32 and 33.

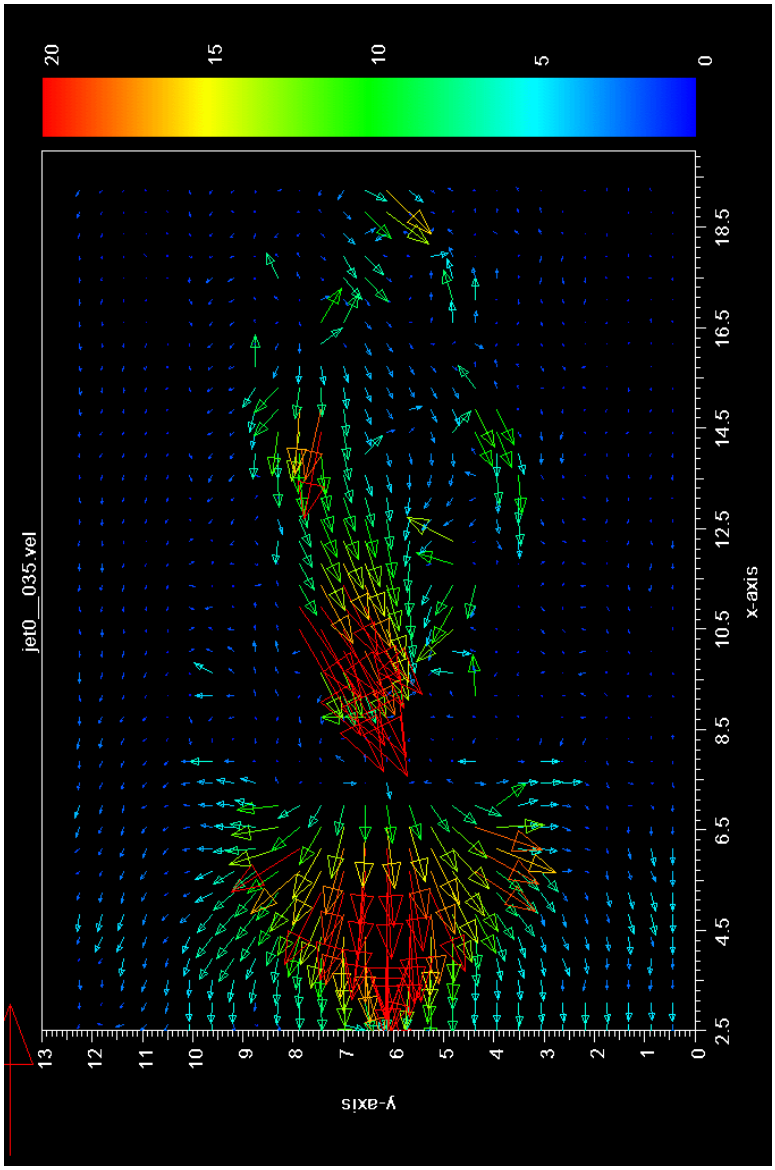

Figure A.18: Velocity comparison of DPIV frames 34 and 35.

Bibliography

[1] P. Krueger and A. Gharib, "Thrust augmentation and vortex ring evolution in a fully pulsed jet," *AIAA Journal*, vol. 43, no. 4, pp. 792–801, 2005.

[2] J. Anderson, K. Streitlien, D. Barrett, and M. Triantafyllou, "Oscillating foils of high propulsive efficiency," *Journal of Fluid Mechanics*, vol. 360, pp. 41–72, 1998.

[3] F. Hover, O. Haugsdal, and M. Triantafyllou, "Effect of angle of attack profiles in flapping foil propulsion," *Journal of Fluids and Structures*, vol. 19, no. 1, pp. 37–47, 2004.

[4] S. Licht, V. Polidoro, M. Flores, F. Hover, and M. Triantafyllou, "Docking for an autonomous ocean sampling network," *IEEE Journal of OCeanic Engineering*, vol. 26, no. 4, pp. 498–514, 2001.

[5] M. Triantafyllou and G. Triantafyllou, "An efficient swimming machine," *Scientific American*, vol. 272, no. 3, pp. 64–70, 1995.

[6] M. Triantafyllou, A. Techet, and F. Hover, "Review of experimental work in biomimetic foils," *IEEE Journal of Oceanic Engineering*, vol. 29, no. 3, pp. 585–594, 2004.

[7] S. Singh, A. Simha, and R. Mittal, "Biorobotic auv maneuvering by pectoral fins: Inverse control design based on cfd paramaterization," *IEEE Journal of OCeanic Engineering*, vol. 29, no. 3, pp. 777–785, 2004.

[8] D. Yoerger, J. Cooke, and J. Slotine, "The influence of thruster dynamics on underwater vehicle behavior and their incorporation into control system design," *IEEE Journal of Oceanic Engineering*, vol. 15, no. 3, pp. 167–178, 1980.

[9] A. Healey, S. Rock, S. Cody, D. Miles, and J. P. Brown, "Toward an improved understanding of thruster dynamics for underwater vehicles," *IEEE Journal of Oceanic Engineering*, vol. 20, no. 4, pp. 354–361, 1995.

[10] H. Wang, R. Marks, T. McLain, S. Fleischer, D. Miles, G. Sapilewski, and S. Rock, "Otter: A testbed submersible for robotics research," in *ANS 1995*, Monterey, CA, 1995.

[11] J. Kerwin, *MIT Lecture Notes: Hydrofoils and Propellers 13.014*, 2001.

[12] F. Lane, *Kingdon of the Octopus: The Life History of the Cephalopoda*. Sheridan House, 1960.

[13] S. Vogel, *Cats' Paws and Catapults: Mechanical Worlds of Nature and People*. W.W. Norton and Company, 1998.

[14] M. Denny, *Air and Water: The Biology and Physics of Life's Media*. Princeton University Press, 1993.

[15] J. Seikmann, "On a pulsating jet from the end of a tube, with applications to the propulsion of certain aquatic animals," *Journal of Fluid Mechanics*, vol. 15, pp. 399–418, 1963.

[16] E. Trueman, "Motor performance of some cephalopods," *Journal of Experimental Biology*, vol. 49, pp. 495–505, 1968.

[17] M. Nixon and J. Messenger, *The Biology of Cephalopods*. Academic Press, 1977.

[18] D. Weihs, "Periodic jet propulsion of aquatic creatures," *Fortschritte der Zoologie*, vol. 24, pp. 171–175, 1977.

[19] R. O'Dor and D. Webber, "The constraints on cephalopods: why squid aren't fish," *Canadian Journal of Zoology*, vol. 64, pp. 1591–1605, 1986.

[20] ——, "Invertebrate athletes: Trade-offs between transport efficiency and power density in cephalopod evolution," *Journal of Experimental Biology*, vol. 160, pp. 93–112, 1991.

[21] M. Clarke, "A review of the systematics and ecology of oceanic squids," *Advanced Marine Biology*, vol. 4, pp. 91–300, 1966.

[22] R. O'Dor and J. Hoar, "Does geometry limit squid growth?" *ICES Journal of Marine Science*, vol. 57, pp. 2–14, 2000.

[23] J. Dabiri, S. Colin, J. Costello, and M. Gharib, "Flow patterns generated by oblate medusan jellyfish: field measurements and laboratory analyses," *Journal of Experimental Biology*, vol. 208, no. 7, pp. 1257–1265, 2005.

[24] J. Dabiri and M. Gharib, "Starting flow through nozzles with temporally variable exit diameter," *Journal of Fluid Mechanics*, vol. 538, pp. 111–136, 2005.

[25] B. Smith and A. Glezer, "The formation and evolution of synthetic jets," *Physics of Fluids*, vol. 10, no. 9, pp. 2281–2297, 1998.

[26] A. Crook and N. Wood, "Measurements and visualizations of synthetic jets," *AIAA 39th Aerospace Sciences Meeting and Exhibit, AIAA Paper 2001-0145*, January 2001.

[27] M. Krieg, C. Coley, C. Hart, and K. Mohseni, "Synthetic jet thrust optimization for application in underwater vehicles," in *Proc. 14th International Symposium on Unmanned Untethered Submersible Technology*, Durham, NH, August 2005.

[28] M. Krieg, A. Pitty, M. Salehi, and K. Mohseni, "Optimal thrust characteristics of a synthetic jet actuator for application in low speed maneuvering of underwater vehicles," in *Proc. of 2005 IEEE/MTS OCEANS Conference*, Washington, D.C., September 2005.

[29] D. Rizzetta, M. Visbal, and M. Stanek, "Numerical investigation of synthetic-jet flowfields," *AIAA Journal*, vol. 37, no. 8, pp. 919–927, 1999.

[30] C. Lee and D. Goldstein, "Two-dimensional synthetic jet simulation," *AIAA Journal*, vol. 40, no. 3, pp. 510–516, 2002.

[31] S. Mallinson, C. Kwok, and J. Reizes, "Numerical simulation of micro-fabricated zero mass-flux actuators," *Sensors and Actuators*, vol. 105, pp. 229–236, 2003.

[32] K. Shariff and A. Leonard, "Vortex rings," *Annual Review of Fluid Mechanics*, vol. 24, pp. 235–279, 1992.

[33] T. Maxworthy, "Some experimental studies of vortex rings," *Journal of Fluid Mechanics*, vol. 80, pp. 465–495, 1977.

[34] N. Didden, "Formation of vortex rings- rolling-up and production of circulation," *Zeitschrift fur Angewandte Mathematik und Physik*, vol. 30, no. 1, 1979.

[35] M. Gharib, E. Rambod, and K. Shariff, "A universal time scale for vortex ring formation," *J. Fluid Mech.*, vol. 360, pp. 121–140, 1998.

[36] M. Shusser, M. Rosenfeld, and K. Mohseni, "On the effect of pipe boundary layer growth on the formation of a laminar vortex ring generated by a piston/cylinder arrangement," *Theoretical and Computational Fluid Dynamics*, vol. 15, pp. 306–316, 2002.

[37] J. Dabiri and M. Gharib, "A revised slug model boundary layer correction for starting jet vorticity flux," *Theoretical and Computational Fluid Dynamics*, vol. 17, pp. 293–295, 2004.

[38] P. Krueger, "An over-pressure correction to the slug model for vortex ring circulation," *Journal of Fluid Mechanics*, vol. 545, pp. 42–443, 2005.

[39] A. Glezer and M. Amitay, "Synthetic jets," *Annual Review of Fluid Mechanics*, vol. 34, pp. 503–529, 2002.

[40] M. Lighthill, "Acoustic streaming," *Journal of Sound Vibrations*, vol. 61, p. 391, 1978.

[41] A. Crook, A. Sadiri, and N. Wood, "The development and implementation of synthetic jets for the control of seperated flow," in *17th Applied Aerodynamics Conference*, Norfolk, VA, 1999.

[42] R. James, J. Jacobs, and A. Glezer, "A round turbulent jet produced by an oscillating diaphragm," *Physics of Fluids*, vol. 8, no. 9, pp. 2484–2495, 1996.

[43] B. Smith and A. Glezer, "Jet vectoring using synthetic jets," *J. Fluid Mech.*, vol. 458, pp. 1–34, 2002.

[44] S. Mallinson, G. Hong, and J. Reizes, "Some characteristics of synthetic jets," in *30th AIAA Fluid Dynamics Conference*, Norfolk, VA, 1999.

[45] S. Mallinson, J. Reizes, G. Hong, and H. Haga, "The operation and application of synthetic jet actuators," in *Fluids 2000*, Denver, CO, 2000.

[46] R. Rathnasingham and K. Breur, "Coupled fluid-structural characteristics of actuators for flow control," *AIAA Journal*, vol. 35, no. 5, pp. 832–837, 1997.

[47] K. Mohseni, R. Hongyu, and T. Colonius, "Numerical experiments on vortex ring formation," *Journal of Fluid Mechanics*, vol. 430, pp. 267–282, 2001.

[48] K. Mohseni, "Impulse extremization in synthetic jet actuators for underwater locomotion and manuevering," in *23rd International Conference on Offshore Mechanics and Arctic Engineering*, Vancouver, Canada, June 2004, also published

as a chapter in Advances in Engineering Mechanics, Reflections and Outlooks: In Honor of Theodore Y.-T. Wu, edited by A.T. Chwang, M.H. Teng and D.T. Valentine, World Scientific Pulishing Company, 2005.

[49] D. Coe, M. Allen, M. Trautman, and A. Glezer, "Micromachined jets for manipulation of macro jets," in *Solid-State Sensor and Actuator Wrokshop*, Hilton Head,S.C., 1994.

[50] M. Müller, L. Bernal, R. Moran, P. Washabaugh, B. Parviz, and K. Najafi, "Micromachined acoustic resonators for microjet propulsion," *Proceedings of the 38th Aerospace Sciences Meeting and Exhibit*, January 2000.

[51] M. Müller, L. Bernal, R. Moran, P. Washabaugh, B. Parviz, T.-K. Chou, C. Zhang, and K. Najafi, "Thrust performance of micromachined synthetic jets," *Proceedings of Fluids 2000*, June 2000.

[52] M. Amitay, D. Smith, V. Kibens, D. Parekh, and A. Glezer, "Aerodynamic flow control oven an unconventional airfoil using synthetic jet actuators," *AIAA Journal*, vol. 39, no. 3, pp. 361–370, 2001.

[53] R. Holman, Y. Utturkar, R. Mittal, B. Smith, and L. Cattafesta, "Formation criterion for synthetic jets," *AIAA Journal*, vol. 43, no. 10, 2005.

[54] F.-J. Chen, C. Yao, R. Bryant, and R. Fox, "Development of synthetic jet actuators for active flow control at nasa langley," AIAA Paper 2000-2405, 2000.

[55] B. Smith and A. Glezer, "Vectoring and small-scale motions effected in free shear flows using synthetic jet actuators," *AIAA Paper 97-0213*, 1997.

[56] K. Mohseni, "Zero-mass pulsatile jets for unmanned underwater vehicle maneuvering," in *AIAA 3rd Unmanned Unlimited Technical Conference, AIAA Paper 2004-6386*, Chicago, IL, September 2004.

[57] Q. Gallas, R. Holman, T. Nishada, B. Carroll, M. Sheplak, and L. Cattafesta, "Lumped element modeling of piezoelectric-driven synthetic jet actuators," *AIAA Journal*, vol. 41, no. 2, pp. 240–247, 2003.

[58] C. Rumsey, T. Gatski, W. S. III, V. Vatsa, and S. Viken, "Summary of the 2004 computational fluid dynamics validation workshop on synthetic jets," *AIAA Journal*, vol. 44, no. 2, pp. 194–207, 2006.

[59] H. Tang and S. Zhong, "Incompressible flow model of synthetic jet actuators," *AIAA Journal*, vol. 44, no. 4, pp. 487–497, 2001.

[60] A. Polsenberg-Thomas, Michele, M. Grazier-G'Sell, K. Fisher, and J. Burdick, "Synthetic jet propulsion for small underwater vehicles," in *Proc. IEEE Int. Conf. on Robotics and Automation*, Barcelona, Spain, April 2005.

[61] A. Polsenberg-Thomas, J. Burdick, and K. Mohseni, "An experimental study of voice-coil driven synthetic jet propulsion for underwater vehicles," in *Proc. OCEANS Conference*, Washington D.C., September 2005.

[62] A. Polsenberg-Thomas, J. Dabiri, K. Mohseni, and J. Burdick, "An experimental study of voice-coil driven synthetic jet propulsors for underwater vehicles," in *Proc. 14th International Symposium on Unmanned Untethered Submersible Technology*, Durham, NH, August 2005.

[63] H. Kim, A. Jauregui, C. Morrison, K. Najafi, L. Bernal, and P. Washabaugh, "Power electrostatic helmholtz-resonance generator for propulsion and cooling," in *Proc. 12th Solid-State Sensor, Actuator, and Microsystems Workshop*, Hilton Head Island, SC, June 2006.

[64] D. Weems, *Designing, Building, and Testing Your Own Speaker System.* McGraw Hill, 1997.

[65] W. Reynolds, D. Parekh, P. Juvet, and M. Lee, "Bifurcating and blooming jets," *Annual Review of Fluid Mechnics*, vol. 35, pp. 295–315, 2003.

[66] L. Kral, J. Donovan, A. Cain, and A. Cary, "Numerical simulation of synthetic jet actuators," in *AIAA Paper 97-1824*, 1997.

[67] C. Willert and M. Gharib, "Digital particle image velocimetry," *Experiments in Fluids*, vol. 10, pp. 181–193, 1991.

[68] A. Smits, *A Physical Introduction to Fluid Mechanics.* John Wiley and Sons, Inc., 2000.

[69] P. Krueger, "The significance of vortex ring formation and nozzle exit overpressure to pulsatile jet propulsion," Ph.D. dissertation, California Institute of Technology, May 2001.

[70] K. Mohseni and M. Gharib, "A model for universal time scale of vortex ring formation," *Physics of Fluids*, vol. 10, no. 10, pp. 2436–2438, 1998.

[71] G. Matsumoto and W. Hamner, "Modes of water manipulation by the lobate ctenophore *Leucothea* sp." *Marine Biology*, vol. 97, pp. 551–558, 1988.

[72] S. Mallinson and J. Reizes, "Numerical simulation of membrane forcing effects on synthetic jet actuators," in *14th Australasian Fluid Mechanics Conference*, Adelaide, Australia, 2001.

[73] R. Sabersky, A. Acosta, E. Hauptmann, and E. Gates, *Fluid Flow: A First Course in Fluid Mechanics, Fourth Edition.* Prentice Hall, 1999.

[74] R. Granger, *Fluid Mechanics.* Dover Books, 1995.

[75] M. Ablowitz and A. Fokas, *Complex Variables: Introduction and Applications.* Cambridge University Press, 1997.

[76] J. Brown and R. Churchill, *Complex Variables and Applications.* McGraw Hill, 1996.

[77] W. Price, "A controlled random search procedure for global optimization," *The Computer Journal*, vol. 20, no. 4, 1976.

[78] M. Milano, J. Schmidhuber, and P. Koumoutsakos, "Self-organizing nets for optimization," *IEEE. Trans. On Neural Networks*, vol. 15, no. 3, 2004.

[79] J. Newman, *Marine Hydrodynamics*. MIT Press, 1999.